MOLECULAR STRUCTURE AND BONDING AT NANOEMULSION SURFACES

by

ANDREW P. CARPENTER

A DISSERTATION

Presented to the Department of Chemistry and Biochemistry
and the Graduate School of the University of Oregon
in partial fulfillment of the requirements
for the degree of
Doctor of Philosophy

June 2020

DISSERTATION APPROVAL PAGE

Student: Andrew P. Carpenter

Title: Molecular Structure and Bonding at Nanoemulsion Surfaces

This dissertation has been accepted and approved in partial fulfillment of the requirements for the Doctor of Philosophy degree in the Department of Chemistry and Biochemistry by:

Dr. Jeffrey Cina	Chairperson
Dr. Geraldine Richmond	Advisor
Dr. Jim Prell	Core Member
Dr. Eric Corwin	Institutional Representative

and

Kate Mondloch	Interim Vice Provost and Dean of the Graduate School

Original approval signatures are on file with the University of Oregon Graduate School.

Degree awarded June 2020

DISSERTATION ABSTRACT

Andrew P. Carpenter

Doctor of Philosophy

Department of Chemistry and Biochemistry

June 2020

Title: Molecular Structure and Bonding at Nanoemulsion Surfaces

The formation of nanoemulsions, nanosized oil droplets in water, has provided scientists with unique hydrophobic chemical environments capable of being leveraged for a diverse set of applications ranging from the petroleum to pharmaceutical industries. In order to stabilize nanoemulsions, the droplet surface must be stabilized. While empirical rules have been established for the kinds of chemicals able to be used for nanoemulsion stabilization, there is a lack of knowledge of the molecular details of the interface that contribute to droplet stability. This lack of knowledge is no more present than in the study of bare nanoemulsions, absent emulsifiers, where a significant negative charge of unknown origin accumulates at the droplet surface and provides the necessary stabilizing electrostatic force.

The studies detailed in this dissertation take advantage of vibrational sum-frequency scattering spectroscopy (VSFSS) to study the surfaces of nanoemulsion droplets and build up a molecularly specific picture of the droplet interface. Beginning with the creation of bare low charge nanoemulsions, an explanation for the accumulation of negative charge at bare nanoemulsion surfaces is developed that can be generalized to the charge accumulation observed at nearly all aqueous-hydrophobic surfaces. Further studies of bare nanoemulsion surfaces focus on the structure and bonding of the aqueous

and hydrophobic phases, with the first direct measurements of interfacial water at the bare nanoemulsion surface being reported. These measurements have found that the chemical bonding interactions between oil and water molecules at the nanoemulsion surface is different from that of the extended planar oil-water interface. It is also found that all surfactants studied induce a structural reorganization of interfacial oil molecules.

Other studies, reported here, focus on the assembly of surfactants to nano- oil and water droplet surfaces. Surfactant alkyl chains assemble in a similar manner at the bare oil and water droplet surfaces, but in a different manner compared to the planar oil-water interface. However, despite differences in the alkyl chain assembly, further work investigating headgroup solvation and charge screening phenomena finds that these phenomena occur in similar fashions at the curved and planar oil-water interfaces.

This work contains published and unpublished co-authored material.

CURRICULUM VITAE

NAME OF AUTHOR: Andrew P. Carpenter

GRADUATE AND UNDERGRADUATE SCHOOLS ATTENDED:

University of Oregon, Eugene, OR
Linfield College, McMinnville, OR

DEGREES AWARDED:

Doctor of Philosophy, Chemistry, 2020, University of Oregon
Masters of Science, Chemistry, 2016, University of Oregon
Bachelor of Arts, Chemistry, 2012, Linfield College
Bachelor of Arts, Mathematics, 2012, Linfield College

AREAS OF SPECIAL INTEREST:

Nonlinear Spectroscopy
Second Order, Vibrational
Interfacial Chemistry

PROFESSIONAL EXPERIENCE:

Graduate Research Assistant in the Richmond Laboratory, Department of Chemistry and Biochemistry, University of Oregon, Eugene (2013-Present)

Graduate Teaching Assistant, Department of Chemistry and Biochemistry, University of Oregon, Eugene (2013-2015, 2017-2019)
Physical Chemistry Laboratory, Presidential Undergraduate Research Scholarship (PURS) Program

Teaching Assistant, Department of Chemistry, Linfield College, McMinnville (2009-2012)
General Chemistry Lab, Organic Chemistry Lab, Department Tutor

GRANTS, AWARDS, AND HONORS:

CAS Dissertation Research Fellowship, University of Oregon, 2019-2020

Graduate Teaching Award, Chemistry, University of Oregon, 2015

PUBLICATIONS:

Carpenter, Andrew P.; Foster, Marc J.; Richmond, Geraldine L. "Effects of Charge Screening on Surfactant Adsorption to the Nanoemulsion and Planar Oil-Water Interfaces." (In Preparation)

Tran, Emma; Carpenter, Andrew P.; Richmond, Geraldine L. "Interfacial Molecular Characterization of pH-tunable Polyethylenimine at the Nanoemulsion Droplet Surface." *Langmuir*, (submitted).

Carpenter, Andrew P.; Altman, Rebecca M.; Tran, Emma; Richmond, Geraldine L. "How Low Can You Go? Molecular Details of Low Charge Nanoemulsion Surfaces." *The Journal of Physical Chemistry B,* 124, 20, 4234-4245.

Carpenter, Andrew P.; Tran, Emma; Altman, Rebecca M.; Richmond, Geraldine L. "Formation and Surface-Stabilizing Contributions to Bare Nanoemulsions Created with Negligible Surface Charge." *Proceedings of the National Academy of Sciences*, 116(19), 2019, 9214-9219.

Hensel, Jennifer K.; Carpenter, Andrew P.; Ciszewski, Regina K.; Kittredge, Clive T.; Schabes, Brandon K.; Moore, Fred G.; Richmond, Geraldine L. "Molecular Characterization of Water and Surfactant AOT at Nanoemulsion Surfaces." *Proceedings of the National Academy of Sciences*, 114(51), 2017, 13351-13356.

Robertson, Ellen J.; Carpenter, Andrew P.; Olson, Courtney M; Ciszewski, Regina K.; Richmond, Geraldine L. "Metal Ion Induced Adsorption and Ordering of Charged Macromolecules at the Aqueous/Hydrophobic Liquid Interface." *The Journal of Physical Chemistry C,* 118(28), 2014, 15260-15273.

ACKNOWLEDGMENTS

This dissertation would not exist without a rather large village of people who have supported me, cared for me, challenged me, enjoyed life with me, and encouraged me over the last seven years. I feel particularly indebted to my village.

First, I would like to convey my gratitude to Prof. Geraldine (Geri) Richmond. When I first met Geri during my visitation weekend in the winter of 2013, I got the impression of a scientist who was able to see the world outside the walls of her laboratory and cared for others. I was not wrong. Geri, the rigor and expectations you have had for me has been graciously paired with encouragement and votes of confidence when experiments weren't going smoothly and I felt lost in the basement. Thank you for everything you've done for me these past seven years.

To my family, Bruce, Beth, and Michael, I don't even know where to begin. Thank you doesn't even come close to being a starting point for expressing the gratitude I have for you three. The support I've received from my parents in my pursuit of an education has been limitless. The phone calls with mom while walking to and from the lab in the dark and the bottomless pit of wisdom my dad seems to possess, have been foundational. To Michael, the last two years of my PhD have been so much better because you've been in town. To all of three of you, I love you.

To all the past and present Richmond Lab members, thank you for making this pursuit of a PhD such a wild and wonderful ride. Ellen thanks for getting me started in the lab. Jenny, everything I know and have been able to do started with your mentorship, teaching, and instruction. To Laura, Jet, Nick, Sumi, thanks for making the early years great. Brandon, I have deeply appreciated the many years of sharing an office with you.

Thanks for all the advice and insight you've shared about research and life in general. Bri, thanks for taking the plunge into research in the Richmond lab with me. Rebecca, thanks for guaranteeing I wouldn't be the last Richmond lab graduate student, and for vastly more than that. To Konnor, Evan, Marc, and Emma, good luck. I'm excited to see what you all accomplish!

To Larry Scatena and Fred Moore, thank you for your continual support and advice throughout the years. It is greatly appreciated. To Liz Atkinson, Brian Gilbert, and Stephen Bricher, thank you all for inspiring me at Linfield.

I also want to also express gratitude to Prof. Sylvie Roke. Thank you for providing me the opportunity to learn more about the wonderful scattering spectroscopy you have pioneered and continue to develop. The impact of sum-frequency scattering spectroscopy on the field of surface science is incredibly profound.

To all my friends, thank you for everything. I almost hesitate to list names for fear of missing someone. To Zach, Kyle, Josh, Ben, Evan, Kirk, Jayme, Janelle, Claire, Beth, CJ, Cody, Sam, Andrew and Taylor Troxell, Logan and Charlotte Rau, Robin, Ali, Joey, Luke, Dan R, Wes, JJ, Kelsey, Emilie, Megan, Dean, Eric, Dan Q, Mark, Jefe, Jake, Curtis, Emmett, Kimber, Teagan, Logan, Sam, Miles and Tyler; I'm lucky to have made lifelong friends as good as you all. To anyone I missed and shouldn't have, I'm sorry. I've been truly blessed by so many great people over the years.

Finally, my faith has always been paramount to who I am. I am very blessed by God for everyone listed above, the community of faith I've had, and the church home I found at UFC. To everyone at UFC, thank you for everything.

This research was funded by the Department of Energy.

For Bruce, Beth, and Michael.

TABLE OF CONTENTS

Chapter Page

Chapter Page

LIST OF FIGURES

Figure Page

LIST OF TABLES

Table Page

CHAPTER I

INTRODUCTION

Emulsions are colloidal systems consisting of two immiscible liquid phases, where the phase possessing the lower volume fraction is dispersed as droplets within the higher volume fraction phase. These liquids are known as the dispersed and continuous phases, respectively. Significant attention is given to droplet stability of the dispersed phase as the stability of emulsion droplets is intimately tied to application. For example, within food science products require stable emulsion droplets so that products' shelf lives are desirable for consumers. Yet, in other applications, such as wastewater treatment or the processing of crude oil, the desired separation of hydrophilic and hydrophobic phases require the destabilization of emulsion droplets. Increasing attention is being given to emulsion systems where the droplet diameter is somewhere between 10's to 100's of nanometers, taxonomically known as nanoemulsions. These nano-sized emulsion systems are finding application in many industries; including cosmetics,[1-3] drug delivery purposes,[4-10] oil recovery,[11-14], food science,[15-18] and as nanoreactors for material synthesis.[19-20] Key to further application development of these nano-sized dispersions is a fundamental understanding of the molecular origins of nanoemulsion stability and the chemical environment present at their surfaces.

Nanoemulsions differ from their larger and smaller analogues, miniemulsions and microemulsions/micelles, respectively, in that nanoemulsions are kinetically stable structures, whereas the other droplets are thermodynamically stable.[17, 21] Formation of nanoemulsions requires an input of energy to break up the dispersed phase and mix it into

the continuous phase.[17, 21] This can be accomplished through both low and high energy mixing procedures such as the emulsion inversion point or phase inversion temperature methods and ultrasonication, respectively.[18, 21-22] After nanoemulsion formation the continuous and dispersed phases will quickly phase separate unless the droplet surface can be stabilized. Once the surface has been stabilized nanoemulsion droplets are remarkably robust and capable of maintaining a relatively constant droplet size in the midst of changes to solution pH or salinity, dilution, temperature, and other solution conditions.[21, 23-28] This robust kinetic stability, in addition to tunable rheological properties, small size, and low polydispersity, are what have accelerated nanoemulsion application across seemingly disparate industries.[1, 21, 29-32]

Since the origin of nanoemulsion stability comes from the stabilization of the droplet surface, understanding the chemical environment at the droplet surface becomes of utmost importance. During nanoemulsion formation the free energy of the chemical system is increased due to the rise in surface area.[17, 33] To compensate for the increased surface area necessitates a lowering of interfacial tension at the droplet surface.[17, 33] Most often, this is accomplished through the addition of surface-active chemicals, which adsorb to the droplet surface and reduce the interfacial tension. Nanoemulsions have been stabilized by simple surfactants,[34-37] ionic and non-ionic polymers,[8, 38] and more complex chemical mixtures.[8, 13-14, 39-40] In addition to lowering the interfacial tension, emulsifiers introduce additional electrostatic or steric stabilizing forces that work to prevent droplet coalescence.[41] This is illustrated in Figure 1.1. Curiously, though, there are reports of stable bare nanoemulsions, absent emulsifiers, that are stabilized by a negative charge accumulation at the droplet surface.[42-43] A consistent and broadly

accepted explanation for the remarkable stability of bare nanoemulsions has yet to be found and is still under debate. Underlying this debate is the lack of molecularly specific information of the chemical composition, molecular structure, and intermolecular bonding environment present at the droplet surface.

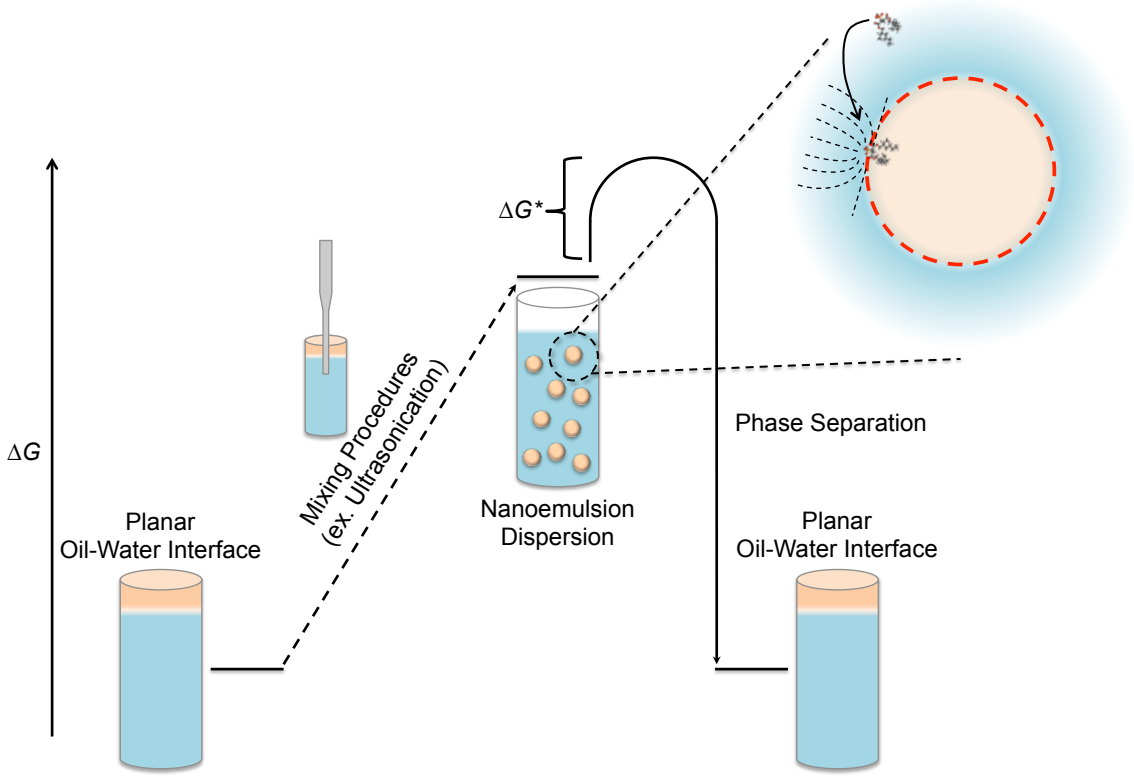

Figure 1.1. Illustration of the thermodynamics of nanoemulsion formation and stability. A generic mixing procedure provides sufficient energy to disperse the oil into the water, where emulsifiers can adsorb to the surface and provide the relevant forces to establish an energetic barrier, delaying phase separation.

Understanding the molecular level details that contribute to nanoemulsion formation and stability is necessary for a coherent explanation of bare nanoemulsion stability, as well as a continued development towards application. Until recently, molecular level details of the nanoemulsion interface have primarily been inferred from

non-chemically specific measurements such as planar surface tension measurements,[33, 44] neutron and x-ray reflectivity/scattering,[12, 45-46] electrophoretic mobility measurements,[47-48] and by monitoring droplet size as a function of time.[17, 21, 49] These "macroscopic" techniques can, respectively, provide a baseline understanding of the surface activity of emulsifiers, the thickness of interfacial layers around the nanoemulsion droplet, a quantification of the droplet surface charge, and a metric to judge the efficacy of certain emulsifiers to stabilize the droplet structure. Mainstream vibrational spectroscopic techniques, such as infrared or Raman spectroscopies, possess a chemical selectivity that would be desirable for the study of nanoemulsion interfaces. Unfortunately, the way they have successfully been leveraged to elucidate molecularly specific features of micelles[50-55] lacks the interfacial specificity to selectively probe the larger nanoemulsion droplet surface.

Vibrational sum-frequency spectroscopy (VSFS) has been the technique of choice to study the molecular details of planar aqueous-hydrophobic interfaces. VSFS provides a means of studying the composition, chemical bonding environment, and structural organization of th interfacial region by measuring the vibrational spectrum of aqueous-hydrophobic interfaces.[56-60] This technique has been successfully applied in the study of air-water,[61-63] solid-water,[64] and oil-water interfaces.[65-67] Yet, due to the different mechanisms in which a planar interface and nanoemulsion droplet surface are formed,[17] it is not clear that the information gained from VSFS experiments at a planar interface is directly transferrable to the droplet surface. Vibrational sum-frequency *scattering* spectroscopy (VSFSS), originally pioneered and developed by Roke et. al.,[68-69] is an extension of the original VSFS technique that can circumvent this issue. VSFSS

measures the vibrational spectrum of particle surfaces where the average particle diameter is on the order of 100's of nanometers to microns.[70] The sum-frequency response generated at the nanoparticle surface in a VSFSS experiment has been shown to contain all the same information that is obtained in the reflection geometry VSFS experiments on planar surfaces. The advent of VSFSS has already proven to be revolutionary in the study of nanoemulsion surfaces by way of providing a means of interrogating the nanodroplet surface with a chemical specificity. The first nanoemulsion studies utilizing VSFSS have provided information on the interfacial structure of surfactants,[35, 71-72] the organization of hydrophobic phase of highly charged bare nanoemulsions,[73-74] water structure and bonding at nanodroplet surfaces,[73-75] and ion interactions at emulsion surfaces.[72, 76-77]

This dissertation is a compilation of studies that seek to provide a molecular description of the chemical structure and bonding environment at both bare and surfactant coated nanoemulsions surfaces. The theory of sum-frequency generation from nanoparticle and planar interfaces is presented in Chapter II, followed by a description of the experimental apparatuses used to conduct this research in Chapter III. Detailed in Chapter IV is the creation of bare low charge nanoemulsions (LCNE), which are contrasted against the backdrop of previously reported bare nanoemulsions possessing large negative zeta potentials. Using VSFSS to study the bare LCNE surface, conclusions are drawn about the origins of the observed negative charge accumulation at bare aqueous-hydrophobic interfaces. The first direct measurements of an unbound water oscillator are made at the LCNE droplet surface, by which it is concluded the water-oil bonding interactions are stronger at the bare nanoemulsion surface relative to the planar

oil-water interface. LCNE samples are also used to understand how the adsorption of simple surfactants perturb the structure of interfacial water and oil molecules. These bare nanoemulsion studies are followed in Chapter V by investigations into the molecular structure and solvation environment of surfactant adsorbed to both the nano- oil and water droplet surfaces. This structural arrangement and solvation environment is compared to surfactant assembly at a similar planar oil-water interface. Chapter VI reports on studies into the role electrostatic interactions between ionic surfactants have on surface adsorption at planar and droplet surfaces. Finally, in Chapter VII the work that has been discussed in this dissertation is summarized, followed by some additional demonstrations of VSFSS towards the study of other chemical systems along with a brief perspective on where second-order nonlinear scattering spectroscopies can be developed further. This final discussion serves as an outlook on the potential of VSFSS to provide important molecular scale information of other nano-sized particle interfaces.

The work reported within this dissertation has been aided by the work of several co-authors. Relevant contributions are recognized at the beginning of each chapter.

CHAPTER II

SUM-FREQUENCY GENERATION FROM PARTICLE AND PLANAR INTERFACES

Vibrational sum-frequency generation has become a powerful tool in the study of the molecular details of interfacial phenomena, particularly at aqueous-hydrophobic interfaces, because this technique measures the vibrational spectrum of molecules within the thin interfacial region between two phases. This chapter provides a brief theoretical background for vibrational sum-frequency generation at both the planar and nanoemulsion oil-water interfaces. Starting with a general overview of light-matter interactions, second-order nonlinear spectroscopies are then discussed in the context of vibrational sum-frequency spectroscopy of the planar oil-water interface. After the theory has been discussed for reflection geometry second-order nonlinear spectroscopies, the theoretical framework developed by Roke and co-workers is followed to show how a series of transformations between coordinate reference frames connect the macroscopic beam polarizations to the molecular information at a nanoemulsion surface. These transformations are then used to derive the specific contributions to the sum-frequency electric fields for the SSP and PPP beam polarization combinations for spherical nanoemulsions. Through these transformations across reference frames, the ability to obtain molecular information from nanoemulsion droplet surfaces is demonstrated. Additional resources are cited throughout, with an in depth background on vibrational and nonlinear spectroscopies able to be found in several texts.[78-81]

Nonlinear Effects in Light-Matter Interactions

Utilizing the interactions of light with matter has given scientists a tool to probe, dissect, and build up a description of the molecular scale. Given an electric field, $\boldsymbol{E}$, propagating through a material, a force is exerted upon the valence electrons of the molecules that make up the material. For low intensity light the force imparted on the material will be small and the light-matter interaction can be described as an oscillating dipole (equation 2.1).

$$\boldsymbol{\mu} = \mu_o + \alpha \boldsymbol{E} \tag{2.1}$$

For molecules within the irradiated material, their dipole ($\boldsymbol{\mu}$) is a function of the permanent molecular dipole (μ_o) and the polarizability (α), which interacts with the light's electric field. Summing over all the molecular dipoles in a material provides the material's macroscopic induced polarization ($\boldsymbol{P}$), the induced dipole per unit volume. Under low intensity light, the total induced polarization can be simplified to only the first order polarization while ignoring the macroscopic average of the permanent molecular dipole, since the majority of bulk materials lack a permanent dipole in the absence of a static external electric field. Thus, the induced polarization is written as:

$$\boldsymbol{P}^{(1)} = \varepsilon_o \boldsymbol{\chi}^{(1)} \boldsymbol{E} \tag{2.2}$$

Within equation 2.2, ε_o is the permittivity of a vacuum and $\boldsymbol{\chi}^{(1)}$ is a material's first order susceptibility, representing the average molecular polarizability within the material. $\boldsymbol{P}^{(1)}$

describes solely the material's linear response. However, as the electric field strength of the incident light increases, nonlinear effects need to be taken into account.

As laser technology has advanced, in particular with ability to generate ultrafast pulses of light, it is now commonplace to be able to produce pulses of light with high intensity electric fields. As the electric field strength increases, higher-order, nonlinear, effects within a material can be probed. These nonlinear interactions are broadly described in equation 2.3 as a power series expansion of the induced polarization.

$$\boldsymbol{P} = \left(\boldsymbol{P}^{(1)} + \boldsymbol{P}^{(2)} + \boldsymbol{P}^{(3)} + \cdots + \boldsymbol{P}^{(n)}\right) \tag{2.3}$$

Here, $\boldsymbol{P}^{(n)}$ is a representation of the nth order induced polarization, with the sum of the polarizations contributing to the total induced polarization. Rewriting equation 2.3 to describe the relationship between the induced polarization and incident electric fields results in equation 2.4.

$$P_i = \varepsilon_o\left(\chi_{ij}^{(1)}E_j + \chi_{ijk}^{(2)}E_jE_k + \chi_{ijk}^{(3)}E_jE_kE_l + \cdots\right) \tag{2.4}$$

Similar to the first-order material response described above, $\boldsymbol{\chi}^{(n)}$ is material's nth-order susceptibility. Since second-order spectroscopies are the primary spectroscopic techniques used in this dissertation, focus will be given to the second-order term.

Second-Order Spectroscopies of Liquid Interfaces

Sum-frequency and second harmonic generation are the most widely used second-order processes in the study of liquid-liquid interfaces. Within this dissertation, vibrational sum-frequency spectroscopy is used. For sum-frequency generation, the second order polarization can be written as:

$$P_i^{(2)}(\omega_0) = \chi_{ijk}^{(2)} E_j(\omega_1) E_k(\omega_2) \tag{2.5}$$

Here, the induced second-order polarization ($P_i^{(2)}$) will be dependent upon the second-order susceptibility ($\chi_{ijk}^{(2)}$), a third-rank tensor, which describes the average material response to the external electric fields E_j and E_k oscillating at frequencies of ω_1 and ω_2. For sum-frequency generation, the induced second-order polarization will oscillate at the sum of the incident frequencies ($\omega_0 = \omega_1 + \omega_2$). Other terms exist for additional second-order nonlinear processes, such as difference-frequency generation,[59] but are neglected here to focus on sum-frequency generation.

Under the electric dipole approximation, $\chi_{ijk}^{(2)}$ will only be non-zero at the interface for liquid systems, giving rise to sum-frequency generation's surface selectivity. The liquid bulk can be considered a centrosymmetric environment, and as $\chi_{ijk}^{(2)}$ is a third-rank tensor with 27 elements, the only value those elements can have underneath the inversion symmetry operator is zero.

$$\chi_{ijk}^{(2)} = \chi_{-i-j-k}^{(2)} = -\chi_{ijk}^{(2)} = 0 \tag{2.6}$$

At the interface, however, the inversion symmetry is broken and $\chi^{(2)}_{ijk}$ can now possess non-zero values. Liquid surfaces are anisotropic within the plane of the interface and can be assigned $C_{\infty v}$ symmetry. Under the constraints of this symmetry group the majority of tensor elements within $\boldsymbol{\chi}^{(2)}$ will reduce to zero, except for 7 non-zero elements. Of those 7 non-zero elements, only 4 are unique due to the degeneracy of the axes that define the plane of the interface. Table 2.1 provides a table of these non-zero $\boldsymbol{\chi}^{(2)}$ elements and the beam polarization combinations used to probe them within common reflection geometry sum-frequency spectroscopy experiments. These relationships between polarization combination and $\boldsymbol{\chi}^{(2)}$ elements have been well established.[59]

Beam polarizations are denoted S and P in relationship to the plane of incidence (S – perpendicular and P – parallel). These polarizations belong to the coordinate system associated with $\chi^{(2)}_{ijk}$, which is that of the interfacial frame of reference (illustrated in Figure 2.1) with the z-axis aligned perpendicular to the interfacial plane. Polarization combinations are always reported in the order of descending photon energy; sum-frequency, visible, infrared. This connection between beam polarization and the nanoemulsion droplet surface will be discussed in short order.

Table 2.1 Beam polarization combinations used in reflection geometry sum-frequency spectroscopy and the $\boldsymbol{\chi^{(2)}_{ijk}}$ elements they probe under $\boldsymbol{C_{\infty v}}$ symmetry.

Beam Polarizations (SF, visible, IR)	**Non-Zero $\boldsymbol{\chi^{(2)}_{ijk}}$**
SSP	$\chi^{(2)}_{xxz}$
SPS	$\chi^{(2)}_{xzx}$
PSS	$\chi^{(2)}_{zxx}$
PPP	$\chi^{(2)}_{zzz}, \chi^{(2)}_{yyz}, \chi^{(2)}_{yzy}, \chi^{(2)}_{zyy}$

Vibrational Sum-Frequency Spectroscopy of the Planar Oil-Water Interface

Reflection geometry vibrational sum-frequency spectroscopy (VSFS) of planar oil-water interfaces uses a fixed frequency visible beam that is coherently overlapped with an infrared beam. Figure 2.1 illustrates the excitation process leading to sum-frequency generation and the experimental reflection geometry of common VSFS experiments. In VSFS experiments the visible beam is chosen to have a narrow bandwidth in the frequency domain and to be non-resonant with any electronic states. Meanwhile, the infrared beam is frequency tuned across a spectral region and can either be a broad or narrow frequency bandwidth. When the infrared beam frequency overlaps with the frequency of a vibrational mode there will be a resonant enhancement of the sum-frequency response at the interface provided the vibrational mode is both infrared and Raman active.

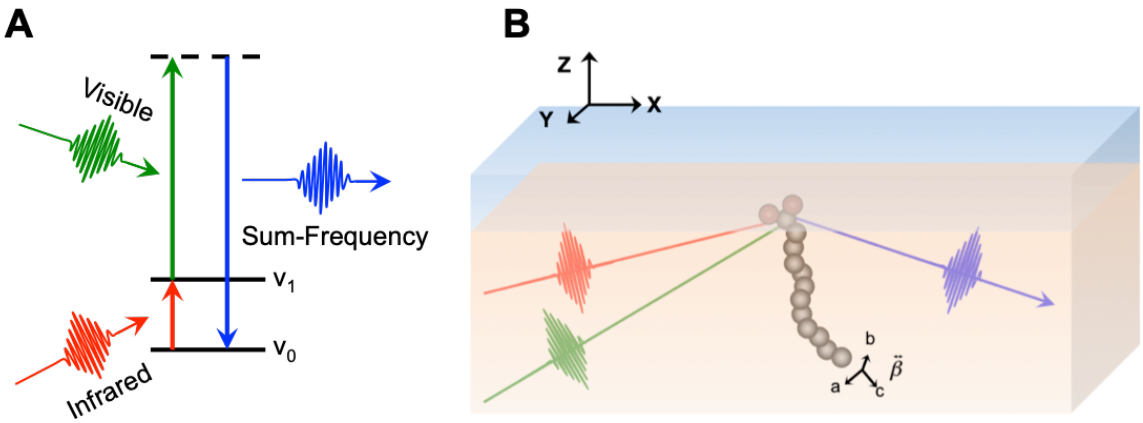

Figure 2.2. Illustration of (A) the excitation process leading to sum-frequency generation and (B) the experimental geometry of reflection VSFS experiments used to study the planar oil-water interface.

The detected sum-frequency signal (I_{SF}) will be proportional to the square of the effective second-order susceptibility and the intensities of the visible (I_{Vis}) and infrared (I_{IR}) lasers beams.

$$I_{SF} = \left|\chi_{Eff}^{(2)}\right|^2 I_{Vis} I_{IR} \tag{2.7}$$

The effective second-order susceptibility is related to the true second-order susceptibility through Fresnel coefficients that describe the reflection and transmission of the incident visible and infrared electric fields at the liquid-liquid interface.[59]

For vibrational sum-frequency, where the visible beam is non-resonant with any electronic states, the second-order susceptibility contains both vibrationally resonant contributions and a non-resonant contribution to the spectral line shapes. To account for the contributions from all resonant modes, the full second-order susceptibility is written as a sum of n vibrationally resonant modes and a non-resonant contribution (equation 2.8).

$$\chi^{(2)} = \chi_{NR}^{(2)} + \sum_{n} \chi_{R,n}^{(2)} \tag{2.8}$$

Non-resonant contributions ($\chi_{NR}^{(2)}$) have been shown to be largely invariant to incident frequencies.[82-83] Resonant contributions ($\chi_{R}^{(2)}$) to the second-order susceptibility, on the other hand, are dependent upon both the number (N) of oscillators and average molecular hyperpolarizability ($\beta^{(2)}$). The coordinate transform (T) connects the coordinate system of molecular vibrational motion to the laboratory frame coordinate system through a

series of Euler rotations. The average over all molecular orientations ultimately connects the molecular hyperpolarizability to the interfacial susceptibility.

$$\chi_{ijk}^{(2)} = N\langle T_{ia}T_{jb}T_{kc}\rangle\beta_{abc}^{(2)} \tag{2.9}$$

At the molecular level, the hyperpolarizability is expressed as the product of the infrared transition moment (A_c) and the Raman transition probability (M_{ab}) with a center frequency ω and natural linewidth (Γ).

$$\beta_{abc}^{(2)} = \frac{A_c M_{ab}}{\omega - \omega_{IR} - i\Gamma} \tag{2.10}$$

From the appearance of A_c and M_{ab} in equation 2.10 it is evident that a vibrational mode must be both infrared and Raman active for it to be sum-frequency active. Additionally, equation 2.10 illustrates how there is an enhancement of the sum-frequency generation when the infrared laser frequency (ω_{IR}) is resonant with the energy of a vibrational transition.

The origins of sum-frequency generation at extended planar liquid-liquid interfaces should be clear by now. Molecular level vibrational information ($\boldsymbol{\beta}^{(2)}$) is related to the interfacial susceptibility ($\boldsymbol{\chi}^{(2)}$) laboratory frame through a coordinate transform (T), averaged over all molecules. The polarizations of the incoming and outgoing laser beams, propagating through the plane of incidence, are referenced to the coordinate system of the interfacial plane. The polarization combinations of the sum-frequency, visible, and infrared beams, then, are capable of probing the vibrational modes with dipole components oriented perpendicular to the interface (SSP), parallel to the

interface (SPS, PSS), and a combination of dipole moments oriented in both directions (PPP).

Given that sum-frequency generation at the planar interface requires a non-isotropic chemical environment, how can someone measure the sum-frequency response from the surface of an isotropic particle such as a spherical nanoemulsion?

Vibrational Sum-Frequency Scattering of Nanoemulsion Surfaces

In the previous section it was discussed how sum-frequency generation is interfacially selective, with bulk signal averaging to zero for detection in the far field. While nanoemulsions are spherical, centrosymmetry is broken at the nanoemulsion interface and, therefore, a second-order polarization can be generated. Sum-frequency generation at different points of the nanoemulsion droplet surface don't completely deconstructively interfere in the farfield, resulting in an incomplete phase matching that allows sum-frequency photons to be detected by a detector in the farfield placed at some optimal angle. First experimentally reported by Roke et al.,[68] the theory was initially developed by Roke and was later expanded in collaboration with de Beer.[69-70, 84-88] This section follows the work by Roke and de Beer in their development of the transformations that connect the various reference frames involved in sum-frequency scattering spectroscopy. It then follows the use of those transformations to show which molecular hyperpolarizabilities elements contribute to sum-frequency signal detected in the SSP and PPP polarization combinations.

We start by considering the sum-frequency electric field (E_0) that is generated by the second-order polarization built up on the nanoemulsion interface (equation 2.11).

$$E_0(\omega) \propto \frac{k_0^2}{r_0} \mathbf{\Gamma}^{(2)}(\theta, R, \omega) E_{IR} E_{vis} \tag{2.11}$$

Measured at a distance r_0 from the nanoemulsion, the scattered sum-frequency electric field is proportional to the incident infrared and visible electric fields and the particle susceptibility ($\mathbf{\Gamma}^{(2)}$). The particle susceptibility is often referred to within literature as the effective susceptibility. However, the nomenclature of particle susceptibility is used here in order to avoid confusion with the reference to an effective susceptibility in equation 2.7. The particle susceptibility incorporates the geometric considerations necessary to understand and model sum-frequency from the particle surface. Similar to the transformation that connected the microscopic and surface reference frames with planar sum-frequency spectroscopy, the particle susceptibility possesses a series of coordinate transformations that connect the molecular level information at the particle surface ($\beta^{(2)}$) to the macroscopic laboratory frame in which the beam polarizations are defined. The reference frames involved in sum-frequency scattering are illustrated in Figure 2.2.

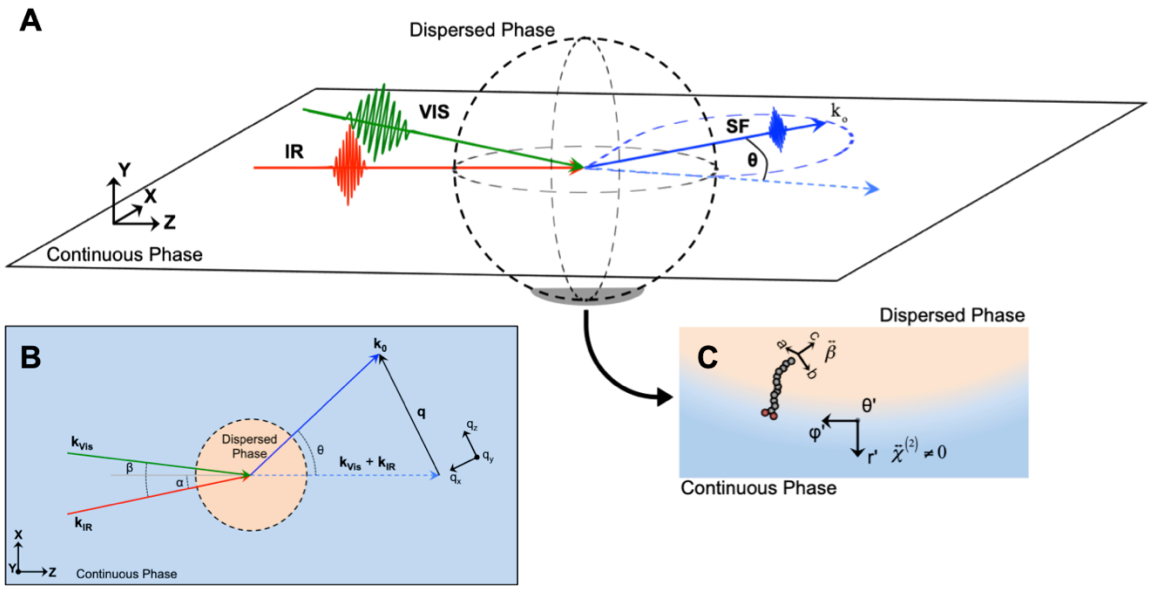

Figure 2.3. Illustration of the various reference frames of VSFSS. (A) Sketch of a generic nanoparticle placed at the origin of the x, y, z coordinate system. (B) Top down of the xz-plane illustrating the rotated lab frame. (C) Up close view of a surfactant molecule at the nanoemulsion surface depicting the relationship between the molecular reference frame and the nanoemulsion surface reference frame.

Beginning with the laboratory reference frame, the nanoemulsion is placed at the center of this coordinate system (x, y, z) with a radius R. The scattering plane (xz-plane), is defined by the plane in which the visible ($\boldsymbol{k}_{Vis}$) and infrared ($\boldsymbol{k}_{IR}$) beams propagate. The z-axis of the scattering plane is set by the phase-matched direction ($\boldsymbol{k}_{Vis} + \boldsymbol{k}_{IR}$). The infrared beam is incident on the nanoemulsion at an angle, α, from the phase-matched direction and with an angle, β, between it and the visible beam. The sum-frequency wavevector ($\boldsymbol{k}_0$) lies within the scattering plane at an angle, θ, from the phase-matched direction. The beam vectors ($\boldsymbol{k}_0$, $\boldsymbol{k}_{Vis}$, $\boldsymbol{k}_{IR}$) can be expressed within the scattering plane as follows, where **x**, **y**, and **z** are the unit vectors for the laboratory frame.

$$\begin{bmatrix} \boldsymbol{k}_0 \\ \boldsymbol{k}_{Vis} \\ \boldsymbol{k}_{IR} \end{bmatrix} = \begin{bmatrix} k_0 \sin\theta & 0 & k_0 \cos\theta \\ -k_0 \sin(\beta - \alpha) & 0 & k_0 \cos(\beta - \alpha) \\ k_0 \sin\alpha & 0 & k_0 \cos\alpha \end{bmatrix} \begin{bmatrix} \boldsymbol{x} \\ \boldsymbol{y} \\ \boldsymbol{z} \end{bmatrix}$$

(2.12)

The most efficient way to describe the scattering process, however, is via the scattering vector (**q**), defined in relation to the phase-matched direction by $\boldsymbol{q} = \boldsymbol{k}_0 - (\boldsymbol{k}_{Vis} + \boldsymbol{k}_{IR})$. It follows, then, that $|\boldsymbol{q}| = 2k_0 \sin\frac{\theta}{2}$. This reference frame is often referred to as the rotated lab frame within the scattering formalism developed by Roke and co-workers. The rotated lab frame, and thus scattering vector, can be calculated from the unit vectors of the original laboratory frame via the rotational transformation in equation 2.13.

$$\begin{bmatrix} \boldsymbol{q}_x \\ \boldsymbol{q}_y \\ \boldsymbol{q}_z \end{bmatrix} = \begin{bmatrix} -\sin\frac{\theta}{2} & 0 & -\cos\frac{\theta}{2} \\ 0 & 1 & 0 \\ \cos\frac{\theta}{2} & 0 & -\sin\frac{\theta}{2} \end{bmatrix} \begin{bmatrix} \boldsymbol{x} \\ \boldsymbol{y} \\ \boldsymbol{z} \end{bmatrix}$$

(2.13)

This transformation relates the unit vectors for the rotated lab frame, ($\mathbf{q}_x$, $\mathbf{q}_y$, $\mathbf{q}_z$) to the unit vectors for the laboratory frame.

The next transformation provides the necessary connection between the scattering vector and the nanoemulsion surface. Spherical coordinates make the most logical choice for defining the surface of a nanoemulsion droplet. Therefore the nanoemulsion reference frame is defined by r', θ', and φ' coordinates, where r' is the axis perpendicular to the interface pointed out from the surface of the dispersed phase towards the continuous phase. The nanoemulsion surface coordinates can be calculated from the rotated lab frame using equation 2.14.

$$\begin{bmatrix} \boldsymbol{e}_{r\prime} \\ \boldsymbol{e}_{\theta\prime} \\ \boldsymbol{e}_{\varphi\prime} \end{bmatrix} = \begin{bmatrix} \sin\theta'\cos\varphi' & \sin\theta'\sin\varphi' & \cos\theta' \\ \cos\theta'\cos\varphi' & \cos\theta'\sin\varphi' & -\sin\theta' \\ -\sin\varphi' & \cos\varphi' & 0 \end{bmatrix} \begin{bmatrix} \boldsymbol{q}_x \\ \boldsymbol{q}_y \\ \boldsymbol{q}_z \end{bmatrix}$$

(2.14)

For the nanoemulsion surface, $\boldsymbol{e}_{r\prime}$, $\boldsymbol{e}_{\theta\prime}$, $\boldsymbol{e}_{\varphi\prime}$ are the unit vectors.

The final transformation that needs to be developed describes the relationship between the nanoemulsion surface frame and the molecular frame, where the molecular hyperpolarizability ($\beta^{(2)}$) exists. The unit vectors of the molecular frame are **a**, **b**, and **c**. These unit vectors are calculated from the unit vectors of the surface frame via three Euler angles (φ_ν, θ_ν, ψ_ν), similar to traditional reflection geometry VSFS.

$$\begin{bmatrix} \boldsymbol{a} \\ \boldsymbol{b} \\ \boldsymbol{c} \end{bmatrix}$$

$$= \begin{bmatrix} -\sin\psi_\nu\sin\varphi_\nu + \cos\theta_\nu\cos\varphi_\nu\cos\psi_\nu & \sin\psi_\nu\cos\varphi_\nu + \cos\theta_\nu\sin\varphi_\nu\cos\psi_\nu & -\cos\psi_\nu\sin\theta_\nu \\ -\cos\psi_\nu\sin\varphi_\nu - \cos\theta_\nu\cos\varphi_\nu\sin\psi_\nu & \cos\psi_\nu\cos\varphi_\nu - \cos\theta_\nu\sin\varphi_\nu\sin\psi_\nu & \sin\psi_\nu\sin\theta_\nu \\ \sin\theta_\nu\cos\varphi_\nu & \sin\theta_\nu\sin\varphi_\nu & \cos\theta_\nu \end{bmatrix} \begin{bmatrix} \boldsymbol{e}_{r\prime} \\ \boldsymbol{e}_{\theta\prime} \\ \boldsymbol{e}_{\varphi\prime} \end{bmatrix}$$

(2.15)

Through these four coordinate transformations the coordinate system of molecules at the nanoemulsion surface can be probed using lasers beams whose polarization vectors are defined in the laboratory frame.

Revisiting equation 2.11, we re-express the sum-frequency amplitude with a particle susceptibility that is referenced to the laboratory frame coordinates.

$$E_0(\omega) \propto \left(\sum\nolimits_{\alpha_0\alpha_1\alpha_2} \Gamma^{(2)}_{\alpha_0\alpha_1\alpha_2}(\omega) \prod\nolimits_{i=0}^{2} \left(\boldsymbol{q}_{a_i} \bullet \boldsymbol{u}_{i,l} \right) \right) E_{IR} E_{vis}$$

(2.16)

where i = 0, 1, 2 correspond to the sum-frequency, visible and infrared beams, respectively. The summation index α_i corresponds to the laboratory frame coordinates (x, y, z), $\boldsymbol{q}_{a_i}$ the unit vectors of the rotated lab frame, and $\boldsymbol{u}_{i,l}$ is the unit polarization vector corresponding to beam "i" with polarization l. Given the beams propagated through the scattering plane (xz-plane), the polarizations are defined parallel (P) or perpendicular (S) to this plane. Mathematically, these polarization vectors are defined as

$$\begin{bmatrix} \boldsymbol{u}_{0,p} \\ \boldsymbol{u}_{1,p} \\ \boldsymbol{u}_{2,p} \end{bmatrix} = \begin{bmatrix} \cos\theta & 0 & \sin\theta \\ \cos(\beta-\alpha) & 0 & \sin\beta-\alpha \\ \cos\alpha & 0 & \sin\alpha \end{bmatrix} \begin{bmatrix} \boldsymbol{x} \\ \boldsymbol{y} \\ \boldsymbol{z} \end{bmatrix} \tag{2.17}$$

for a P polarized beam, and

$$\begin{bmatrix} \boldsymbol{u}_{0,s} \\ \boldsymbol{u}_{1,s} \\ \boldsymbol{u}_{2,s} \end{bmatrix} = \begin{bmatrix} 0 & 1 & 0 \\ 0 & 1 & 0 \\ 0 & 1 & 0 \end{bmatrix} \begin{bmatrix} \boldsymbol{x} \\ \boldsymbol{y} \\ \boldsymbol{z} \end{bmatrix} \tag{2.18}$$

for a S polarized beam.

The particle susceptibility can be expanded in terms of the spherical coordinates of the nanoemulsion surface.

$$\Gamma^{(2)}_{\alpha_0\alpha_1\alpha_2}(\omega) = \sum\nolimits_{c_0c_1c_2} \int d\boldsymbol{r}'^3 \left[\chi^{(2)}_{c_0c_1c_2}(\omega)\delta(|\boldsymbol{r}'|-R)e^{-i\boldsymbol{q}\bullet\boldsymbol{r}'} \prod\nolimits_{i=0}^{2} \left(\boldsymbol{e}_{c_i} \bullet \boldsymbol{q}_{a_i}\right) \right] \tag{2.19}$$

The coordinates (c_i) correspond to the nanoemulsion surface coordinates and the volume integral integrates the second-order surface susceptibility ($\boldsymbol{\chi}^{(2)}$) over the spherical coordinate system. The angular limits of integration for this integral are the typical limits for spherical integration. That is [0, π] and [0, 2π] for θ' and φ', respectively, while the

radial limits of integration are [0, R], where R is the particle radius. Upon visual inspection of the particle susceptibility, one can easily see the integral's surface selectivity in the delta function, $\delta(|\boldsymbol{r}'| - R)$. Calculation of the sum-frequency electric field (E_0) can be analytically solved using equation 2.19 and the preceding transformations between reference frames and polarization definitions.

Depending on the structure of the particle interface, the non-zero polarization combinations will change. The scattering formalism has been worked out in detail for numerous particle systems with chiral and achiral interfaces[84] and for arbitrarily shaped droplet forms (such as a nanohorse).[88] The nanoemulsion droplets exclusively focused on by this thesis are spherical droplets that possess achiral interfaces. For such an interface only the SSP, SPS, PSS, and PPP polarization combinations of the sum-frequency, visible, and infrared beams will result in a non-zero sum-frequency signal from the droplet surface.[84] As this dissertation exclusively makes use of the SSP and PPP polarization combinations, only their electric field expressions will be written out and the reader is referred elsewhere for the SPS and PSS polarization combinations.[84]

$$E_{SSP} \propto \cos\left[\frac{\theta}{2} - \alpha\right] \Gamma_2^{(2)} \tag{2.20a}$$

$$E_{PPP} \propto \cos\left(\frac{\theta}{2}\right)\cos\left(\frac{\theta}{2} - \alpha\right)\cos\left(\frac{\theta}{2} - \alpha + \beta\right)\Gamma_1^{(2)} + \cos\left(\frac{\theta}{2} - \alpha\right)\cos(\theta - \alpha + \beta)\,\Gamma_2^{(2)} + \cos(\theta - \alpha)\cos(\theta - \alpha + \beta)\,\Gamma_3^{(2)} + \cos(\beta)\cos\left(\frac{\theta}{2}\right)\Gamma_4^{(2)} \tag{2.20b}$$

The various susceptibility particle susceptibility components $\Gamma_i^{(2)}$ in equations 2.20a and 2.20b are expressed as:

$$\Gamma_1^{(2)} = \Gamma_{\perp\perp\perp}^{(2)} - \Gamma_{\parallel\parallel\perp}^{(2)} - \Gamma_{\parallel\perp\parallel}^{(2)} - \Gamma_{\perp\parallel\parallel}^{(2)} \tag{2.21a}$$

$$\Gamma_2^{(2)} = \Gamma_{\parallel\parallel\perp}^{(2)} \tag{2.21b}$$

$$\Gamma_3^{(2)} = \Gamma_{\parallel\perp\parallel}^{(2)} \tag{2.21c}$$

$$\Gamma_4^{(2)} = \Gamma_{\perp\parallel\parallel}^{(2)} \tag{2.21d}$$

where the ∥ and ⊥ indicate the parallel and perpendicular directions relative to the plane tangent to the scattering vector (***q***). Therefore, ∥ is perpendicular to the q_z axis while ⊥ is parallel to q_z.

Connecting the particle susceptibility to surface susceptibility for the molecules studied in this dissertation, equation 2.19 will yield

$$\begin{bmatrix} \Gamma_1^{(2)} \\ \Gamma_2^{(2)} \\ \Gamma_3^{(2)} \\ \Gamma_4^{(2)} \end{bmatrix} = \begin{bmatrix} 2F_1 - 5F_2 & 0 & 0 & 0 \\ F_2 & 2F_1 & 0 & 0 \\ F_2 & 0 & 2F_1 & 0 \\ F_2 & 0 & 0 & 2F_1 \end{bmatrix} \begin{bmatrix} \chi_1^{(2)} \\ \chi_2^{(2)} \\ \chi_3^{(2)} \\ \chi_4^{(2)} \end{bmatrix}$$

(2.22)

Similar to the particle susceptibility components written above, the surface susceptibility components are expressed as:

$$\chi_1^{(2)} = \chi_{\perp\perp\perp}^{(2)} - \chi_{\parallel\parallel\perp}^{(2)} - \chi_{\parallel\perp\parallel}^{(2)} - \chi_{\perp\parallel\parallel}^{(2)}$$

(2.23a)

$$\chi_2^{(2)} = \chi_{\parallel\parallel\perp}^{(2)}$$

(2.23b)

$$\chi_3^{(2)} = \chi_{\parallel\perp\parallel}^{(2)}$$

(2.23c)

$$\chi_4^{(2)} = \chi_{\perp\parallel\parallel}^{(2)}$$

(2.23d)

When considering the surface susceptibility components, $\parallel$ and $\perp$ are referenced to the surface coordinate system with $\parallel$ being parallel to θ' and φ', and $\perp$ being parallel to the nanoemulsion's radial axis (r'). F_1 and F_2 in equation 2.22 are the scattering form functions. Relevant to the nanoemulsions in this dissertation, Roke et al. have solved

these form functions for second-order scattering under the Rayleigh-Gans-Debye approximation.[84]

$$F_1(qR) = 2\pi R^2 i\left(\frac{\sin(qR)}{(qR)^2} - \frac{\cos(qR)}{qR}\right) \tag{2.24a}$$

$$F_2(qR) = 4\pi R^2 i\left(3\frac{\sin(qR)}{(qR)^4} - 3\frac{\cos(qR)}{(qR)^3} - \frac{\sin(qR)}{(qR)^2}\right) \tag{2.24b}$$

were $q \equiv |\boldsymbol{q}|$, the magnitude of the scattering vector, and R is the nanoemulsion radius. The Rayleigh-Gans-Debye approximation only holds when the index of refraction of the dispersed phase is close to that of the continuous phase. Mathematically this can be expressed as $qR(1-m) \ll 1$,[89] where m is the relative refractive index between the dispersed and continuous phase. This approximation holds for the nanoemulsion studied here, which use various combinations of the following solvents for the dispersed and continuous phases: H_2O, D_2O, hexadecane, isooctane, and CCl_4.

Finally, the relationship between the surface susceptibility and the molecular hyperpolarizability for the nanoemulsions studied here is expressed. Similar to planar interfaces, the spherical nanoemulsion droplet surface is considered isotropic with respect to the azimuthal angle.

$$\begin{bmatrix}\chi_1^{(2)}\\ \chi_2^{(2)}\\ \chi_3^{(2)}\\ \chi_4^{(2)}\end{bmatrix} = \frac{N\langle\cos(\phi_{mol})\rangle}{2}\begin{bmatrix}5D-3 & 0 & 0 & 0\\ 1-D & 2 & 0 & 0\\ 1-D & 0 & 2 & 0\\ 1-D & 0 & 0 & 2\end{bmatrix}\begin{bmatrix}\beta_1^{(2)}\\ \beta_2^{(2)}\\ \beta_3^{(2)}\\ \beta_4^{(2)}\end{bmatrix}$$

(2.25)

Equation 2.25 calculates the surface susceptibility elements for N number of molecules at the nanoemulsion surface, with an average molecular tilt angle of ϕ_{mol} relative to interfacial normal, and an orientational parameter $D = \frac{\langle \cos^3(\phi_{mol}) \rangle}{\langle \cos(\phi_{mol}) \rangle}$. As stated above, the hyperpolarizabilities belong to the molecular coordinate system and the separate $\boldsymbol{\beta}^{(2)}$ elements are expressed as:

$$\beta_1^{(2)} = \beta_{ccc}^{(2)} - \beta_2^{(2)} - \beta_3^{(2)} - \beta_4^{(2)}$$

(2.26a)

$$\beta_2^{(2)} = \frac{\left(\beta_{aac}^{(2)} + \beta_{bbc}^{(2)}\right)}{2}$$

(2.26b)

$$\beta_3^{(2)} = \frac{\left(\beta_{aca}^{(2)} + \beta_{bcb}^{(2)}\right)}{2}$$

(2.26c)

$$\beta_4^{(2)} = \frac{\left(\beta_{caa}^{(2)} + \beta_{cbb}^{(2)}\right)}{2}$$

(2.26d)

The connection between the molecular level information in the molecular reference frame to the macroscopic laboratory frame has been outlined for sum-frequency scattering experiments. The interested reader is referred to other sources for more detail

regarding second-order nonlinear scattering theory, such as electric field expressions for additional polarization combinations, non-Rayleigh-Gan-Debye formalisms, and non-spherical and arbitrary particle shapes.[69, 84-86, 88, 90-91] It is worth pointing out, as the molecular reference frame has just been considered, that the Raman and IR selectivity mentioned with respect to planar sum-frequency experiments is also relevant at the molecular level of the scattering formalism. Vibrational modes interrogated by VSFSS need to be both Raman and IR active for generation of a non-zero sum-frequency response. Before detailing the experimental systems used to perform second-order nonlinear scattering experiments, the fitting routine used in all vibrational sum-frequency analysis will be briefly discussed.

Spectral Fitting for Interpreting Sum-Frequency Experiments

Sum-frequency spectroscopy, in both the reflection and scattering experimental geometries, is a coherent spectroscopic technique where $\boldsymbol{\chi}^{(2)}$ and $\boldsymbol{\Gamma}^{(2)}$ are complex and the non-resonant and resonant components all have associated phases and amplitudes. Sufficient interpretation of sum-frequency experiments requires a robust fitting technique to account for the interferences between non-resonant and resonant components. This is illustrated in equation 2.27, where the measured intensity is proportional to the square of the sum of the various contributions that will lead to constructive and destructive interferences.

$$I_{SF}(\omega) \propto \left|A_{NR}e^{i\phi_{NR}} + A_{R,1}e^{i\phi_{R,1}} + A_{R,2}e^{i\phi_{R,2}} + \cdots + A_{R,n}e^{i\phi_{R,n}}\right|^2 \tag{2.27}$$

Whereas with linear vibrational spectroscopies that are simply a superposition of separate vibrational modes, interpretation of sum-frequency spectra needs to account for the interferences between contributing modes. The fitting routine used to appropriately interpret sum-frequency spectra within this dissertation was first implemented by Moore et al.[92]

$$\left|\chi^{(2)}\right|^2 = \left|A_{NR}e^{i\phi_{NR}} + \sum_n \int_{-\infty}^{\infty} \frac{A_n e^{i\phi_n} e^{-\left[\frac{\omega-\omega_n}{\Gamma_{G,n}}\right]^2}}{\omega - \omega_n - i\Gamma_{L,n}} d\omega\right|^2 \tag{2.28}$$

In equation 2.28 the non-resonant response is described by a frequency independent amplitude (A_{NR}) with an accompanying phase (ϕ_{NR}). The resonant modes are described a convolution of a Lorentzian and Gaussian lineshapes, originally described by Bain,[93] in order to account for the homogenous broadening inherent to the vibrational transition and inhomogeneous broadening arising from the local chemical environment, respectively. For each of the n vibrational modes, the fitting routine assigns an amplitude (A_n), a phase (ϕ_n), a frequency (ω_n), a Lorentzian width ($\Gamma_{L,n}$), and a Gaussian width ($\Gamma_{G,n}$). It is important to note that the fitting routine was originally applied to planar sum-frequency spectra and ignores the angular dependence of a scattered sum-frequency response. However, it is still valid so long as the angle of detection (θ) does not change during sum-frequency measurements and any size dependent influences on the sum-frequency intensity have been accounted for.

Second-order spectroscopy fits are known to be non-unique,[94] and using five fitting parameters per resonant feature, along with the two parameters for the non-

resonant contribution, necessitates a consistent approach to limiting the number of variables allowed to float in the fits. To achieve this, the phases of the non-resonant and all resonant modes were chosen to be either 0 or π to characterize the relative phase relationship between vibrational modes (i.e. constructive or deconstructive). The Lorentzian line widths were all fixed at values that are consistent with their typical vibrational lifetimes.[95-97] Therefore, the only values that were permitted to vary are the non-resonant and resonant amplitudes, the center frequencies, and the Gaussian widths. When available, literature values from previous studies are used to provide reasonable initial guesses and constraints, which are later relaxed. For planar sum-frequency spectra, the non-resonant amplitude has been shown to be negligible at the oil-water interface. This is likely the result of similar magnitude non-resonant responses for both the oil and aqueous phases, but possessing opposite phases.[83] So for the planar sum-frequency experiments reported here the non-resonant amplitude was also set to 0.

CHAPTER III

EXPERIMENTAL DETAILS

This chapter details the experimental systems for both the scattering and reflection sum-frequency experiments. Brief descriptions and background are provided for supplementary techniques, which were used to characterize nanoemulsions size and charge, surfactant surface activity.

Vibrational Sum-Frequency Scattering Laser System

For all vibrational sum-frequency scattering (VSFSS) experiments a picosecond visible pulse and femtosecond, broadband, infrared pulse were used to excite the sum-frequency response at nanoemulsion surfaces.

In order to create the pulses required for our VSFSS experiments, a Libra-HE regenerative amplifier (Coherent, USA) was used to generate a 800 nm beam, which was used to generate the infrared pulse and as the visible beam in VSFSS experiments. The Libra amplifier incorporates a Vitesse (Coherent, USA) oscillator that outputs 800 nm seed pulses at a 80 MHz repetition rate. These seed pulses are temporally stretched using a diffraction grating based pulse stretcher before being injected into the amplification cavity. An Evolution pump laser (Coherent, USA), outputting a 15 W 532 nm pulse, was used to amplify the seed pulses in a Ti:Sapphire gain medium. Amplified pulses are dumped out of the amplification cavity into a diffraction grating based pulse compressor.

The resulting amplified beam is directed out of the Libra amplifier at a 1 kHz repetition rate, a power of 3 W, and pulse width of < 100 femtoseconds.

The amplified 800 nm beam is then split, using a beam splitter, sending the majority of the beam to pump an OPERA-SOLO 2 (Light Conversion, USA) optical parametric amplifier (OPA) to generate the infrared pulses. The stability of the 800 nm beam alignment into the OPA is monitored using a beam profiler. This profiler was positioned at the far end of the table, measuring the 800 nm light leaking through the first mirror the 800 nm beam hits after passing through OPA.

Within the OPA, generation of the infrared pulse begins with the 800 nm being split again, with ~ 5% of the light sent to a sapphire crystal to generate a white light continuum. In this pre-amplification step, the white light continuum is spatially chirped and then overlapped with a portion of the 800 nm beam inside a BBO nonlinear crystal. Signal and idler beams are generated out of this crystal, via optical parametric generation, alongside other beams from higher order nonlinear processes. All beams except for the signal beam are blocked, which is subsequently overlapped in a second BBO crystal with the majority of the 800 nm beam from earlier. This second BBO crystal is used to create a new, amplified, signal/idler pair at ~100x the power of the pre-amplification signal/idler pair. These signal/idler beams are recombined in a GaSe crystal in order to generate the infrared beam via a difference frequency generation process. This infrared beam is then passed through a Ge infrared filter and then directed out of the OPA box for use in VSFSS experiments. By controlling the WLC timing during the pre-amplification step and tuning the nonlinear crystal angles, infrared light with wavelengths between 3-10 μm can be generated.

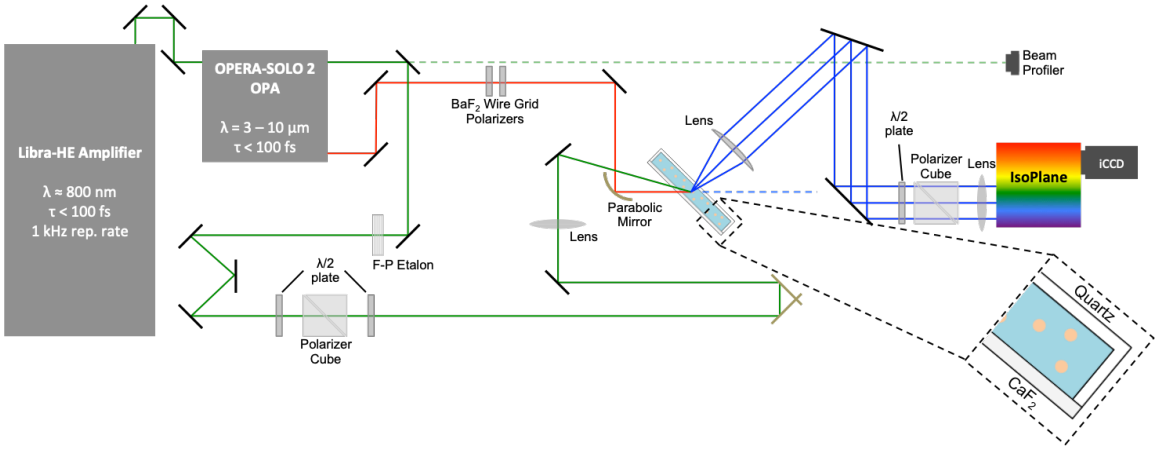

Figure 3.1. Diagram of the experiment system (not to scale) used for nanoemulsion surface spectroscopic studies.

Modeled after experimental systems described in literature,[35, 68, 75] Figure 3.1 provides a schematic of the homebuilt VSFSS experimental system used within this dissertation, and uses the aforementioned visible and infrared beams for generation of a sum-frequency response off nanoemulsion samples. The portion of the 800 nm beam split off inside the OPA, and passed through, is hereafter referred to as the visible beam. he visible beam is pulse shaped using a Fabry-Pérot (F-P) Etalon and then passed through a half-wave (λ/2) plate – polarizer cube – λ/2 plate setup to control for beam power and polarization. The visible beam is then reflected off of a gold retroreflector, which is used to adjust the beam's path length, before being focused behind the sample cuvette (spot size ~500 μm). The broadband infrared beam is frequency selected for the vibrational region of interest and is generated from the OPA horizontally polarized, P-polarization for these experiments. It passes through two BaF_2 wire grid polarizers before being

focused down to a spot size of ~80 μm using a 90˚ off-axis gold parabolic mirror (50 mm focal length (FL)), with the beam's focus being placed inside the sample cuvette.

Unless otherwise noted, the sample cuvette for all VSFSS experiments consists of a CaF_2 entrance window (CeNing Optics) with a quartz cuvette back (Helma QS). All quartz cuvette backs used here have an optical path length of 200 μm. A cuvette holder (Helma QS) was used to hold these cuvettes and was fixed in place using a home built mount to prevent shifting of the cuvette position during scans.

For all experiments reported in this dissertation, the visible and infrared beam enter the sample cuvette with an opening angle of 20˚ and the scattered sum-frequency signal was detected at an angle of 60˚ from the phase-matched direction. The phase-match direction was determined by measuring the SFG transmission from a nonlinear MgO:LN crystal (P/N MLN5100-SFG(I)-UC). To collect the scattered sum-frequency signal, a plano-convex lens (20 mm FL) was used to collimate the scattered signal. The sample cuvette was angled so that the back window and collection lens were parallel with each other. The sum-frequency signal is passed through a λ/2 plate – polarizer cube setup to filter and select the desired polarization. Another lens (100 mm FL) was used to focus the collimated light into a spectrometer (IsoPlane; Princeton Instruments) that spectrally disperses the sum-frequency signal onto an intensified CCD (PIMAX 4, Princeton Instruments).

At the beginning of each day the experimental system was aligned and the detection line set using a reference sample. The first sample run each day was a standard sample, to gauge instrument performance and for use in data normalization in order to allow for a robust comparison of data taken on different days. Early VSFSS experiments

monitoring the signal intensity from standard samples found negligible changes over the course of the day, as long as the room temperature did not fluctuate more than 1 ˚F. Thus, for later experiments, the standard sample is only smeasured at the start of the day. For every measured sample, a series of 3 signal scans and 3 background scans, where the visible and infrared beams are de-timed from each other, are taken in alternating order (signal-background-signal-…). Unless otherwise noted, each spectra shown in this thesis is an average of at least 3 background subtracted and normalized spectra, reproduced on a minimum of 3 unique samples.

Reflection Vibrational Sum-Frequency Laser Systems

The laser systems used for reflection geometry vibrational sum-frequency experiments, to study the planar oil-water interface, have been reported in previously literature[98-101] and theses.[102-103] Thus, herein, only a brief description of the two laser systems used will be provided, with further details to be found in previous publications. Before describing the laser systems, the sample cell will be described, as the sample cell geometry used with both laser systems was the same.

A custom built sample cell used for all studies on the CCl_4 – $H_2O(D_2O)$ interface was machined from a solid piece of Kel-F. A CaF_2 window was used for the incident window and a BK7 glass window was used for the window that out-going beams exited. Both windows were sealed using Dupont Kalrez perfluoropolymer o-rings. The Kel-F sample cell, both windows, and o-rings were all cleaned in an acid bath and copiously rinsed before use. Before any surfactant solutions were added to the sample cell, the

water spectrum of the neat CCl_4 – H_2O was taken to ensure the cell was clean. All data have been normalized to a non-resonant signal generated off a gold mirror and are the average of at least 300 shots/wavelength. Each spectra shown was replicated with a minimum of three unique samples.

For the first VSFS laser system, more complete descriptions can be found in the relevant publications.[98-99] It is based on a commercially available sum-frequency system by Ekspla (Lithuania). The laser possesses a oscillator that generates a 1064 seed pulse created by a flash-lamp pumped Nd:YAG rod. These pulses are generated at a 10 Hz repetition rate, ~600 μJ/pulse, and have 30 picosecond pulse lengths. This beam is frequency doubled to 532 nm, with a portion sent to the interface for VSFS experiments and the rest is recombined with the original 1064 beam to generate a tunable infrared beam inside an OPO/OPG/DFG setup. Depending on the crystal installed at the DFG stage, the tunable infrared can have a wavelength between 2.5 – 10 μm. For the experiments reported in this dissertation, the DFG crystal used in this laser system was a $AgGaS_2$ crystal.

To generate sum-frequency at the planar oil-water interface the visible and infrared beams were overlapped at the interface with pulse energies of 80 μJ and 80 – 250 μJ, respectively. The angles of incident were set near total internal reflection for the CCl_4 – H_2O interface. Polarization selection of the visible beam was performed using a λ/2 plate/Glan-Taylor polarizer combination. A periscope was used to change the infrared polarization as needed. Sum-frequency signal generated from the planar interface was polarization selected with another λ/2 plate/Glan-Taylor polarizer setup and

detected using a monochromator (model MS2001) and photomultiplier tube (PMT, Hamamatsu R7899).

This laser system was used to measure VSFS spectra of the CH stretching and water stretching vibrational regions (2700-3700 cm^{-1}) when the surfactants AOT and CTAB were adsorbed to the CCl_4 – $H_2O(D_2O)$ interface.

The second VSFS laser system used to study molecular behaviors at the planar oil-water interface is also described in previously publications.[101, 104] Similar to the first, it is based on a commercially available sum-frequency system by Ekspla (Lithuania). A flash-lamp pumped Nd:YAG rod generates a 1064 seed pulse, similar to the first laser system. However, the repetition rate of this laser is 50 Hz. A similar OPO/OPG/DFG process is used to generate the infrared pulses with this laser system, and at similar wavelengths and energies as well. A $AgGaS_2$ crystal was used for experiments using shorter infrared wavelengths, whereas a GaSe crystal was used for experiments at longer infrared wavelengths. Polarization selection of the visible and infrared beams was done using a $\lambda/2$ plate/Glan-Taylor polarizer setup and periscope, respectively. Beam angles incident upon the interface were near total internal reflection. Detection of the sum-frequency response from the interface was also done using another monochromator/PMT setup.

This laser system used a bottom up approach, propagating the visible and infrared beams through the CCl_4, to measure VSFS spectra in the D_2O stretching region of the neat CCl_4 – HOD and CCl_4 – D_2O interfaces. It was also used in experiments performed in a top-down geometry, where a thin layer of octane was placed on top of a D_2O sub-

phase. The experimental cell used in top down experiments was milled out of Kel-F and subjected to the same cleaning procedures as the other experimental cell. Top down experiments were performed with this laser system to measure the SO vibrational stretch of the surfactant AOT at the planar oil-water interface.

Nanoemulsion Sample Preparation and Glassware Cleaning Procedures

The creation of bare low charge nanoemulsions, as will be seen later on, necessitates rigorous cleaning procedures. Therefore, only glass containers were used to store solutions and samples. The cleaning procedures used with all glassware is described first, with general nanoemulsion preparation described second.

All glassware is copiously rinsed by ultrapure water (18.2 MΩ•cm resistivity) before being placed in a concentrated sulfuric acid bath that contained NOCHROMIX (Godax Labs, inc.) for a minimum of 12 hours. After this initial acid bath, glassware was rinsed again with ultrapure water before being placed into a second, "isolated", acid bath. Glassware was required to go through the previous rinse – acid bath – rinse procedure before entering the isolated acid bath. After the second acid bath, all glassware was copiously rinsed one more time before being dried in a drying oven and stored in dust free containers until use. These preparation procedures were consistent with previous preparation procedures necessary to measure high quality water stretching spectra at the planar oil-water interface, absent impurities.[66, 105]

As mentioned in the introduction, nanoemulsions require an input of energy to break up the droplet size into the appropriate size range. To achieve this, high-energy

ultrasonication was used to create all nanoemulsions discussed here. The specifics of how different nanoemulsion samples were created will be discussed in later chapters and in the context of the studies being performed. In general, however, the dispersed phase was kept relatively dilute at 1 – 2% vol./vol. and the emulsifier of interest was dissolved in the continuous phase at the desired concentrations. For studies involving changes to pH or ionic strength, those changes were made to the aqueous continuous phase.

Dynamic Light Scattering

Dynamic light scattering (DLS) was used to characterize nanoemulsion droplet size distributions and calculate the average droplet size. A commercially available Zetasizer Nano ZS (Malvern, UK) was used to perform all DLS experiments. In order to characterize nanoemulsion sample sizes, a cuvette filled with nanoemulsion samples is irradiated by a continuous wave HeNe laser (633 nm, 4 mW). A photodetecter placed at an angle of ~175˚ detects the backscattered radiation off nanoemulsions samples, tracking the intensity fluctuations as a function of time. Nanoemulsions move through solution via Brownian motion where the droplet speed through solution is related to the particle size using the Stokes-Einstein equation. Analyzing the time-dependence of the light intensity scattered off of particles moving in solution, using a correlation function, allows for a determination of the particle size.

Electrophoretic Mobility and Zeta Potential

Most of the nanoemulsions studied here possess some sort of charge at their surfaces, with the identity of the charge carrier being dependent upon the system. Quantification of charge at nanoparticle interfaces is typically accomplished using electrophoretic mobility (EpM) measurements. The true surface charge cannot directly be determined for the nanoemulsion surface due to the distribution of ions around a charged particle in an aqueous solution. Instead, the zeta potential (ZP) is calculated from the EpM measurements. Provided here is a brief overview of the structure of the electric double layer surrounding colloids, how ZP is related to the EpM, and a description of the typical EpM experiment.

Illustrated in Figure 3.2 is the distribution of ions around a nanoemulsion. Extending from the charged interface into the bulk solution, the composition and structure of this ion distribution is referred to as the electric double layer. Closest to the charged droplet surface is the Stern layer, where ions are considered firmly bound to the surface. Outside the Stern layer is the diffuse layer, where ions are more diffusely distributed, the electric potential is often modeled as to exponentially decay with distance from the droplet. As nanoemulsions move through solution, due to Brownian motion, the ions and solvent molecules that are more firmly bound to the droplet surface will move with the droplet. The firmly bound ions screen the surface charge, reducing its magnitude. Within the diffuse layer is an imaginary “slipping plane” that defines the boundary between ions and molecules that move with the particle and those that do not. The ZP is defined as the potential difference across the slipping plane.

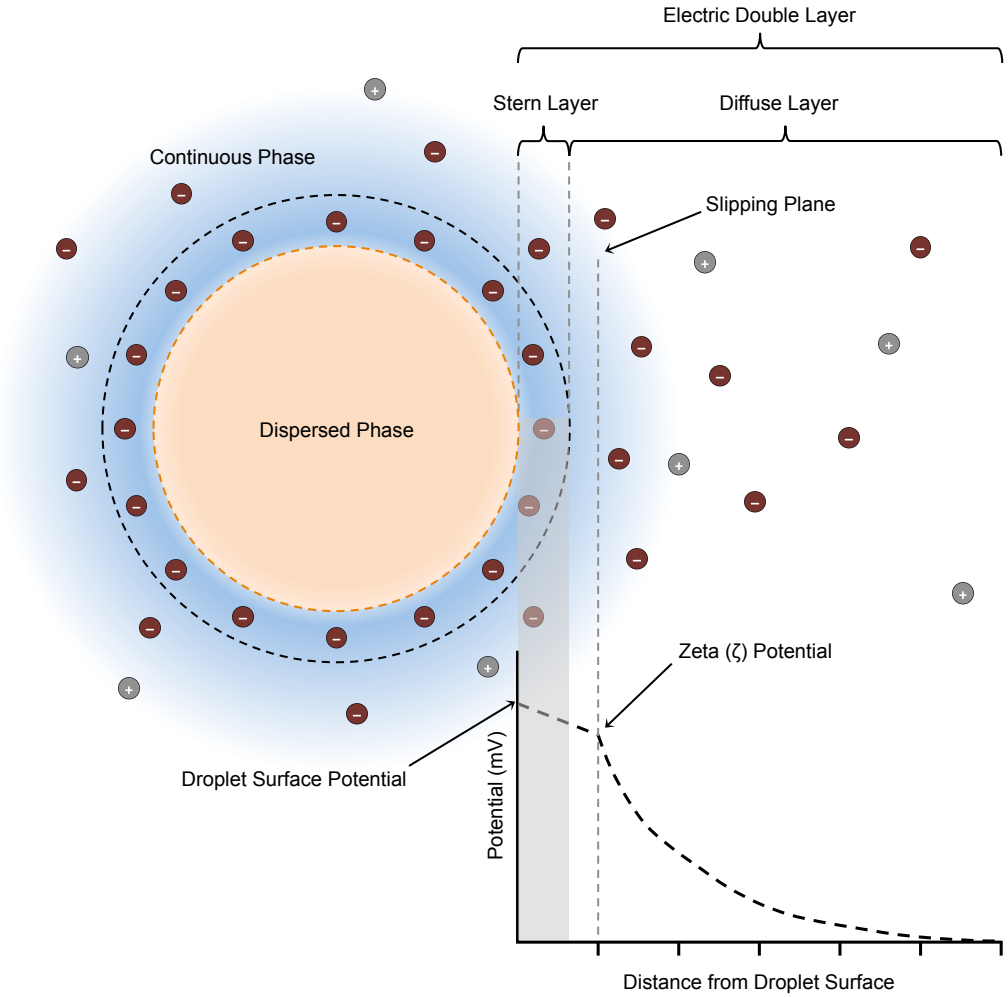

Figure 3.2. An illustration of the distribution of ions around nanoemulsions. Included are representations of definitions of different components of the electric double layer and how the electric potential changes with distance from the droplet. Image was adapted and recreated from a similar image appearing in the Malvern Zetasizer manual.

During an EpM experiment, the electrophoretic mobility (μ) is measured when nanoemulsions move with a constant velocity (v) in the presence of a uniform external electric field (E_{ex}). This is expressed in equation 3.1.

$$\mu_{EpM} = \frac{v}{E_{ex}} \tag{3.1}$$

This velocity is experimentally determined using laser Doppler velocimetry (LDM), which calculates the nanoemulsion velocity from the frequency shift of the backscattered radiation. The EpM is calculated from this velocity and is then inserted into Henry's formula (equation 3.2) to calculate the electrokinetic potential, i.e. the zeta potential (ζ).

$$\mu_{EpM} = \frac{2\varepsilon\zeta f(\kappa\alpha)}{3\eta} \tag{3.2}$$

This relationship between the ZP and the EpM is dependent upon the dielectric constant (ε), the solution viscosity (η), as well as Henry's function (f(κα)). Two values for Henry's function are typically used. For solutions with a background ionic strength of ~1 mM, or greater, Smoluchoski's approximation is appropriate, and f(κα) = 1.5. If the background ionic strength is low, then Huckel's approximation is used and f(κα) = 1. However, other values can be calculated between these two limiting cases with analytical expressions such as the Ohshima model.[106]

The Zetasizer Nano ZS (Malvern, UK) used for DLS experiments was also used to perform LDM experiments, hereafter referred to as EpM experiments. Disposable folded capillary cuvettes (polystyrene) were used to hold the nanoemulsion solutions during these experiments. A ZP standard (DTS 1235, Malvern) was used to verify the performance of our instrument. On our instrument the standard's measured ZP value was -43 mV, matching well with the reported value of -42 ± 4 mV. All ZP and EpM values reported herein are the average of at least 5 unique samples, with each sample being measured at least 10 times.

Interfacial Tensiometry

As seen in chapter 2, sum-frequency signal intensity is dependent upon both the number density of vibrational modes at the interface, as well as the average orientation of those vibrational modes. In order to decouple these sources of intensity changes in sum-frequency spectra, interfacial tensiometry is used. The interfacial tension is most susceptible to changes in the surface concentration of surface adsorbed molecules and its sensitivity to orientational changes is negligible. Thus, it provides an appropriate means of determining how the surface concentration of adsorbed molecules changes in different solution conditions. Interfacial tension measurements reported here were taken using two methodologies, pendant drop and Wilhelmy plate tensiometry.

The pendant drop tensiometry method was performed using a pendant drop tensiometer (KSV). CCl_4, used as a model hydrophobic phase, was placed in a quartz cuvette while the aqueous solution was placed in a syringe (1 mL Hamilton, gas-tight) with a hooked needle. All surfactants were placed in the aqueous phase. To determine the interfacial tension, an aqueous droplet was suspended in CCl_4 and a picture of the droplet was recorded at a fixed time interval until the interface had equilibrated, i.e. the interfacial tension no longer changed. Software, provided with the instrument, fits the droplet shape within each picture using the Young-Laplace equation. This fit determines the droplet shape factor, from which the interfacial tension can be calculated.

In Wilhelmy plate tensiometery, a thin platinum plate is suspended at the interface and the interfacial tension is calculated from the force applied to the plate. For these experiments either a CCl_4 subphase or a hexadecane top phase were used as the

hydrophobic phases. When the CCl_4 subphase was used, a neat aqueous layer (no surfactants) was placed on top of the subphase and the neat air-water surface tension was measured to ensure a clean experimental set up. If the neat air-water surface tension was ~72 mN/m, then the plate was lowered to the CCl_4 – H_2O interface until the surface tension value read ~ 44 mN/m. Finally, the appropriate amount of surfactant was diluted into the aqueous phase and the interfacial tension measured until the interface equilibrated. When hexadecane was used as the hydrophobic phase, the neat aqueous-hydrophobic interface was measured and then the aqueous subphase was replaced with the same volume of the desired solution.

Surface pressure is the chosen value to report results of interfacial tensiometry experiments. To calculate the surface pressure, the interfacial tension of the surfactant-coated interface is subtracted from the interfacial tension of the neat aqueous-hydrophobic interface. Thus, any decrease in the interfacial tension results in a rise in surface pressure. For all surface pressures reported within this dissertation, the surface pressure is referenced to a neat aqueous-hydrophobic value taken at the beginning of the day. Surface pressure values for a concentration series of the surfactant AOT was measured using both methods, with negligible differences in the results. Therefore, both methods used with simple surfactant systems are assumed to yield comparable observations and are used equivalently to provide insight into changes in surfactant surface population.

CHAPTER IV

BARE LOW CHARGE NANOEMULSION SURFACES

The bare aqueous-hydrophobic interface has long been understood to acquire a large negative charge despite the hydrophobic phase lacking any polarizable chemical groups. Debate over the identity of the charge carrier continues to the present day as conflicting conclusions are derived from "macroscopic" and molecularly specific experiments. This chapter describes a new approach to understanding the origins of the interfacial charge through the creation of low charge nanoemulsions (LCNE). The measured zeta potential at the LCNE surface is significantly smaller than previous studies and characterization of the pH dependence of the zeta potential, alongside surface spectroscopic measurements, indicate that the lower charge is a result of a minimization of surface impurities. With impurities minimized VSFSS is used to study the molecular features of the LCNE surface. These molecular characteristics are dissimilar to other published experiments on highly charge bare nanoemulsions. The LCNE surface possesses a measurable free OH vibration that provides evidence for stronger dispersion bonding interactions between interfacial water and oil molecules, compared to similar planar alkane-water interfaces. Upon adsorption of linear alkane surfactants the free OH vibration disappears and a reorganization of the hydrophobic phase is observed. Emma Tran assisted with the preparation of the LCNE samples reported here and Rebecca M. Altman carried out the comparative VSFS experiments. This chapter contains work that has been previously published.[107-108]

Introduction

Nanoemulsion stabilization is most often achieved through the use emulsifier mixtures composed of surfactants and polymers. These emulsifier blends are used to form mono- or multi-layer interfacial films at the droplet surface, which ultimately contribute to the droplet stability and can be tuned for specific application. Yet, in the absence of these stabilizing interfacial layers, a significant negative charge has been observed to spontaneously accumulate at the bare nanoemulsion surface.[42-43, 48, 73] Remarkably, this negative charge is sufficient to provide the necessary electrostatic repulsive force that prevents droplet coalescence[43] and, thus, stabilizes the bare nanoemulsion dispersion. This charging phenomenon is particularly notable because the hydrophobic phase in these studies lacks any polarizable groups that could easily explain the origins of this charge. Despite this charging behavior first being observed in the mid-1800's,[109] there is still no consensus on the identity of the charge carrier. This phenomenon is not unique to the bare nanoemulsion interface, but is ubiquitous across numerous aqueous hydrophobic interfaces. It has been observed at the bare air-water,[109-111] solid-water,[112] and self-assembled monolayer-water interfaces.[113-114] Thus, any potential charge carrier must provide a coherent description that can be generally applied to all these interfaces. Mainstream theories of the identity of a charge carrier that satisfy this condition, illustrated in Figure 4.1, include the adsorption of negatively charged ions,[42-43, 115-117] charge transfer mechanisms originating from asymmetric interfacial hydrogen-bonding environments,[74, 118-120] and surface adsorbed impurities.[46, 121-125]

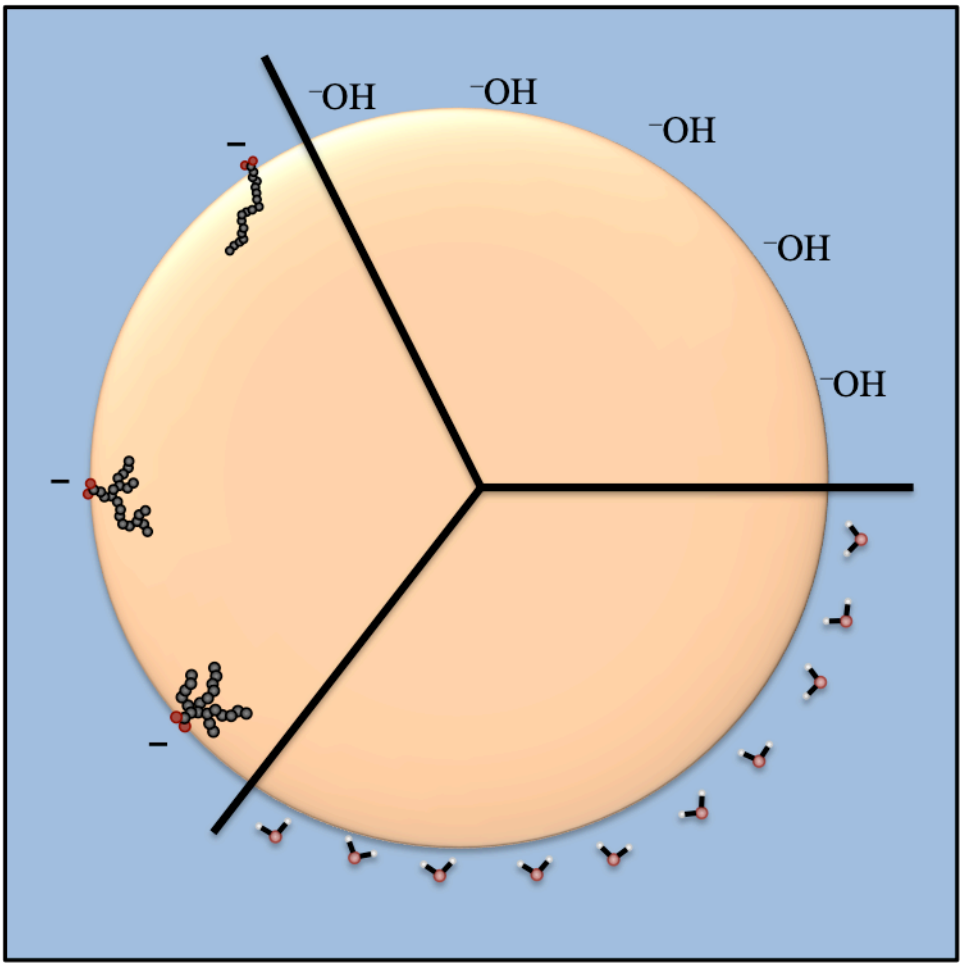

Figure 4.1. Illustration of potential sources of negative charge at bare aqueous-hydrophobic nanoemulsion interfaces. Moving clockwise from upper right, hydroxide ion adsorption, water dipole ordering, and trace surface impurities.

The most prominent explanation for the charging of aqueous-hydrophobic interfaces identifies the hydroxide ion as the charge carrier. Herein this will be referred to as the hydroxide hypothesis. It is believed that hydroxide ions preferentially adsorb to the aqueous-hydrophobic interface in significant amounts with an interfacial concentration reported to be 3 nm^2/hydroxide ion.[48] Electrophoretic mobility (EpM) and acoustophoretic mobility measurements on bare nanoemulsions, in addition to gas bubbles, have provided the majority of the evidence used to support this hypothesis.

From these measurements researchers calculate the zeta potential (ZP), the potential across the slip plane near the droplet surface. For bare nanoemulsions dispersed in neutral aqueous solutions are commonly measured to have ZP values greater in magnitude than -55 mV.[34, 42-43, 48, 73-74, 115] Extensive studies of the ZP's pH dependence suggest that it plateaus at the largest negative ZP when the pH > 10, and reaches an isoelectric point (ZP ~ 0) somewhere between a pH of 2 and 4, depending on the hydrophobic phase.[42-43] From these experiments the free energy of adsorption for the hydroxide ion was calculated to be ~25kT,[42-43] which is on the same order of magnitude of the adsorption free energy of simple ionic surfactants.[33] While those studies present compelling evidence for the adsorption of hydroxide ions, they are considered to "macroscopic measurements". That is, they do not provide molecularly specific information by directly probing the molecules at the interface.

Unfortunately for proponents of the hydroxide hypothesis, corroborating evidence is scant among studies using spectroscopic methods in an attempt to positively identify surface enhanced hydroxide ions. Support has recently been found in non-resonant second harmonic generation experiments of the planar aqueous-hexadecane interface performed by Gan et al., who calculated a ΔG_{ads} = -8.3 kcal/mol for hydroxide ions.[126] Despite being a surface specific technique, the non-resonant second harmonic experiments are still susceptible to other non-hydroxide ion contributions that the researchers may be unaware of. This point is made because other spectroscopic techniques, such as photoelectron spectroscopy[127] and vibrational sum-frequency spectroscopy (VSFS),[74, 128-130] are chemically specific and have both failed to identify any surface enhancement of hydroxide ions. Molecular dynamic simulations also provide

evidence contrary to the hydroxide hypothesis and suggest that if any acid/base ion is enhanced at the surface it is the proton.[127, 130-132] Importantly, it should not be suggested that all "macroscopic" experiments agree with the EpM measurements. Surface tension measurements of the air-acid/base solution interface have found that the surface tension is lowered for acidic solutions while surface tension is raised for basic solutions, relative to the neat air-water surface tension value.[133] Thus, surface tension suggests the hydroxide ion is actually repelled from the surface. While EpM and acoustophoretic mobility measurements of nanodroplets provide compelling evidence for the hydroxide hypothesis, additional studies suggest the charge carrier identity lies elsewhere.

Other common explanations beyond the hydroxide hypothesis include (bi)carbonate adsorption,[116-117] interfacial charge transfer resulting from ordered interfacial water molecules,[74, 118-120] and the presence of surface active impurities.[46, 121-125] Whereas it has been calculated that the pH dependent concentrations of (bi)carbonate species, originating from dissolved CO_2, could be consistent with the ZP trends,[116] early experiments sought to limit the dissolution of CO_2.[42] Thus, this explanation is unlikely. Alternatively, computational research has appeared over the last decade that has stimulated discussion about the possibility of charge transfer, due to ordered water dipoles, contributing to the measured ZP. VSFS studies of the water region have demonstrated water at hydrophobic surfaces is well ordered,[134-136] providing experimental support for these studies. However, the amount of charge that these charge transfer models contribute to the EpM measurements is highly dependent on where the slip plane is located[137] and only a single study, thus far, has calculated charge densities from interfacial water that could entirely account for the charge density found in

experiments.[120] In the last several years there has been a resurgence in both experimental and computational support for the notion surface-active impurities are the most likely source of interfacial charge.[46, 122-125] The suggestion of impurities is, understandably, vigorously denied with claims of intense measures taken to ensure system cleanliness and doubts that numerous labs across time and space could all experience issues with impurities.[70, 138] However, one only needs to look at other fields of research to find a similar struggle to limit the effects of impurities across the globe.[139-142]

This chapter reports the creation and study of bare low charge nanoemulsions. The creation of LCNE droplets possessing an average ZP of -10 ± 5 mV is shown to be result of stringent cleaning procedures that have previously been used to measure the most accurate VSFS spectra of interfacial water at the oil-water interface.[66] pH dependent EpM measurements of LCNE droplets suggest the lingering charge at these droplet surfaces is the result of residual surface-active impurities. VSFSS experiments of the interfacial water molecules at the LCNE droplet surface measure for the first time an unbound water oscillator, colloquially called the free OD, which is notably absent in spectra of high charged nanoemulsions. This interfacial water vibration provides evidence that the low ZP is not the result of surface impurities and suggests stronger oil-water bonding interactions exist at the nanodroplet interface compared to what is expected from planar oil-water studies. Using surfactants to tune the nanoemulsion charge, the free OD is observed to disappear and a reorganization of the interfacial hydrophobic phase is seen. The molecular behavior at the LCNE surfaces differs from what has been observed for nanoemulsions possessing higher charges, and the studies herein highlight the effects trace impurities can hold.

Electrophoretic Mobility of Low Charge Nanoemulsions

A distinguishing feature of bare LCNE droplets is their low ZP compared to bare nanoemulsions previously reported in literature. Under neutral pH conditions previously reported bare hexadecane nanoemulsions typically possess ZP values ranging from -55 to -90 mV.[34, 42-43, 48, 73-74, 115] Bare LCNE droplets are classified in this dissertation as bare nanoemulsions possessing an average ZP of -10 ± 5 mV under neutral pH conditions. Interestingly, some LCNE samples incorporated into that average value possessed ZP values within error of zero. These ZP values were calculated from the EpM data using the Hückel approximation in order to account for similar length scales for the Debye screening length and the droplet diameter. These low ZP values were replicated for LCNE samples prepared in H_2O, D_2O, and HOD aqueous phases. Confidence can therefore be had that swapping the aqueous phase won't affect the ZP and we can use these aqueous phases interchangeably for spectroscopy purposes later on. It is surprising that with such low surface charges these nanoemulsions are marginally stable. Conventional classification would assign our LCNE samples ($|ZP| < 30$ mV) as unstable. While phase separation was witnessed before the end of the day for the samples that had zeta potentials within error of zero, DLS measurements found that the average LCNE sample remained sub-micron for several days. This marginal stability will be returned to shortly, as pH dependent EpM measurements discussed below provide clues to why this is the case.

In order to create LCNE droplets, attention had to be given to glassware cleaning procedures and solvent storage conditions. The cleaning procedure used to clean glassware used in LCNE preparation are the same as the procedures that are demonstrably necessary to measure accurate water spectra at the planar oil-water interface.[66, 105]

This cleaning procedure was outlined in Chapter III and will be hereafter be referred to as the "isolated cleaning procedure." The sensitivity of ZP was tested to solvent storage conditions and cleaning procedures, the results of which are displayed in Figure 4.2 alongside a range of literature ZP values. Bare nanoemulsions prepared in glassware cleaned via the isolated cleaning procedure (Figure 4.2, blue bar) possess the lowest ZP values of all the solution conditions tested. If the isolated cleaning procedure was abandoned, and a "used" acid bath was used to clean the glassware used in bare nanoemulsion preparation, then a higher average ZP is measured (Figure 4.2, purple bar). Notably, the effects of the isolated cleaning procedure are null if the aqueous phase was store in polyethylene containers. Bare nanoemulsions prepared with an aqueous phase that had been stored for up to a week in polyethylene containers, but prepared in glassware cleaned with the isolated cleaning procedure, possessed the highest and most variable ZP of all samples prepared (Figure 4.2, orange bar). While all reported values for bare nanoemulsions prepared in this work are lower than the range of previously reported values (Figure 4.2, black bar), the sensitivity to cleaning procedures is significant.

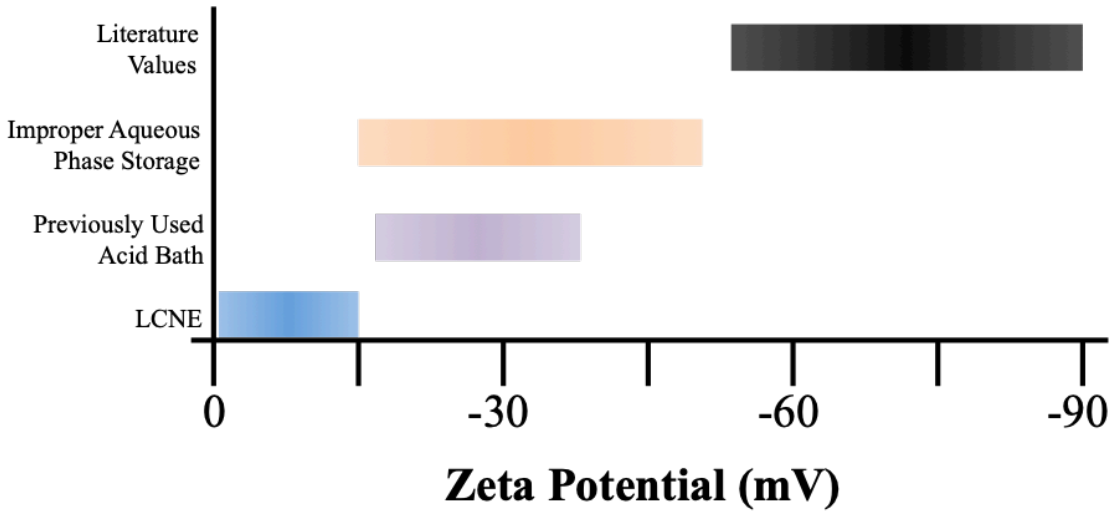

Figure 4.2. Zeta potential ranges for LCNE samples (blue), nanoemulsions prepared in glassware cleaned with used acid baths (purple), aqueous phase stored in polyethylene containers (orange), and the literature values for bare hexadecane nanoemulsions (black).

It should be mentioned that all new glassware was used in the studies that resulted in the creation of bare LCNE samples. No conclusion can be drawn if new glassware is necessary for others to follow suit in the creation of LCNE samples, as the control tests required to draw such a conclusion were, unfortunately, not performed. However, after several cleaning cycles using the isolated cleaning procedure, LCNE samples could still be formed using the previously new glassware. What can be concluded, though, is that the ZP of bare nanoemulsions is clearly sensitive to the solvent storage conditions and glassware cleaning procedures. It would stand to reason that when these conditions are relaxed that impurities could be the source of the higher negative charge. No attempt is made to identify the source or chemical identity of impurities present in the high charged bare nanoemulsion samples found in literature, as that would be pure speculation. However, given the appearance impurities are minimized at the LCNE surface, pH

dependent EpM studies of these samples could provide meaningful data into whether or not evidence supporting the hydroxide hypothesis can be reproduced at LCNE surface.

Presented in Figure 4.3a are the results from EpM measurements of LCNE droplets dispersed in different pH environments. Initial LCNE samples were made with a 2% vol./vol. hexadecane phase before being diluted to 1% vol./vol. The final solutions were pH adjusted using DCl (99.9% D, CDN Isotopes) or NaOD (99.8% D, CDN Isotopes) and possessed a constant NaCl concentration (10 mM). The pH was determined by dropping nanoemulsion solutions onto pH strips (range: 0 – 14, Merck KGaA). The EpM of LCNE droplets (Figure 4.3a, red trace) is found to largely be invariant to changes in pH when pH > 5 before rapidly decreases towards zero under more acidic conditions. LCNE data is presented alongside data extracted from a previous study, by Roger et al, of bare hexadecane nanoemulsions made with 99% pure (Figure 4.3a, blue trace) and 99.8% pure (Figure 4.3a, green trace) hexadecane.[121] Roger et al. concluded that the difference between the curves can be attributed to trace impurities in the oil phase that adsorb to the droplet surface upon dispersion of the hexadecane. In order to support their claim, they doped nanoemulsion solutions prepped with 99.8% pure oil with 5.8 mM oleic acid as a model fatty acid impurity (Figure 4.3a, orange trace). In light of that study, the drastically reduced EpM values for LCNE would indicate that impurity levels at LCNE samples are minimized beyond the impurity levels observed in previous studies. What then, is the source of the residual negative charge at the LCNE surface?

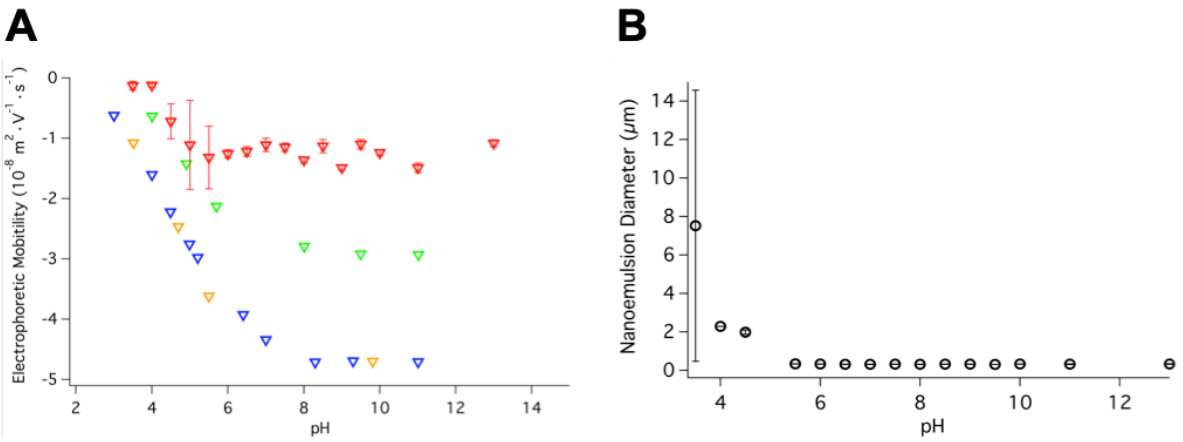

Figure 4.3. The (A) electrophoretic mobility for LCNE droplets dispersed in different pH environments (red). These are plotted alongside values extracted from Roger et al for samples prepared with 99% pure (blue) hexadecane, 99.8% pure (green) hexadecane, and 99.8% pure hexadecane deliberately contaminated with carboxylic acids. (B) The size of the LCNE samples was also measured as a function of solution pH.

The lingering charge at LCNE surfaces is proposed to be the result of carboxylic acid-like surface impurities. These impurities could be originating from the oil phase,[121] as no attempt was made to clean it as others have done,[138, 143] or it could be originating from some other source. This speculation is supported by previous work investigating the pH dependent behavior of carboxylic acid surfactants at the planar oil-water interface.[98] There it was found that the deprotonated carboxylate species occupied the oil-water interface above a pH of 6. A diffuse deprotonated carboxylic monolayer at the droplet surface could give rise to the invariant surface charge observed for the LCNE samples above pH 6. As the pH falls below 6, larger variations are seen in the LCNE EpM data. This is attributed to a mixture of protonated and deprotonated carboxylic acid impurities, which would result in acid-anion complex formation at the LCNE droplet surface and larger variations in the EpM values. The narrow pH range in which larger variations of EpM values are observed is consistent with the narrow pH range observed

for the formation of fatty acid vesicles resulting from acid-anion complexes.[144] As the LCNE solution pH becomes more acid, pH < 4, the proposed diffuse carboxylic acid-like monolayer will become primarily protonated. As a result, any protonated carboxylic acids at the droplet surface will be unable to provide a stabilizing electrostatic force and any stabilizing surface tension affects will disappear.[98, 145] This process would result in droplet destabilization and growth as stabilizing forces disappear. For the LCNE samples discussed here, the droplet diameters are observed to rapidly increase from several hundred nanometers to microns as the pH falls and the EpM approaches zero (Figure 4.3b). Thus the pH responsiveness of the residual LCNE charge can be entirely explained by the presence of a diffuse carboxylic acid monolayer.

While carboxylic acid-like impurities can reasonably explain the charging behavior observed at LCNE surfaces, other potential explanations for this charging behavior should be considered. The adsorption of either (bi)carbonate or hydroxide ions would require a much more significant change in EpM values for the pH range 6-10.[43, 116] Instead, an invariance to pH in this range is observed for the LCNE EpM values. Thus, ion adsorption models cannot reasonably account for the pH dependent trends observed in the LCNE EpM data. Interfacial charging resulting from ordered interfacial water molecules is additionally unlikely. While it was proposed in the first LCNE study,[107] that stronger water-oil bonding interactions and the interfacial aqueous layer could be contributing to the LCNE droplet charge and thus its stability, in light of the pH dependent EpM results those contributions are most likely minimal. Charge transfer models supporting any significant contribution to ZP from water dipoles are hindered by assumptions of where the slip plane is placed.[137] As the true location of the slip plane

can't be positively identified, any rigorous assignment of a fraction of the ZP to water dipole ordering is limited. Furthermore, the pH dependence of these models hasn't been characterized. VSFS experiments measuring the water spectrum of the oil-water interface find negligible perturbations to interfacial water, even in extremely basic pH environments.[129] If water dipoles were responsible for the interfacial charge, one would expect a change in the water ordering upon changes to pH, and thus change to VSFS spectrum. Since there is negligible change to the VSFS spectra, contributions from water ordering are even more unlikely.

The notion that trace impurities are the origins of any lingering charge at the LCNE surface is the most likely explanation. This is consistent with the variation in ZP for different cleaning procedures and the large variation in reported ZP values for bare hexadecane nanoemulsions. Additionally, trace impurities could provide a consistent explanation for the observation of negative charge across many different aqueous-hydrophobic interfaces. Attempts to use VSFSS to directly detect a deprotonated carboxylate vibrational mode at the LCNE droplet surface, in basic conditions failed to identify such signal. Estimates of the amount of impurity necessary to give rise to the EpM behavior observed at aqueous-hydrophobic interfaces place the concentration in the nanomolar range.[123, 125] The surface area per molecule for these impurities would be large at the LCNE surface and far below the detection limits of VSFSS.[146] Given the pH dependent trends in the LCNE size data (Figure 4.3b), these surface impurities also assist in the providing the marginal stability observed for LCNE droplets.

Water Bonding at LCNE Surfaces

If the ZP of previously reported highly charged nanoemulsions is the result surface-active impurities, and impurities have been minimized at the LCNE surface, then there should be supporting evidence observable via surface spectroscopic methods. In particular, the water-stretching vibrational region is very sensitive to the presence of surface adsorbed chemical. Both non-ionic and ionic surfactants are known to perturb the bonding environment of interfacial water,[105, 107, 147-149] with nanomolar concentrations of added ionic surfactants having notable affects on the interfacial water spectrum.[105] A key defining feature of the bare oil-water interface is the vibrational resonance corresponding to a water vibrational mode that does not participate in any bonding interactions, hydrogen. Colloquially called the free OH, this oscillator is measured near 3700 cm^{-1} at the planar bare air-water interface[67, 134] and is observed to shift to 3670 cm^{-1} at the planar oil-water interface as a result of weak dispersion interactions between interfacial water and oil molecules.[67] VSFS experiments have shown that the sum-frequency intensity corresponding to the free OH vibrational mode will decrease with increasing surfactant adsorption through a reduction of available surface area and bonding interactions.[67, 105, 150] Concomitant with a loss of free OH intensity is a significant increase in the sum-frequency intensity at lower energies corresponding to highly coordinated water stretches experiencing increased hydrogen bonding interactions, hereafter referred to as "bound" stretches.

As a result of being able to pass the infrared laser through the oil phase, measuring the sum-frequency spectrum of interfacial water at the planar oil-water

interfaces is considerably more accessible compared to the nanoemulsion surface where one must pass the infrared beam through an aqueous continuous phase. The challenge for studying the interfacial water spectrum at bare LCNE surfaces is in trying to reduce bulk infrared absorption by the same molecules one is trying to measure at the droplet surface. In order to reduce the continuous phase absorption and still keep maximum possible number of measureable vibrational modes, a 50:50 mixture of H_2O:D_2O was used as the continuous phase. Mixtures of H_2O and D_2O will rapidly undergo proton exchange to form water molecules possessing one hydrogen atom and one deuterium atom, HOD. This reaction is governed by a known equilibrium constant of 4.[151] Herein, this 50:50 mixture will be simply referred to as HOD. At the ratio used here, the final aqueous phase composition will be 1:1:2 of H_2O:D_2O:HOD.

Aqueous phase VSFSS experiments were carried out in the deuterated water-stretching region (2200 – 2800 cm^{-1}) with a focus on measuring the spectral intensity above 2600 cm^{-1} in an attempt to measure the free OD, the deuterated analogue of the free OH. Despite growth of LCNE droplets over the course of days, on the time scale of these experiments (hours/sample) the droplet size was relatively unchanged. A vibrational resonance was observed in both the PPP and SSP polarization combination when VSFSS experiments were performed on deuterated hexadecane LCNE droplets using an infrared pulse centered at 2700 cm^{-1} (inset, Figure 4.4). This peak was normalized to both the non-resonant sum-frequency response out of a nonlinear crystal and the infrared transmission curve for the neat HOD mixture, to account for the frequency dependent absorption by the continuous phase (Appendix A). To obtain the transmission curve a thin film of HOD was placed between two CaF_2 windows and

measured by a FTIR spectrometer. After normalization the peaks appears more of a shoulder on top of a broad background (Figure 4.4).

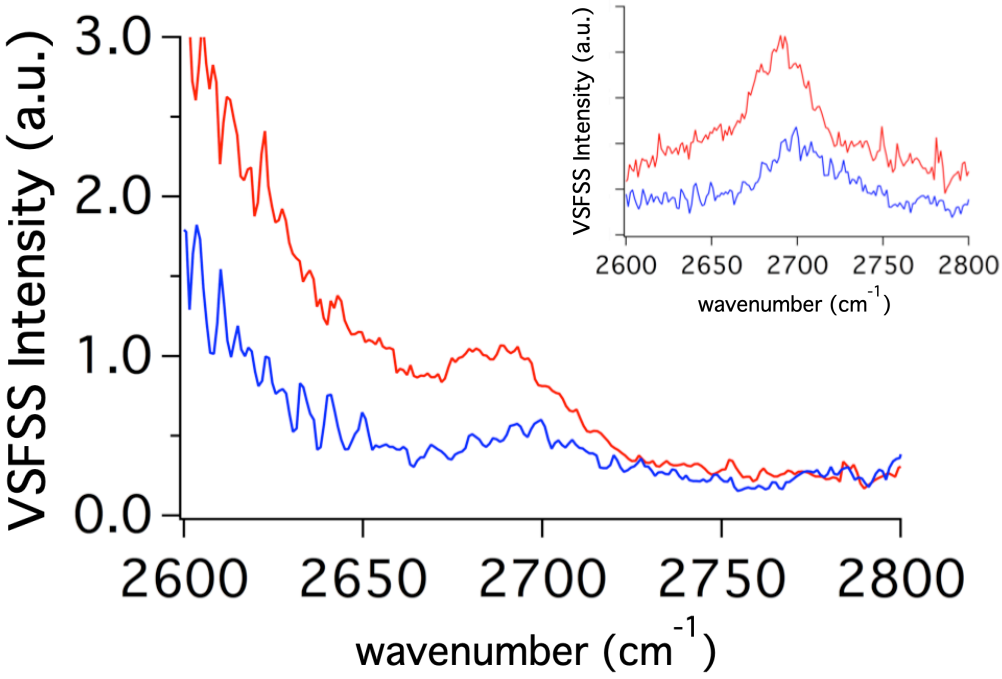

Figure 4.4. Free OD resonance at the LCNE surface measured in the SSP (blue) and PPP (red) polarization combinations. Inset shows the spectra prenormalization by the IR pulse profile and IR transmission spectrum of the continuous phase.

To confirm this resonance was originating from the LCNE surface, transmission VSFS experiments of the planar CaF_2-HOD interface were performed in the same spectral region. These experiments failed to identify any distinct resonance, thus the vibrational resonance is originating from the droplet surface. Within the measured frequency region, the only vibrational resonances that can be excited at the deuterated hexadecane LCNE samples surface are OD stretches from interfacial HOD and D_2O molecules. Thus, to assess the response of the peak seen in Figure 4.4 to adsorbed surfactants, VSFSS experiments were performed on surfactant covered (1 mM CTAB)

nanoemulsions. No distinct vibrational resonance was found for these samples and it appears that the vibrational resonance disappears at high surfactant concentrations. Thus, it is concluded the distinct vibrational peak display in Figure 4.4 is the free OD at the LCNE droplet surface. At the planar alkane-H_2O interface, a previous study found the bound OH stretches were more intense than the free OH.[152] Thus, the low sum-frequency intensity of the free OD relative to bound OD intensity would be consistent with what has been observed at the planar alkane-water interface. Unfortunately, a large amount of infrared absorption seen at lower energies prevents a strict analysis of the bound OD stretches at the droplet surface. Any specific conclusions as to the effect of impurities on this spectra region would be purely speculative, however it is likely that some of the elevated sum-frequency intensity relative to the free OD is due to the presence of trace impurities. Nonetheless, the presence of the free OD does permit some study of water bonding at the LCNE surface, despite not being able to draw many conclusions about the bound OD stretching region.

The observation of a free OD at the LCNE surface differs significantly from previously studies of water at nanoemulsion interfaces. One study used VSFSS to study water at the surface of surfactant stabilized water nanodroplets dispersed in oil.[75] In that study it was concluded the hydrogen bonding network of bound D_2O molecules was enhanced relative to the planar interface. They claimed that their droplet were representative of "hydrophobic" surfaces, however, they seemed to have failed to consider the impacts that the interfacial surfactants can have on changing the interfacial water structure, which would be seen in the sum-frequency spectra. The surfactant concentrations used in that study are above their CMC values, and multiple studies have

shown that high concentration of surfactants is going to have a significant impact on the water structure.[105, 149] As a result, no free OD was observed at the surfactant covered nano-water droplet surface. Another VSFSS study on higher charged nanoemulsion surfaces specifically stated that the free OD did not exist at the nanoemulsion surface.[74] The lack of free OD at the higher charged bare nanoemulsion surfaces is likely the result of surface-adsorbed impurities and is discussed later in more detail. The presence of the free OD at the LCNE surface supports the notion that impurities are minimized and, therefore, LCNE samples can be used to gain insight into the water-oil bonding interactions at bare nanoemulsion surfaces.

Although EpM measurements and the presence of the free OD present evidence surface impurities are the origin of the interfacial-charging phenomenon, the aqueous phase spectrum provides further evidence refuting the hydroxide hypothesis. If there were a significant concentration of hydroxide ions within the interfacial region, as has been suggested, the estimated area/hydroxide ion is 3 nm^2. [48] Previous computational work suggests that interfacial electric fields would induce a common ordering in any surface adsorbed hydroxide ions.[153-154] Therefore, a surface density of 3 nm^2/oriented hydroxide ion is above the detection limit of VSFSS.[146] However, no vibrational resonance corresponding to the deuterated hydroxide ion ($^-$OD) is observed near 2725 cm^{-1} in Figure 4.4.[74] Therefore, it is concluded the hydroxide ion does not possess a significant surface excess at the LCNE surface.

In order to aid in understanding which water vibrational modes are contributing to the droplet water spectrum, comparative studies were performed at the planar CCl_4-water interface. The hexadecane-water interface was not studied as the necessary experimental

redesigns to the planar VSFS experimental systems would have been particularly cumbersome to other group members. Previous work out of the Richmond lab has already established the differences of water in contact with CCl_4 and linear alkanes,[66-67, 152, 155] so the use of CCl_4 as a model hydrophobic phase does not prevent using the CCl_4-D_2O interface to aid in interpreting the hexadecane droplet water spectrum. Spectra for both pure D_2O and the HOD mixture in contact with CCl_4 are presented in Figure 4.5a. These spectra were taken in the PPP polarization combination because the PPP droplet spectrum provides a higher signal-to-noise ratio to analyze. The free OD is clearly seen in both spectra near 2700 cm^{-1}. Two peaks were used to fit the CCl_4-D_2O spectrum (Figure 4.5a, dark blue trace), which correspond to the bound water stretches and the free OD vibration. For the CCl_4-HOD spectrum (Figure 4.5a, light blue), a third peak was added to account for the presence of free OD oscillators from interfacial HOD and D_2O species. This is rationalized by previous VSFS experiments at the planar HOD-air interface that determined free OD oscillators from both HOD (free OD_{HOD}) and D_2O (free OD_{D2O}) molecules contribute to the sum-frequency spectrum of HOD mixtures.[156] Stiopkin et al. found that an uncoupling of the OD oscillators resulted in an ~ 17 cm^{-1} frequency shift for the free OD_{HOD} relative to the free OD_{D2O}. The presence of both free OD oscillators would explain the reduced intensity and broadening seen in the HOD spectrum compared to the D_2O.

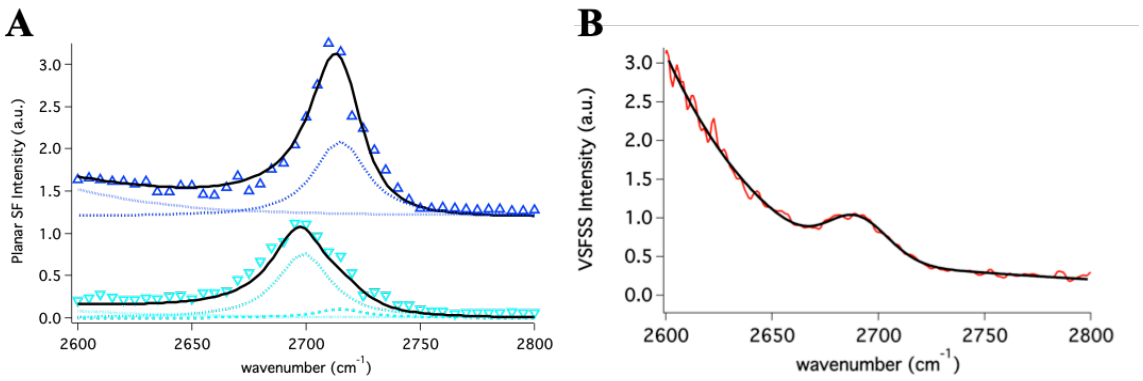

Figure 4.5. (A) Planar sum-frequency spectra (PPP polarization) of the D_2O – CCl_4 (dark blue, vertically offset) and HOD – CCl_4 (light blue) interfaces in high-energy OD stretching region (2600 – 2800 cm^{-1}). Spectral fits (black traces) are included alongside the individual contributing peaks (dashed lines). (B) LCNE PPP spectrum (red) and associated fit (black).

At the CCl_4-D_2O interface the free OD_{D2O} is found to have a center frequency of 2715 cm^{-1}. This value is 30 cm^{-1} lower than the free OD_{D2O} frequency at the planar air-D_2O interface (~ 2745 cm^{-1}).[156] A 30 cm^{-1} shift between the oil-D_2O and air-D_2O interfaces is consistent with the magnitude of frequency shift found between the oil-H_2O and air-H_2O interfaces.[67] These frequency shifts between the air-water and oil-water interfaces are the result of weak dispersion bonding interactions between the unbound water oscillator and the hydrophobic phase.[66, 152] At the planar CCl_4-HOD interface the free OD_{HOD} and free OD_{D2O} were fit to 2699 cm^{-1} and 2715 cm^{-1} respectively. A frequency shift of 16 cm^{-1} between the two peaks is remarkably consistent with the uncoupling of OD oscillators observed at the air-HO interface, so the lower frequency peak is assigned as the free OD_{HOD}. This assignment is supported by the fact the free OD_{HOD} is more intense in these fits than the free OD_{D2O}, the results of more HOD molecules being present in solution.

The results of the planar free OD peak frequencies are presented in Table 4.1 alongside the estimated planar HOD-hexadecane and the results from fitting the LCNE PPP spectrum (Figure 4.5b). Free OD values for the planar HOD-hexadecane are estimated from the differences between free OD frequencies at the CCl_4-H_2O and alkane-H_2O interfaces.[67] These estimated values are 2705 cm^{-1} and 2720 cm^{-1} for the free OD_{HOD} and freeOD_{D2O} resonances, respectively. Fitting the LCNE PPP spectrum determines the free OD frequencies to be 2690 cm^{-1} and 2703 cm^{-1} for the contributions arising from interfacial HOD and D_2O, respectively (Figure 4.5). These values correspond to a 15 cm^{-1} frequency shift between the planar and the nanodroplet oil-water interfaces.

Table 4.1 Free OD frequencies for the different oil-water water interfaces. Values are derived from fits to spectra using equation 2.28.

Interface	**Free OD_{HOD}**	**Free OD_{D2O}**
Planar CCl_4-D2O	N/A	2715 ± 1 cm^{-1}
Planar CCl_4-HOD	2699 ± 1cm^{-1}	2715 ± 1cm^{-1}
Estimated Planar hexadecane-HOD	2705 cm^{-1}	2720 cm^{-1}
LCNE Surface	2690 ± 5 cm^{-1}	2703 ± 5 cm^{-1}

To visually emphasize this frequency shift, VSFS was used to measure the vibrational spectrum of the planar CCl_4-HOD interface with 10 μM deuterated SDS added to the aqueous phase. This experiment was performed to (1) mimic the effects of contaminants at the oil-water interface and (2) to replicate the relative intensity between

the free OD and bound OD modes that is observed in the droplet spectrum. Displayed in Figure 4.6 are the results of the deuterated SDS experiments (green trace) and the LCNE spectrum, both recorded in the PPP polarization combination. The bare CCl_4-HOD interface is also presented to emphasize the effects of the SDS on the water spectrum. Comparing these spectra, the free OD frequency shift between the planar and droplet interfaces becomes visually apparent. A frequency shift of 15 cm^{-1} is large enough in magnitude to suggest there is a difference in strength of the dispersion bonding interactions between interfacial oil and water molecules at the droplet surface.

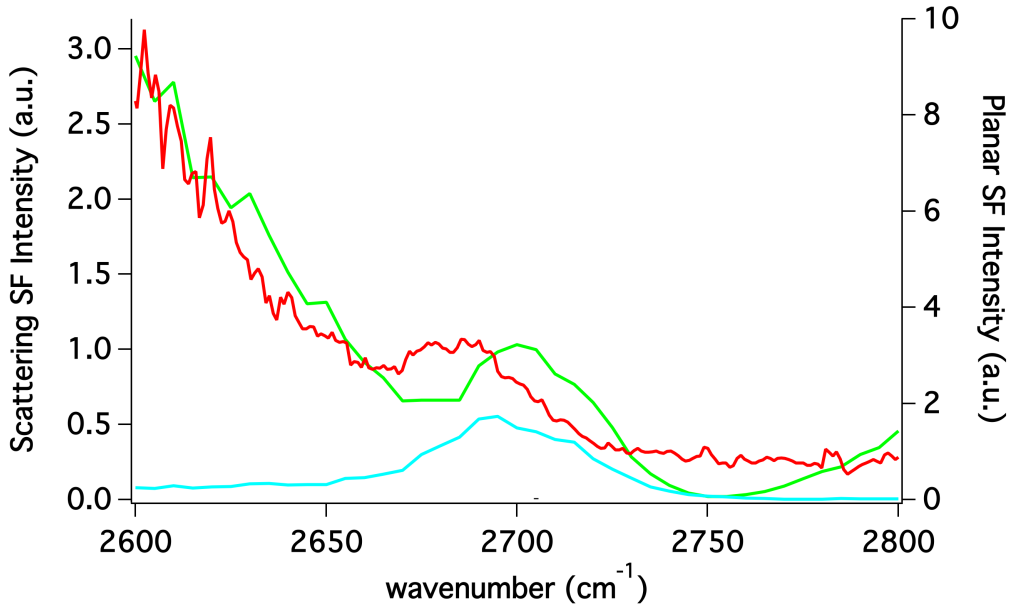

Figure 4.6. Side-by-side comparison of the free OD at the LCNE droplet surface (red, left axis), bare planar HOD–CCl_4 interface (light blue, right axis), and the HOD-CCl_4 interface in the presence of 10 μM deuterated SDS (green, right axis).

What are the physical origins leading to such a frequency shift? One possibility could be that differences in capillary waves at the planar and droplet interfaces are affecting the molecular level structural features at the oil-water interface and are leading to this frequency shift. Recent work at the planer air-water interface has suggested that

capillary waves can affect the orientational distribution of the free OH.[157] However, this is not a settled matter[158-159] and other work investigating the VSFS spectra of water adjacent alkyl self-assembled monolayers found negligible differences in the free OH compared to the planar alkane-water interface.[152, 155] At the self-assembled monolayer surface any capillary wave action should be damped out. Therefore, the likelihood that the free OH is frequency shifted as a result of differences in capillary wave action at the planar versus curved interface is unlikely.

A separate explanation for the observed frequency shift is that the interfacial hexadecane molecules create hydrophobic cavities whose structural features favor stronger dispersion interactions between the oil and water molecules at the LCNE surface. Previous simulations of the alkane-H_2O interface revealed an asymmetric vibrational line shape for the free OH, stretching towards lower frequencies.[152] The spectral intensity at lower wavenumbers suggests that there is a diverse population of unbound OH oscillators at an alkane-water interface with some participating in stronger dispersion bonding interactions. It has been shown that for one of water's OH bonds to be shielded from any hydrogen bonding at an alkane interface, the alkane surface must be rough on the atomic scale.[160] Thus, the hydrophobic cavities that are created by the alkane molecules at a roughened interface would provide the local chemical environment that shields the OH bond from participating in any hydrogen bonding interactions. It would follow that the hydrophobic cavities at the droplet and planar surfaces are different. A future test of this would be to measure the droplet free OD at a series of sizes and test whether the droplet frequency converges on the planar frequency as the radius of curvature grows.

Unfortunately, conclusions on the structural origins of the free OD frequency shift at the nanoemulsion surface are speculative at this time. It is important to note that the thermodynamic states of the planar and droplet interfaces are different. Whereas the planar interface is a thermodynamically stable state, the nanoemulsion surface is kinetically stable. Given that droplets are dispersed with an input of energy, and their surfaces necessitating some stabilizing force, this frequency shift could be a reflection of a difference in the thermodynamic state of these two different interfaces. Advanced simulations and further experiments are needed to connect the specific structural details or thermodynamic differences at the droplet hydrophobic phase to the intermolecular interactions.

LCNE Hydrophobic Phase Structure and Surfactant Perturbations

Given the minimization of impurities at the LCNE surface, these low charge droplets provide a unique chemical system to study the arrangement of hydrophobic molecules at the droplet surface in the absence of contaminants. VSFSS was used to measure the CH stretching region of LCNE samples made from hydrogenated hexadecane dispersed in D_2O. Any sum-frequency signal will originate from interfacial hexadecane molecules. Figure 4.7a includes the typical VSFSS spectrum of the bare LCNE droplet surface (grey trace) in the SSP polarization combination. The low level of signal intensity observed in the SSP polarization combination was also observed in VSFSS experiments performed in the PPP polarization combination,[107] however the number of experiments performed in the SSP polarization combination is more expansive

and so hereafter the analysis focuses on VSFSS experiments performed in the SSP polarization combination. The low level of signal intensity can't be the result of a lack of oil molecules at the bare oil droplet surface. Thus, it must be due to the lack of a common orientational ordering of the CH stretches at the droplet surface. It is proposed, here, that hexadecane molecules orient themselves parallel to the droplet surface. Such an orientational distribution of the hexadecane methylene vibrational dipoles would appear isotropic-like, with respect to interfacial normal, within the coherence length of the SFG process.[161] This structural arrangement would then lead to near complete cancelation of any sum-frequency intensity, unless there is a slight deviation of the molecular structures out of the interfacial plane. An slight upturn in the methyl groups relative to the interface could provide the necessary hydrophobic pockets for the free OD to appear[160] and result in a low signal intensity presented in Figure 4.7a. This proposed structural is consistent with the previous work of Fukuto et al., whose X-ray reflectivity and atomistic MD simulations concluded hexadecane molecules orient themselves mostly parallel to the hexadecane-water interface with a slight enhancement of methyl groups at the interface.[162] Other groups have concluded similar orientations for other linear alkanes at the bare n-alkane-water interface.[163-164] Thus, it is seems to be a general feature that interfacial alkane molecules position their alkyl chains primarily parallel with respect to the alkane-water interface.

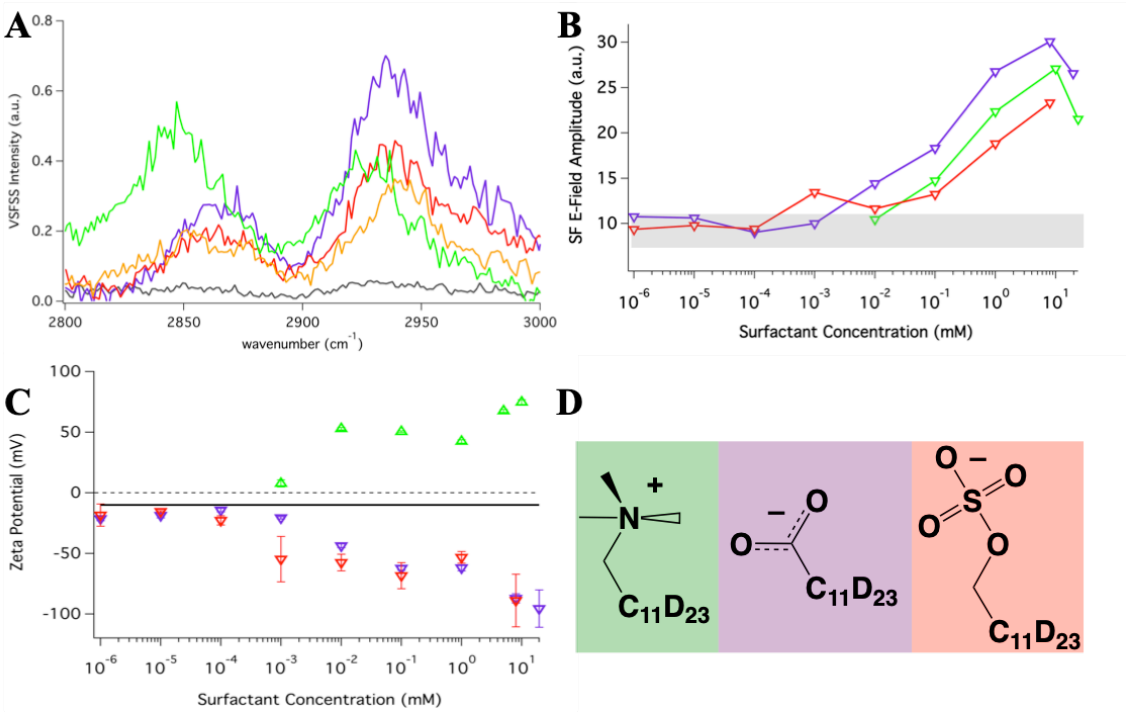

Figure 4.7. (A) VSFSS CH stretching spectra of interfacial hexadecane at the bare LCNE surface (grey) and in the presence of deuterated surfactants including SDS (red, 1 mM), KL (purple, 1 mM), DTAB (green, 1 mM), and DoOH (orange, 10 mM). For the ionic surfactants, the (B) integrated sum-frequency electric field amplitude is plotted as a function of surfactant concentration alongside the range of measured amplitude for the LCNE droplet (grey bar). (C) The zeta potential for these samples and the LCNE droplets (black line) are also provided with (D) the chemical structures of the ionic surfactants.

Alongside the bare LCNE droplet surface spectrum, Figure 4.7a displays the typical spectra for nanoemulsions prepared in the presence of deuterated n-alkyl ionic and nonionic surfactants. These included sodium dodecyl sulfate (SDS), potassium laurate (KL), dodecyltrymethylammonium bromide (DTAB) and n-dodecyl alcohol (DoOH). For the spectra displayed in Figure 4.7a, the bulk surfactant concentrations were 1 mM for the ionic surfactants and 10 mM for DoOH. All ionic surfactants were prepared by dissolving the surfactant in the aqueous continuous phase. Solubility issues prevented

DoOH being dissolved in the aqueous phase, therefore DoOH-stabilized nanoemulsions were prepared by adding the correct volume of DoOH to the pre-sonicated nanoemulsion solution. With the alkyl chains of the surfactants deuterated, the only contributions to the vibrational spectrum in Figure 4.7a are the interfacial hexadecane molecules.

The change in sum-frequency intensity observed in the SSP polarization combination between the bare LCNE spectrum and the surfactant-stabilized nanoemulsions is drastic. A similar rise in intensity of sum-frequency signal was also observed in the PPP polarization combination when surfactants adsorbed to the LCNE surface.[107] Assuming that the interfacial density of hexadecane doesn't change upon surfactant adsorption, the increased intensity can only be attributed to a reorganization of the hexadecane alkyl chains. Thus, it is concluded that interfacial hexadecane molecules undergo a structural reorganization upon adsorption of surfactant molecules to the droplet surface in order to maximize favorable Van der Waals interactions. The contributing vibrational modes to these spectra will be the methylene and methyl symmetric stretches, methyl Fermi resonance, and the methyl asymmetric stretches.[165-166] Unfortunately, a combination of a lack of spectral resolution and the non-uniqueness of fit parameters in second-order spectroscopies[94] makes sufficiently fitting these spectra with the known vibrational resonances difficult. However, there is no distinct sharp peak near 2875 cm^{-1}, assigned to the methyl symmetric stretch, that would be evidence of a primarily trans alkyl chain conformation for interfacial hexadecane molecules. This spectral feature was seen in low-temperature VSFSS experiments where it was taken as evidence of interfacial freezing.[167] The lack of a strong sum-frequency response corresponding to the methyl symmetric stretch indicates the reorganized hydrophobic phase is still conformationally

disordered at room temperature. Considering that surfactants molecules are known to be conformationally disordered at nanoemulsion interfaces,[35-36] a conformationally disordered interfacial oil layer is not surprising.

Upon visual inspection it would seem that the spectral shape of the oil phase spectra are different when compared to one another, which could be evidence that the different surfactants have different affects on the droplet oil phase. These spectral differences are most notable when comparing the deuterated DTAB spectrum to the deuterated SDS and KL spectra. However, the spectral differences between these spectra are can be accounted for by an interference of the vibrational modes with a higher-order $\chi^{(3)}$ response.[168] The manner in which a $\chi^{(3)}$ response interferes with vibrational modes will change with changes to the sign and magnitude of the interfacial potential. The change in the sign of the interfacial potential between the cationic and the anionic surfactants would manifest as a change in interference. This would be sufficient to explain why there is an elevated intensity at lower frequencies in the DTAB spectrum, while the elevated intensity is seen at higher frequencies in the SDS and KL spectra. A $\chi^{(3)}$ response can also explain the reason for the visual frequency shift in the maximum sum-frequency intensity perceived in these spectra. The slightly elevated intensity at the higher energy end of the anionic surfactant stabilized nanoemulsion spectrum, relative the non-ionic stabilized nanoemulsion, could also be explained by the presence of a $\chi^{(3)}$ response. The mechanism of $\chi^{(3)}$ interferences is illustrated further in Appendix B. It is concluded that the average hexadecane structure in the presence of anionic and cationic and nonionic surfactants are similar.

In order to further understand how surfactants perturb the LCNE hydrophobic phase the hexadecane sum-frequency amplitude was monitored as a function of ionic surfactant concentration. For these experiments, stock nanoemulsions were prepared with a 2% vol./vol. hexadecane phase and 2 nM added deuterated ionic surfactant concentration in the continuous phase. The final surfactant concentration for nanoemulsion samples was adjusted by diluting the stock nanoemulsion solution into D_2O solutions with the appropriate surfactant concentrations. The final volume fraction for all samples was 1% vol./vol. Using this dilution method, nanoemulsion droplet size changes between the original stock solution and the final solutions were observed to be negligible and had no effect on the VSFSS experiments. Displayed in Figure 4.7b is the square root of the integrated CH stretching sum-frequency intensity as a function of surfactant concentration. The square root of the sum-frequency intensity is taken to observe how the sum-frequency electric field amplitude coming from interfacial hexadecane molecules changes as a function of deuterated surfactant concentration. When the bulk surfactant concentration exceeds 10 μM, the sum-frequency electric field amplitude is observed to rise above the baseline value measured for LCNE droplet (grey band). The electric field amplitude is also observed to plateau as the bulk surfactant concentration approaches the surfactant's CMC. Comparing the results from these VSFSS experiments to ZP measurements of the surfactant-stabilized nanoemulsions, the increase in sum-frequency amplitude corresponds well to the changes in magnitude of the ZP for each ionic surfactant (Figure 4.7c). It is clear from these results that increases in hexadecane reorganization can be directly tied to increased surfactant adsorption at the droplet surface and occurs regardless of surfactant headgroup (Figure 4.7d).

While hexadecane reorganization at the nanoemulsions surface has been previously observed using VSFSS,[72] the results described here differ significantly from those previous studies. Low sum-frequency signal intensity was measured for the bare LCNE droplet surface (Figure 4.4a), but those previous studies measured a significant sum-frequency response for highly charged bare hexadecane nanoemulsion in the SSP polarization.[74] Additionally, different from the results discussed above, the previous studies observed a lack of change in signal intensity from the oil phase when anionic surfactants adsorbed to the droplet surface.[72] This was rationalized as a difference in how anionic and cationic surfactants assembled at the nanoemulsion surface. Importantly, the bare nanoemulsions reported in previous VSFSS studies possessed average ZP values of -55 mV. It would seem, then, that the origins of the surface charge could be affecting the hydrophobic structure of the bare hydrophobic phase. The high charge bare nanoemulsions of previous studies notably lacked a measurable free OD.[74] It is possible the lack of free OD is due to their experimental setup (infrared pulse center and D_2O continuous phase). However, the above studies of bare LCNE droplet surface studies would seem to suggest that these high charge nanoemulsion surfaces have surface impurities that are affecting their VSFSS results.

To test whether this is a reasonable conclusion, a series of aqueous phase VSFSS measurements were performed on nanoemulsions stabilized by various surfactant concentrations. The purpose of these experiments was to determine an approximate bulk surfactant concentration at which the free OD disappeared. Due to the long scan times (1 hour) for these experiments, the following procedure was used to estimate this concentration. At the start of the day, after the system was aligned, a free OD sample

would be measured. After a successful measurement of the free OD at the LCNE sample, a 1 mM SDS stabilized nanoemulsion sample (diameter ~ 300 nm) was measured. This was then replaced by a 100 μM SDS sample, followed by a 10 μM SDS sample, and finally a 1 μM SDS sample. This process was repeated several times and Figure 4.8 shows typical results from 10 μM SDS and 100 μM SDS. Despite the data being unnormalized, the free OD is clearly visible in the 10 μM sample and not the 100 μM sample. Thus, it would seem that the free OD disappears when the bulk surfactant concentration exceeds 10 μM. The corresponding ZP for 100 μM SDS stabilized nanoemulsion is near -50 mV. Thus it is reasonable that the lack of free OD and high charge in previous VSFSS studies is the result of surface impurities. This conclusion is supported by recent neutron and x-ray reflectivity experiments that identified trace impurities at the "bare" alkane-water interface.[46]

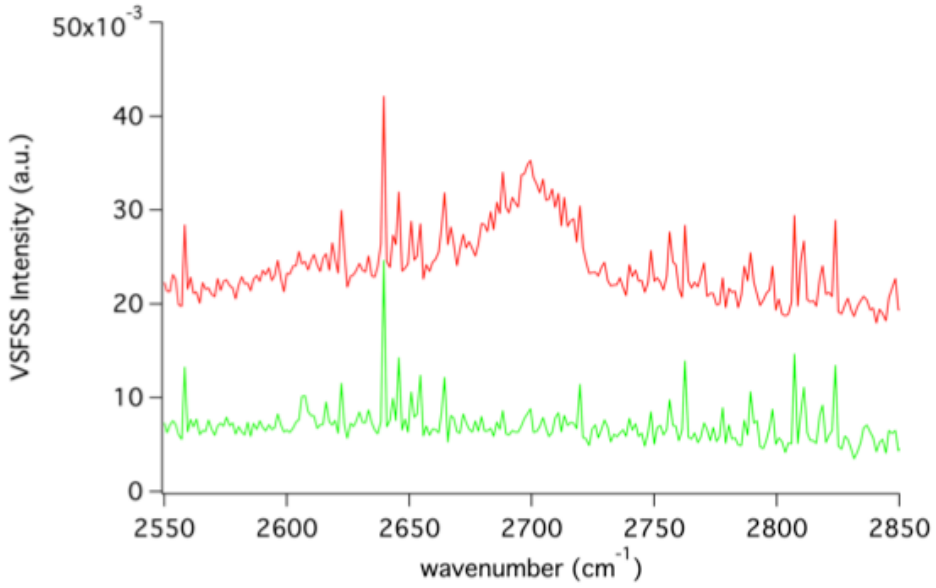

Figure 4.8. Unnormalized VSFSS spectra of the high-energy OD stretching region for nanoemulsions stabilized by 10 μM SDS (red, vertically offset) and 100 μM SDS (green).

It should be noted that there is a discrepancy between in surfactant density required to obscure the free OD. Tyrode et al. found the free OH only disappeared from the planar air-water interface when the area/surfactant molecule dipped below 0.65 nm^2.[149] At 10 μM bulk surfactant concentration, the area/molecule of surfactants at the nanoemulsion interface is much larger (~ 10 nm^2). Many more experiments of the aqueous phase at nanoemulsion surfaces are required to resolve this discrepancy. A standard sample is currently needed in order to compare spectra from taken on different days. This would allow more extensive measurements to be taken of individual surfactant concentrations and a more detailed analysis to be performed. However, the coincidence of the free OD disappearing at the same time the ZP approaches -50 mV provides strong evidence that surface adsorbates could be reorganizing the hydrophobic phase at high charge bare nanoemulsions. This would result in the large signal intensities observed via VSFSS and interfere with the adsorption of SDS, explaining the difference in hydrophobic reorganization observed between the anionic and cationic species.

Conclusions and Summary

The preparation and characterization of bare low charge nanoemulsions has been thoroughly detailed in this chapter. The zeta potential of bare nanoemulsions was shown to be susceptible to preparation and solvent storage conditions. EpM of LCNE droplets in different pH environments provide evidence that residual carboxylic acid-like surface impurities are responsible for the lingering surface charge. In order to verify the LCNE surface possessed minimal impurities, VSFSS was used to measure, for the first time, an

unbound OD oscillator at the nanoemulsion surface. The combination of the free OD alongside the EpM measurements demonstrates that the low charge at LCNE surfaces is not the result of cationic impurities. The lack of a vibrational resonance corresponding to the OD^- ion is notable, and indicates a lack of surface enhanced hydroxide ions. These experiments also provide further evidence to claims that surface-active impurities are the charge carrier responsible for charge accumulation at aqueous-hydrophobic interfaces in general.

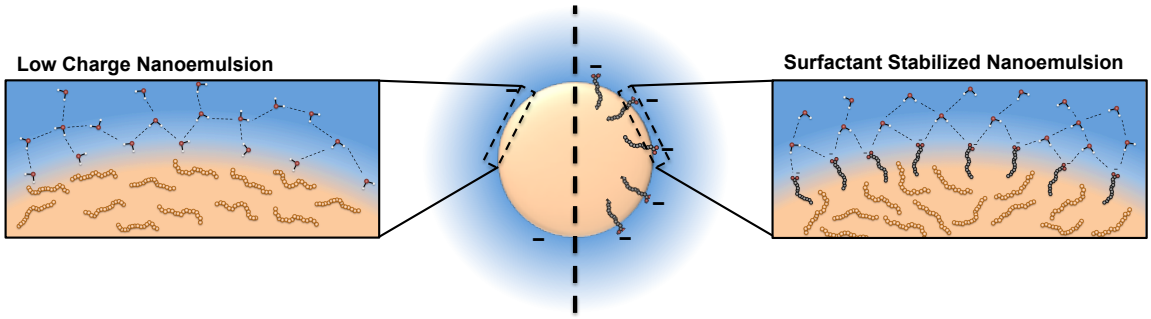

Figure 4.9. Illustration of the bare LCNE surface (left) and the surfactant stabilized nanoemulsion (right).

Along with demonstrating surface-active impurities have been minimized, the free OD also provides intriguing new information about water-oil interactions at the bare nanoemulsion surface. The 15 cm^{-1} frequency shift relative to similar planar oil-water interfaces indicates that oil-water dispersion bonding interactions are stronger at the droplet surface. Additional VSFSS experiments of the hydrophobic phase demonstrate the hexadecane molecules are oriented parallel to the droplet surface and reorganize their alkyl chains as a result of surfactant adsorption (illustrated in Figure 4.9). This appears to be a general phenomenon, as this oil phase reorganization was observed for anionic, cationic, and nonionic surfactants. With the structure and bonding environment of the

interfacial aqueous and hydrophobic molecules characterized in the presence and absence of surfactants, Chapter V will investigate the structural features of surface adsorbed ionic surfactants and the chemical bonding environment around their headgroups.

CHAPTER V

SURFACTANT ADSORPTION TO NANOEMULSION SURFACES

Addition of emulsifiers stabilize nanoemulsions by lowering the surface tension and providing electrostatic or steric repulsive forces that are necessary for long-term nanoemulsion stability.[15, 17, 21] Within this chapter the molecular structure of surfactants are studied at the nanoemulsion surface using VSFSS. The common surfactant, CTAB, is studied at the regular nanoemulsion interface (oil droplets dispersed in water), while the surfactant AOT is used to stabilize both regular and reverse (water droplets dispersed in oil) nanoemulsions. Comparative studies of surfactant adsorption at the nano- oil and water droplet surfaces alongside the extended planar oil-water interface reveal that surfactants assemble in a more disordered configuration at both oil and water droplet surfaces compared to the planar oil-water interface. Additional work with AOT, selectively probing the sulfonate headgroup and water vibrational modes reveal similarities in surfactant headgroup solvation and similar trends in surfactant induced water ordering between planar and curved oil-water interfaces. The AOT VSFSS experiments reported here were performed in collaboration with Dr. Jennifer K. Hensel and are compared to planar surfactant sum-frequency experiments performed by Dr. Regina K. Ciszewski, Dr. Brandon K. Schabes, and Dr. Clive T. Kittredge. This chapter contains some previously published work.[36]

Introduction

While high charged bare nanoemulsions seem to be stabilized by trace surface impurities,[107-108] the stabilization of nanoemulsions by emulsifiers is the most effective way to ensure long term droplet stability. By tuning the chemical composition of these emulsifier mixtures nanoemulsions can be purposed towards applications such as cosmetic,[3] pharmaceutical,[4-8] oil-recovery,[12-13] and material synthesis.[19-20] Altering the composition of these surface layers can result in changes to the nanoemulsions stability, charge, and surface rheological properties.[8, 21] However, the structure of these interfacial layers at the nanoemulsion surface is hard to probe with a molecular specificity seen in studies of other surfactant aggregates, such as microemulsions and micelles. The small sizes of those colloidal systems are well suited for traditional vibrational spectroscopic techniques, such as infrared and Raman spectroscopies, where an interfacial specificity isn't necessary.[50-51, 54, 169-170] These techniques have allowed researchers to understand the impact molecular scale surfactant structure has on the larger surfactant aggregate/microemulsion droplet structure. Unfortunately, those techniques are unable to distinguish between surface and bulk molecules in nanoemulsion samples due to the larger droplet size. Thus, the advent of VSFSS has opened the door to studying the molecular structure of surfactants at the larger nanoemulsion droplet surfaces.

The early nanoemulsion studies using VSFSS focused on nanoemulsions stabilized by simple linear alkyl chain surfactants. They found that the surfactant molecules form a significantly conformationally disordered monolayer at the nanoemulsion droplet surface, with the surfactant alkyl chains possessing a significant

amount of gauche defects even at bulk concentrations near the surfactant's CMC.[35, 72] This is in contrast to the extended planar oil-water interface where the surfactants are found to form conformationally ordered monolayers, with relatively few gauche defects, as the bulk surfactant concentration approaches its CMC value.[65, 171-173] As surfactants pack together at the planar oil-water interface it \ has been observed that linear alkyl chains become more conformationally rigid (i.e. less gauche defects along the alkyl chain) as the average area/molecule is lowered.[171] Thus, the early vibrational sum-frequency scattering spectroscopy (VSFSS) experiments would seemingly suggest that the surfactant interfacial density is lower at the nanoemulsion surface compared to similar planar oil-water interfaces. This was, in fact, concluded for sodium dodecyl sulfate (SDS) stabilized nanoemulsions, where the Roke lab found an maximum surface density of > 4 nm^2/ SDS molecule,[76, 174] compared to the ~0.5 nm^2/ molecule found at the planar oil-water interface.[33, 44, 173]

It is speculated the differences in alkyl chain ordering could be the manifestation of a non-equilibrium state.[35] Since energy is required to form nanoemulsions,[17, 21] it is possible that surfactant assembly at a non-equilibrium interface is going to be inherently different compared to the thermodynamically stable planar oil-water interface. Typical time scales of surfactant adsorption to a planar oil-water interface range from seconds to minutes,[33, 175-177] whereas rough calculations of nanoemulsion droplet rotational motion would dictate a full droplet rotation in about a quarter to half a second.[35] If the solution surrounding the droplet surface is continuously perturb on timescales quicker than adsorption, it stands to reason the surface is truly in a non-equilibrium state. Additionally, the sonication process that mixes the dispersed phase into the continuous

phase could be playing a role in altering the thermodynamics of emulsifier adsorption and altering the adsorption properties of surfactants. Unfortunately, early studies have been limited in scope and restricted to regular nanoemulsion surfaces, so many of details of surfactant adsorption to nanoemulsion surfaces have yet to be understood.

This chapter investigates surfactant adsorption to the nanoemulsion surface and seeks to understand the conformational arrangement of surfactants at a variety of nanoemulsion oil-water interfaces. Observations of the nanoemulsion interface are directly compared to experiments of surfactant adsorption to the planar oil-water interface. VSFSS was used to retrieve molecularly specific details of surfactants at the nanoemulsion oil-water interface, while reflection geometry VSFS and surface tension were used to understand surfactant adsorption to the planar oil-water interface. For the studies reported here hexadecyltrimethylammonium bromide (CTAB) is studied at the planar oil-water interface as a segue into more advanced experiments utilizing AOT to compare a variety of interfaces. Regular nanoemulsions stabilized by several concentrations of CTAB were measured using VSFSS in the SSP polarization combination. Once CTAB has been characterized and the methods for understanding surfactant assembly illustrated, AOT is used to explore similarities and differences between surfactant stabilized regular and reverse nanoemulsion interfaces, the affect of branching in the hydrophobic phase on the surfactant packing structure, long term stability of the interfacial surfactant layer, and how changes to the counterion affect headgroup solvation and water ordering at the nanoemulsion interface.

For all the studies in this chapter, unless otherwise noted, regular nanoemulsions were prepared at 1% vol./vol. deuterated hexadecane as the dispersed phase and D_2O as

the continuous phase. Reverse nanoemulsions were created by dispersing 1% vol./vol. D_2O into twice distilled CCl_4 with 1 mM AOT dissolved into the hydrophobic continuous phase.

CTAB Stabilized Regular Nanoemulsions

Linear alkyl chain surfactants provide the easiest system for understanding changes to alkyl chain conformation that result from changes to the molecular interfacial packing density. Surfactant conformational behavior can be assessed with vibrational sum-frequency experiments by observing the ratio of vibrational intensities arising from the methylene (CH_2, d) and methyl (CH_3, r) symmetric stretches (illustrated in Figure 5.1).[35, 61, 64, 172, 178] For example, a low d/r ratio ($d/r << 1$) is observed under tight interfacial packing conditions where closely spaced surfactants possess an "upright" and rigid conformational arrangement with few gauche defects along their alkyl chains. Such a conformational arrangement results in significant signal cancelation for the methylene symmetric stretch due to deconstructive interference of oppositely oriented methylene modes. This is concurrent with the increasing common alignment of methyl groups at the end of the surfactant chain resulting in an increased intensity from the methyl symmetric stretches. This is a routine analysis in sum-frequency that has been around since the first studies of aqueous-hydrophobic interfaces[61, 65] and can be readily translated to the scattering form of sum-frequency spectroscopy. While the absolute intensity of various vibrational modes will change as a function of the detection angle,[68-69] analyzing the

relative ratio for these two vibrational modes is still valid as both modes carry the same dependency on the detection angle.[35]

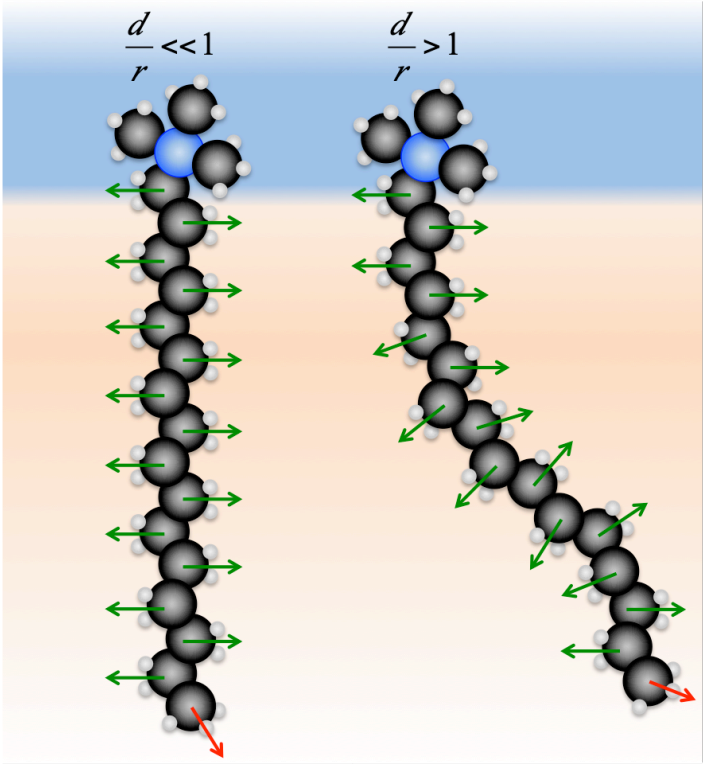

Figure 5.1. Illustration of the dipole ordering along the CTAB alkyl chain, including the methylene dipoles (green) and methyl dipole (red), and the associated d/r ratio.

More work has been done investigating nanoemulsions stabilized by surfactants with 12 carbon long alkyl chains,[35, 72, 76] whereas the surfactant's alkyl chain discussed here matches the length of the oil phase (16 carbons long). CTAB has been previously studied at the planar hexadecane-water interface by Knock et al,[173] and is, thus, a good comparator for the experiments reported here at the hexadecane nanoemulsion-water interface. VSFSS spectra taken in the SSP polarization combination are shown in Figure 5.2 as a function of bulk surfactant concentration. For the VSFSS experimental setup used, the limit of detection for CTAB appears to be near a bulk concentration of 0.1 mM

(green trace). Unfortunately this doesn't provide much of a range of CTAB concentrations to study before reaching the bulk CMC. It is desirable to remain under the CMC to avoid micelle formation that could interfere with the adsorption process and begin to contribute to infrared absorption by the continuous phase. The spectra for CTAB concentrations > 0.1 mM were able to be fit to a series of 5 peaks corresponding to the CH_2 symmetric stretch (2857 cm^{-1}), the CH_3 symmetric stretch (2876 cm^{-1}), the CH_2 asymmetric stretch (2907 cm^{-1}), the CH_3 fermi resonance (2938 cm^{-1}), and a broad resonance at ~2975 cm^{-1} to capture sum-frequency intensity likely arising from poorly resolved headgroup modes.[65, 171, 173, 179]

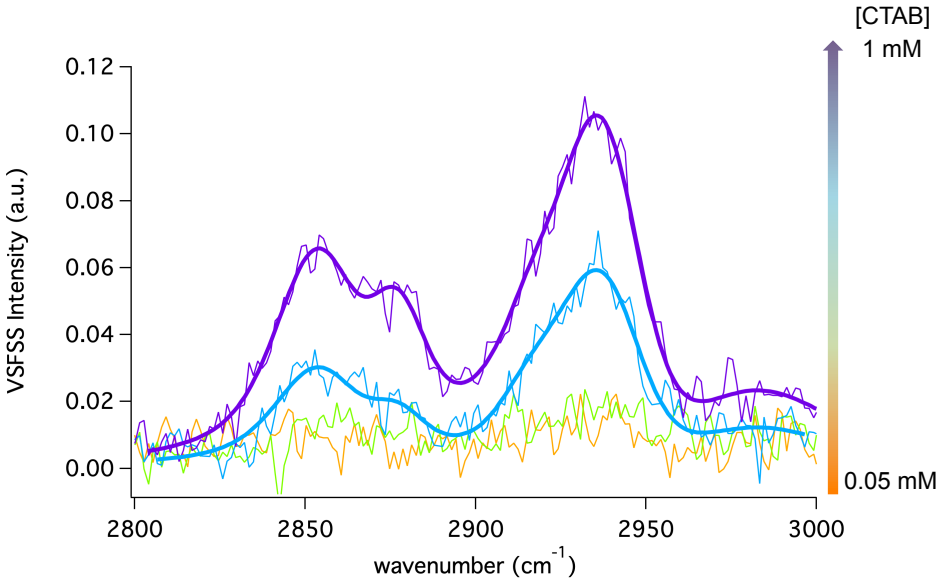

Figure 5.2. VSFSS spectra in the SSP polarization combination of CTAB at 0.05 mM (orange), 0.1 mM (green), 0.5 mM (blue), and 1 mM (purple).

At a CTAB concentration of 0.5 mM (blue trace) the d/r ratio is 1.8. This ratio lowers to 1.4 as the CTAB concentration reaches the CMC (purple trace, 1 mM). At the CMC, this d/r ratio informs us that the CTAB monolayer at the nanoemulsion surface still possesses a significant degree of conformational disorder along its alkyl chain. This is

very different from the sharp conformational transition that Knock et al. found at the planar hexadecane-water interface and the tight molecular packing arrangement occuring at higher surfactant concentrations. At a bulk CTAB concentration of 0.6 mM, the resultant d/r ratio measured at the planar hexadecane-water interface was ~ 0.5. The largest d/r ratio in the same study was ~1.5, which is equal to the lowest value we observe for CTAB at the nanoemulsion interface. It would appear, then, that CTAB possesses a conformational ordering with fewer gauche defects at the planar hexadecane-water interface compared to the nanoemulsion droplet surface where the CTAB monolayer is rather disordered. This conformational disorder is likely the result of a diffuse layer of CTAB at the nanoemulsion surface. This is consistent with what was observed for shorter alkyl chain surfactants at the nanoemulsion surface. In those studies, even near the CMC sodium dodecyl sulfate (SDS) and dodecyltrimethylammonium bromide (DTAB) possessed d/r ratios > 1.[35, 72]

A previous study from the Richmond lab investigated the adsorption of CTAB to the planar CCl_4-D_2O interface in the presence of a co-surfactant (hexanol).[179] This study is valuable, in the present context, both for generalizing CTAB's adsorption behavior to other oil-water interfaces and as a test to ensure the comparative studies we perform with AOT will provide meaningful results. The planar VSFS spectra of CTAB, without any co-surfactants, found a similar trend to that observed by Knock et al. At the CCl_4-D_2O interface the d/r ratio for CTAB converges on a value of 0.7 as the surfactant approaches its maximum surface concentration. This is also much lower than what is observed for CTAB at the nanoemulsion interface. Additionally, similar to the Knock et al. study, the highest calculated d/r ratio for CTAB at the planar CCl_4-D_2O interface is still lower than

the lowest calculated d/r ratio found at the nanoemulsion interface. While the lowest d/r ratio at the planar CCl_4-D_2O interface (0.7) is slightly higher than that what was determined by Knock et al. (0.5), the concentration dependence of the d/r ratio in the "in-house" study is consistent with what one would expect for increased surfactant packing at the oil-water interface. That is, the d/r ratio lowers as the surfactant surface concentration increases indicating a tigher packed surfactant monolayer with fewer gauche defects on average. Further comparison of Knock and Ciszewskis's studies find the surface tension results for CTAB to be largely similar at the two interfaces. Therefore, as long as comparative surface tension results for the planar hexadecane-water and CCl_4-water interfaces don't yield significantly different results, it would seem the use of the CCl_4-D_2O interface for comparative studies of the planar and nanoemulsion interfaces is valid.

AOT Adsorption to the Nanoemulsion and Planar Oil-Water Interfaces

As surfactants adsorb to the regular nanoemulsion interface, they seem to form more diffuse monolayers than what would be expected from planar oil-water studies. Yet, how this behavior tracks to the reverse nanoemulsion surface or changes upon a branching of the oil phase has not been explored. AOT provides a unique system for understanding the similarities and differences of surfactant adsorption at both regular and reverse nanoemulsions due to its ability to stabilize both systems. This ability to stabilize both regular and reverse nanoemulsions comes from (1) AOT's ability to solubilize in both aqueous and hydrophobic continuous phases, a requirement for initial droplet stabilization,[180] and (2) the wedge-like structure of its branched alkyl chains.[181] The

wedge-shape of it's alkyl chains has been implicated as the reason AOT is able to form a myriad of structurally different bulk surfactant aggregates and is likely the reason that it does not require a co-surfactant for reverse nanoemulsion stabilization.[182]

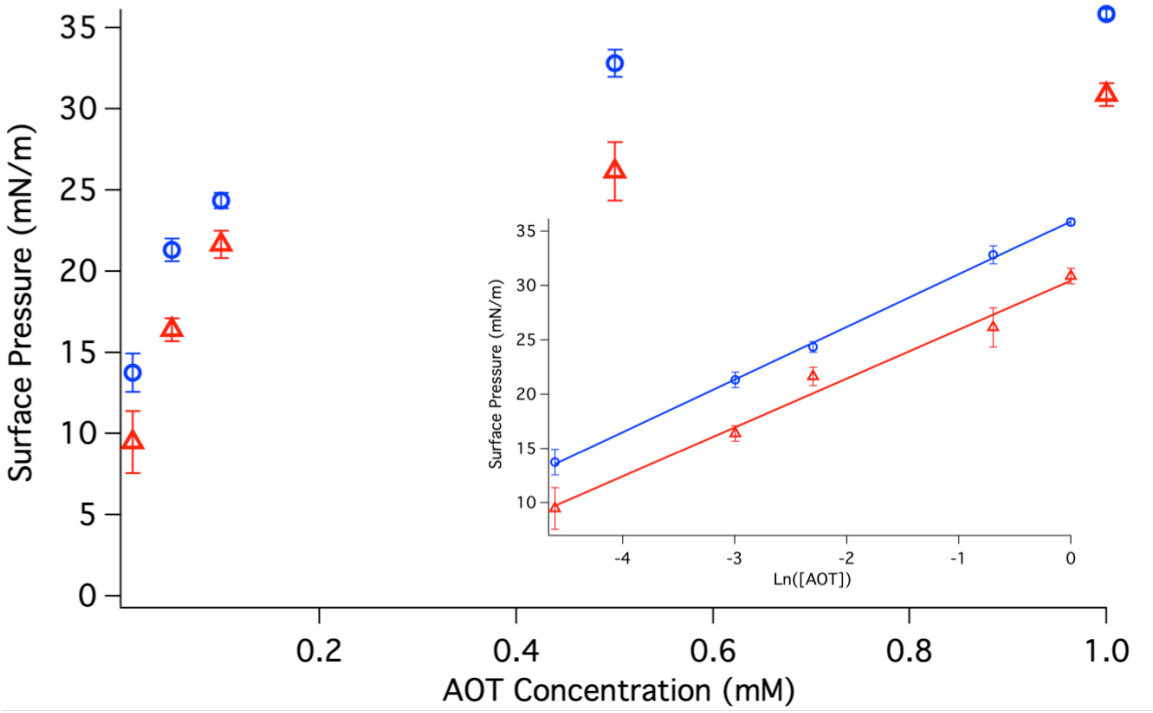

Figure 5.3. Surface pressure measurements of AOT adsorbed to the hexadecane-H_2O (red) and CCl_4-H_2O (blue) interfaces. Inset is the surface pressure plotted against the natural log of the AOT concentration.

Interfacial pressure measurements of AOT at the hexadecane-H_2O and CCl_4-H_2O (Figure 5.3) interfaces provide a means of estimating the bulk surfactant concentration necessary to achieve full droplet surface coverage. Measuring the oil-water interfacial pressure for AOT aqueous solutions, with bulk concentrations ranging from 0.01 to 1 mM, indicates the surface concentration of AOT increases with increasing bulk concentration. Plotting the surface pressure versus $ln([AOT])$ linearizes the surface pressure trend (inset, Figure 5.3). Using the Gibbs adsorption isotherm (equation 5.1), the interfacial pressure can be correlated with the bulk surfactant concentration to

determine the maximum surface excess (Γ) and, from that, the equilibrium surface area per headgroup.[33]

$$\Gamma = \frac{-1}{n_i RT}\left(\frac{\partial \pi}{\partial log(C_i)}\right)_T$$

(5.1)

For the analysis presented here, n_i = 2 in order to account for AOT's counterion species, R is the ideal gas constant, and the room temperature (T) was measured to be 295 K. Fitting the linearized surface pressure plots with equation 5.1 calculates a maximum surface excess of 1.3(±0.1) x 10^{-10} mol/cm^2 at the CCl_4-H_2O interface and 1.5(±0.1) x 10^{-10} mol/cm^2 at the hexadecane-H_2O interface. This converts into an average surface area per AOT molecule is found to be 131 (± 20) and 151 (± 23) Å^2 for the CCl_4-H_2O and hexadecane-H_2O interfaces, respectively. These values are comparable to the area per headgroup of AOT at the planar air-water interface calculated from neutron reflectivity experiments.[45, 183] Using these calculated headgroup areas, the minimum bulk concentration necessary to saturate a nanoemulsion with a 200 nm diameter was estimated using equation 5.2.

$$C_{AOT} = \frac{3\rho\phi}{rN_A}$$

(5.2)

The estimated bulk concentration of AOT (C_{AOT}) for full surface coverage is dependent on the surfactant density (ρ), the droplet volume fraction (ϕ), the droplet radius (r) and Avogadro's number (N_A). Using this expression it is estimated that bulk AOT concentrations of 0.3 and 0.4 mM are necessary to fully cover 1% vol./vol. solutions of 200 nm regular (hexadecane-H_2O) and reverse (CCl_4-H_2O) nanoemulsions, respectively.

VSFSS, in the SSP polarization combination, was used to measure nanoemulsions dispersed in a solution of 1 mM AOT, while VSFS was used to measure the spectral response of AOT (1 mM) at the planar CCl_4-H_2O interface. Figure 5.4a-c displays the typical response measured at the regular, reverse, and planar oil-water interfaces. The nanoemulsion VSFSS spectra (Figure 5.4a-b) were fit to a series of four known CH vibrational modes corresponding to the CH_2 symmetric stretch (2856 cm^{-1}), CH_3 symmetric stretch (2872 cm^{-1}), the CH symmetric stretch (2905 cm^{-1}), and the CH_3 fermi resonance splitting of the CH_3 symmetric stretch and bending overtone (2933 cm^{-1}).[98, 171, 184] The CH_2 symmetric stretch is particularly broad in these fits, which is justified by as intensity arising from numerous different CH_2 moieties occupying different chemical environments and orientations at various parts of the AOT molecule (green circles, Figure 5.4d).

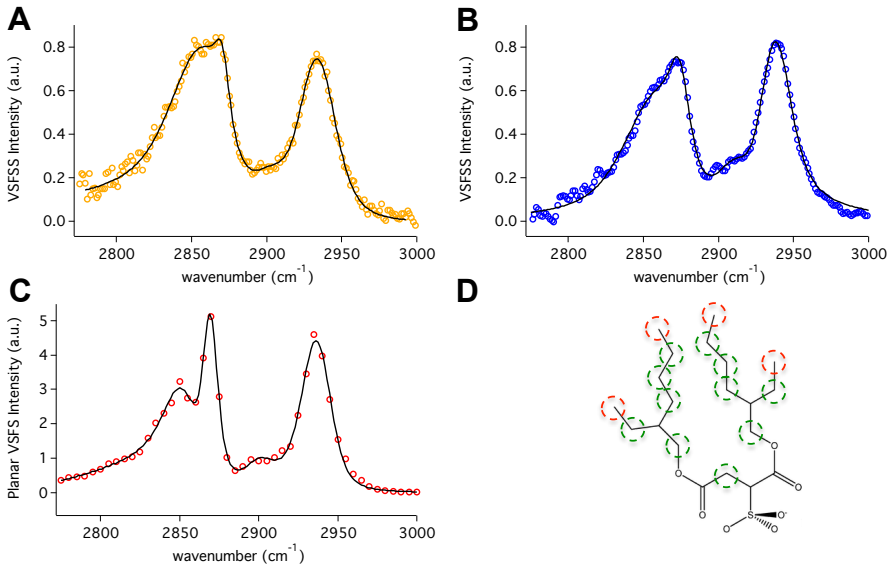

Figure 5.4. Sum-frequency spectra, taken in the SSP polarization combination, of 1 mM AOT at the (A) regular nanoemulsion, (B) reverse nanoemulsion, and (C) planar CCl_4-H_2O interfaces. (D) The methylene (green) and methyl (red) moieties along the alkyl chains contributing to these spectra are highlighted.

The planar VSFS spectrum (Figure 5.4c) is fit to the same CH_2 symmetric stretch (2856 cm^{-1}), CH_3 symmetric stretch (2869 cm^{-1}), the CH symmetric stretch (2908 cm^{-1}), and the CH_3 fermi resonance splitting of the CH_3 symmetric stretch and bending overtone (2932 cm^{-1}). The higher resolution found in the picosecond planar VSFS experiment, compared to the scattering experiments, is partially responsible for the sharper spectral features seen in the planar spectrum. Given the higher resolution, the appearance of a broad CH_2 resonance in the planar sum-frequency spectrum is taken as further justification for the broad CH_2 resonance found in the nanoemulsion spectra.

While there are similarities in frequencies and breadth of the assigned peaks between the planar and droplet spectra, the relative intensities for the methylene and methyl vibrational modes is significantly different between the nanoemulsion and planar interfaces. For the regular and reverse nanoemulsion droplet surfaces, the d/r ratio was calculated to be 2.8 ± 0.4 and 2.4 ± 0.3, respectively. While the diversity of methylene groups found on the primary and side chains, and near the headgroup, restrict our interpretation from determining whether the AOT chains are in a strict trans conformation or possess some degree of gauche defects; the ratio between the methylene and methyl response can still provide a valuable metric for comparing conformational order across interfaces. Thus, we can conclude, that AOT molecules adopt a similar conformational arrangement at both regular and reverse nanoemulsion interfaces given the similarity in the d/r ratio found in the two systems.

Turning attention to the planar oil-water interface the d/r ratio is determined to be 0.6 ± 0.1. This was originally reported at a slightly higher value,[36] however after averaging more data sets together the average value for the d/r ratio was found to be

lower. This does not affect the original interpretation, but actually emphasizes it and we discuss it here. This lowered d/r ratio is a result of increased relative methyl intensity in the planar spectrum. An increase in order at the planar oil-water interface would be consistent with the ordered lamellar layers that have been studied previously at planar solid-water and air-water interfaces.[182] The conformationally disordered surfactant monolayers at the nanoemulsion interface compared to the planar oil-water interface is also consistent with what was seen for CTAB in the previous section and other observations of disordered surfactant monolayers found in literature.[35, 72, 76] However, it is significant that this behavior is observed for nanoemulsions regardless of whether the oil or the aqueous phase is confined.

To test whether differences in surface concentration between the two systems could be contributing to the observed differences in the d/r ratio, planar VSFS spectra were taken at a series of AOT concentrations ranging 0.01 mM to 2 mM (~ CMC). Interestingly, while the overall intensity increases, the spectral shape of AOT in these spectra (Figure 5.5a) is found to be unchanged as the bulk concentration increases. The calculated d/r ratio (Figure 5.5b) for all concentrations is shown to be largely invariant to concentration. From these experiments it is concluded that the steric hindrance caused by the branched alkyl chains of AOT don't allow the tight packing arrangement or the transition into a more trans conformational arrangement at the planar oil-water interface, as is seen for common linear alkyl chain surfactants. Similar experiments were performed across a more limited concentration range of AOT at the regular nanoemulsion interface, and the spectral shape was also observed to be invariant of the surface concentration.

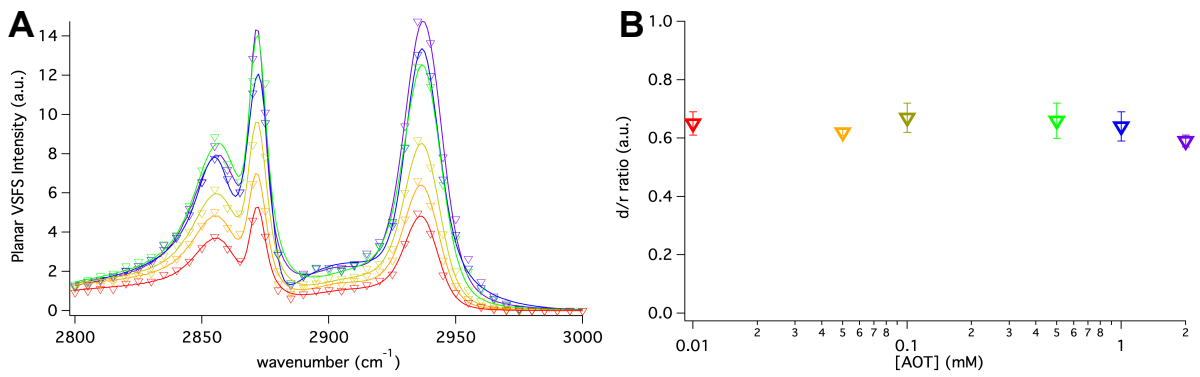

Figure 5.5. (A) Planar sum-frequency spectra, taken in the SSP polarization, of AOT at the CCl_4-H_2O interface and (B) the associated d/r ratio within those spectra for AOT concentrations of 0.01 mM (red), 0.05 mM (orange), 0.1 mM (yellow), 0.5 mM (green), 1.0 mM (blue), and 2 mM (purple).

Further tests were performed to see if spectral differences could arise from changes to the hydrophobic phase. Regular nanoemulsions (1 % vol./vol.) were made using deuterated isooctane to test if a more branched alkyl chain oil phase would alter the average AOT conformational arrangement. Results from VSFSS results are shown in Figure 5.6. The maximum intensity in these spectra were normalized to be comparable, so comparisons of absolute intensity aren't made here. However, it is observed that the spectral shape is remarkably similar; indicating the average AOT conformation at the two droplet surfaces is largely unchanged. It would therefore seem differences in AOT assembly to the nanoemulsion droplet surface and the planar oil-water interface can't be attributed to differences in concentration or oil phase, and is likely the result of the nanoemulsion surface being a non-equilibrium interfacial environment.

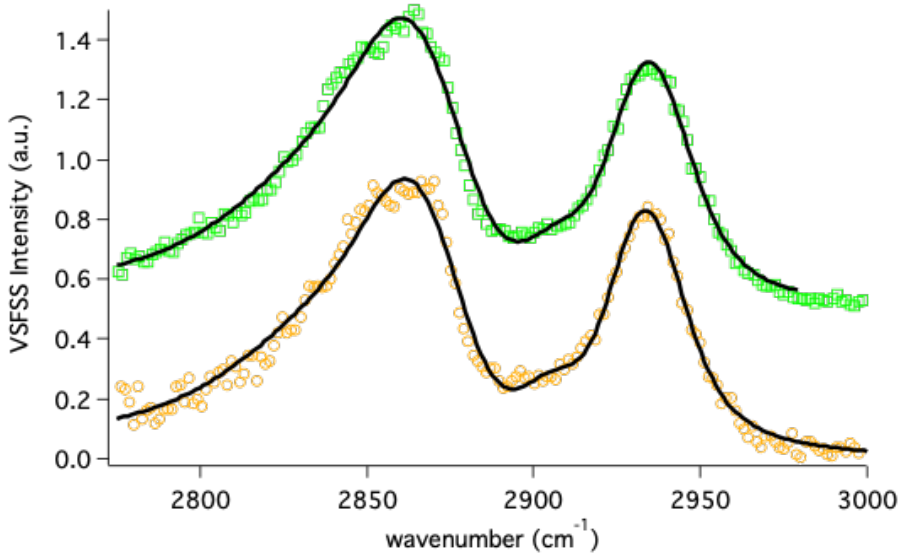

Figure 5.6. VSFSS spectra of 1 mM AOT at the surface of hexadecane (orange) and isooctane (green, vertically offset) regular nanoemulsions.

Structural Stability of AOT Monolayers at Nanoemulsion Interfaces

If the nanoemulsion interface truly is a manifestation of a non-equilibrium state, as has been suggested, then it would be desirable to understand if the structure of the interfacial surfactant monolayer evolves on both short term and long term timescales. Two sets of studies were performed in order to assess the short-term and long-term stability of the AOT monolayer at the nanoemulsion surface. The first set of experiments used VSFSS to monitor the interfacial structure of AOT at the reverse nanoemulsion surface as the nanoemulsions grew via an Ostwald ripening mechanism. The second set of experiments took advantage of several regular nanoemulsion samples found in 2019 that were dated 2013 and 2014. VSFSS was used to measure the AOT at these nanoemulsion surfaces.

Results from VSFSS experiments on the reverse nanoemulsions are found in Figure 5.7. Over the course of 4 days, the average nanoemulsion diameters grew from 200 nm to 643 nm. Ostwald ripening growth mechanisms are linearly proportional to growth in the average droplet volume, with the rate of growth determined to be 360 ± 20 nm^3/s for these samples. Across the 4 days, the spectral shape is found to be invariant of the size. This would indicate that, over this size range, the molecular structure of AOT molecules is unchanged with a growth in droplet size. During growth, as the confined water molecules transit the interface, they don't appear to be any perturbations to the interfacial surfactant layer on the time scale of these experiments (20 min / scan). As with the studies discuss in the last section, there would appear to be an optimum geometry for the AOT alkyl chains and these results would seem to indicate the AOT alkyl conformations is invariant to changes in the surface curvature changes over the measured size range.

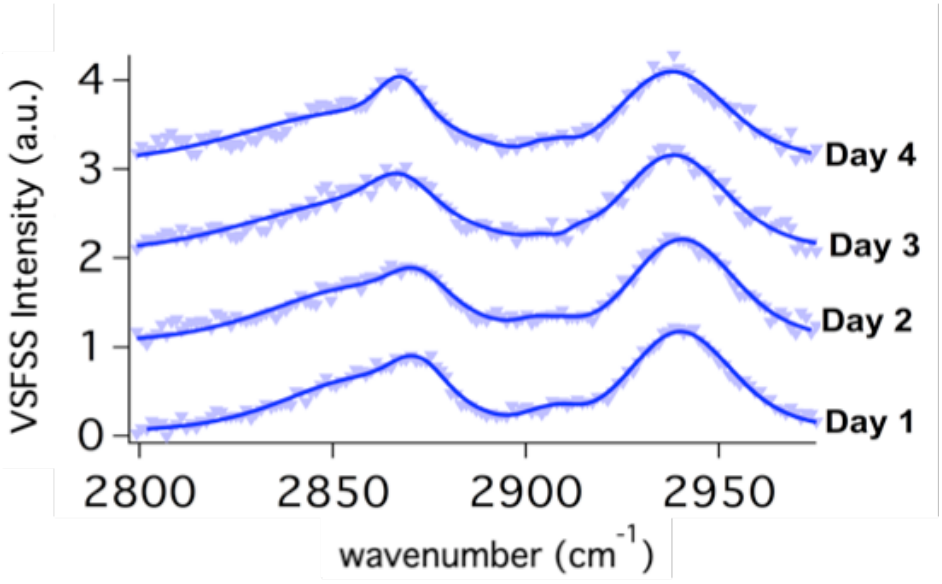

Figure 5.7 Typical trace of VSFSS spectra of reverse nanoemulsion stabilized by 1 mM AOT. Samples were prepared on day 1 and then measured each day for 4 days. Days have been vertically offset from one another.

Whereas reverse nanoemulsions destabilize over the course of days due to the solubility of the dispersed phase in the continuous phase (i.e. Ostwald ripening), AOT stabilized regular hexadecane nanoemulsions are stable for years. For the two samples found in 2019, which were created in 2013 and 2014, their average droplet size changed less than 10%. However, despite the dispersed nanoemulsions having similar droplet sizes, the volume fraction is likely not the same as it originally was. This is suspected because of the appearance of a light oil sheen at the top of the solution. Nevertheless, these two samples provided an excellent opportunity to observe the stabilizing AOT monolayer 5-6 years after formation. The spectra (Figure 5.8) reveal remarkable similarities in the spectral shapes despite some of the samples having aged for several years. Due to suspected changes to volume fraction potentially affecting the absolute intensity,[174] the sum-frequency intensity differences are ignored and spectra normalized to have similar heights. Lack of differences between a fresh sample and the aged samples are concluded to indicate the conformational arrangement of AOT at the nanoemulsion interface is the same.

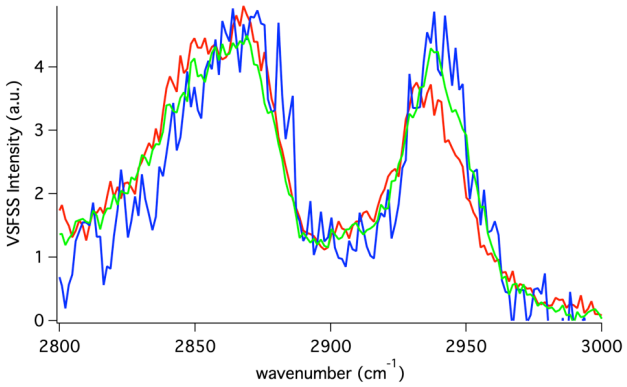

Figure 5.8. VSFSS spectra of AOT stabilized regular nanoemulsions prepared in the year 2013 (blue), 2014 (green), and 2019 (red). Samples measured on the same day in November 2019.

It would seem that the conformational arrangement of AOT alkyl tails at the nanoemulsion interface, while different from the planar oil-water interface, is stable across a range of droplet sizes and time scales. If the structural difference between droplet and planar interfaces is purely due to interfacial curvature, than one would expect a "crossover point" as emulsion sizes grow. Where that crossover point lies remains unknown. In late 2019 micron size emulsions were measured using VSFSS for the first time.[185] Unfortunately, that study doesn't yield any clues as to an estimate of where this potential "crossover" point would be. Most likely, the root cause of differences is the fact that the nanoemulsion surface constitutes a metastable state compared to the equilibrium planar interface. If the molecular level structural differences are due to the Brownian motion of nanoemulsion droplets and continual perturbations to the continuous phase at the droplet surface, as has been suggest,[35] than one would imagine carefully designed temperature dependent studies could yield valuable insight. Potential freezing, or slowing, of the droplet Brownian motion would minimize the affects of the perturbations to the interfacial continuous phase. Temperature dependent VSFSS experiments have been demonstrated,[75, 167, 186] so these studies can be readily performed. However, significant thought will also have to be given to designing the appropriate comparative experiments at the planar interface.

Counterion Effects on Headgroup Solvation and Interfacial Water

With the assembly of AOT alkyl chains is so different at the nanoemulsion surface compared to the planar interface, it is desirable to characterize the headgroup

solvation and the affects of the headgroup on interfacial water structure. This would allow for the development of a more comprehensive picture of how the whole surfactant molecule is positioned at the droplet surface. In order to assess headgroup solvation and water structuring, AOT's sodium counterion was exchanged with potassium and magnesium to form sodium AOT (Na:AOT), potassium AOT (K:AOT), and magnesium AOT (Mg:AOT). Previous work using Raman and Infrared spectroscopies have elucidated how the headgroup vibrational mode is sensitive to changes in counterion interactions and solvation.[50, 170] Potassium and magnesium were chosen here to provide a "spectrum" of headgroup-counterion interactions, with magnesium binding much more strongly to the sulfonate headgroup than either of the others. Further, the degree of water association has also been characterized via Karl-Fischer titration, with the ratio of water molecules/counterion found to be 0.002, 0.6, and 2.7 for Na^+, K^+, and Mg^{2+}, respectively.[187]

The counterion exchange in these studies was performed using previously published methods.[187-188] ^{1}H NMR was used to verify the surfactant was intact after these exchanges and ^{23}Na NMR was used to verify that the original Na^+ counterion had indeed been exchanged. For all K:AOT and Mg:AOT samples the ^{23}Na NMR signal coming from possible residual Na^+ ions was below the detection limit and the ^{1}H NMR spectra matched a Na:AOT reference sample. These results are taken as verification the ion exchange was successful and the surfactant alkyl chain was degraded altered during the process.

Sum-frequency experiments in the SSP polarization combination were performed on D_2O reverse nanoemulsions stabilized by all three surfactants (Na:AOT, K:AOT, and

Mg:AOT) and at the planar oil-water interface (Figure 5.9). In all experiments strong sum-frequency signal is measured near 1045 cm^{-1}. This peak is assigned to a symmetric sulfonate stretch of a highly hydrated sulfonate group. This would be consistent with previous studies of AOT stabilized reverse micelles and microemulsions where this resonance was measured at 1045 cm^{-1} and 1048 cm^{-1} for infrared and Raman spectroscopy, respectively.[50] The frequency from spectral fitting of the VSFSS and VSFS spectra place the sulfonate peak center at 1045 cm^{-1} and 1048 cm^{-1} for the reverse nanoemulsion and planar interfaces, respectively. Small differences observed in the center frequency are within experimental uncertainty and differences in bandwidth are consistent with differences in laser resolution for the planar and nanoemulsion systems.

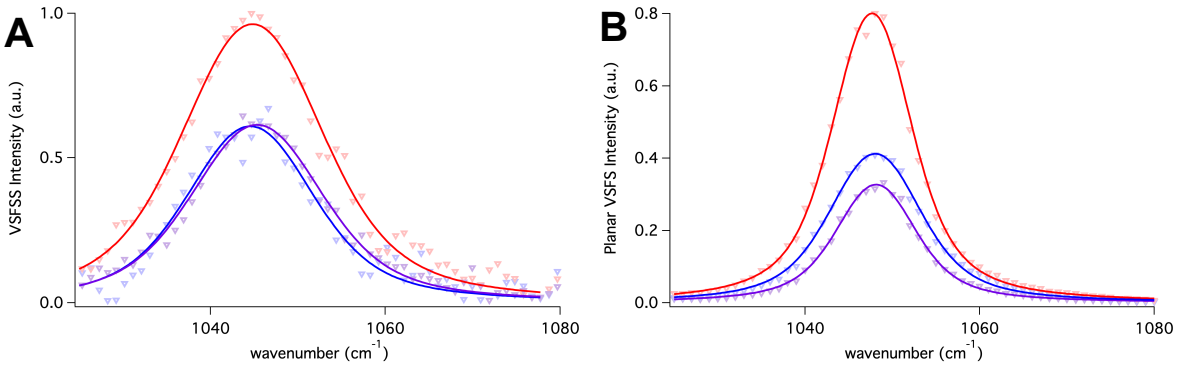

Figure 5.9. Sum-frequency spectra of the sulfonate stretch of Na:AOT (blue), K:AOT (purple), and Mg:AOT (red) at the (A) reverse nanoemulsion surface and (B) the planar oil-water interface.

At both the planar and reverse nanoemulsion interfaces, the center frequency of the sulfonate vibration is within error for all counterions. Raman experiments of solid samples M:AOT (where M is the counterion) showed the sulfonate vibration was sensitive to the intermolecular interactions.[170] The invariance of the sulfonate frequency to counterion indicates the solvation of the headgroup of M:AOT at the reverse

nanoemulsion interface screens the sulfonate stretch from any significant intermolecular interactions with the counterion.[170] Additional similarities are found between the planar and nanoemulsion surfaces in the trend of absolute spectral intensities of across counterions. At both interfaces Mg:AOT has a higher intensity compared to Na:AOT and K:AOT, with the later two possessing relatively similar signal intensities. This increase in intensity could be due to an increase in net orientation of the Mg:AOT sulfonate headgroup or an increase in AOT surface concentration. Looking at the surface tension of Mg:AOT (Figure 5.10) for clues as to the surface activity the different counterion samples finds that the maximum surface excess of Mg:AOT is 1.59 x 10^{-10} mol/cm^2. This approximately a 15% more AOT at the interface for Mg:AOT samples compared to Na:AOT and K:AOT, which have similar maximum surface excesses. This increased surface population is likely a result of the intermolecular charge screening due to the Mg^{2+} counter ion and corresponds well with the observed increase in sum-frequency intensity for Mg:AOT at both the planar and nanoemulsion interfaces. Strikingly, these experiments show that while the assembly of AOT's interfacial chains is sensitive to assembly at the planar versus the curved interface, the solvation of the headgroup is not.

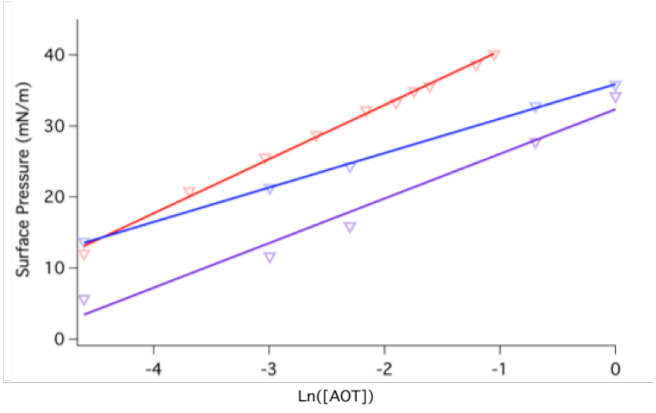

Figure 5.10. Surface pressure of Na:AOT (blue), K:AOT (purple), and Mg:AOT (red), plotted with respect to the natural log of the AOT anion concentration.

Turning back to probe the AOT alkyl chains of the different counterion surfactants, SSP polarization VSFSS experiments of the CH stretching region find similar spectra for each of different counterion surfactants at the D_2O reverse nanoemulsion interface (Figure 5.11a). Negligible differences for the d/r ratio of these samples reveal the counterion identity has no impact on the alkyl chain structure. This is consistent with the picture developed above, as the counterion interacts primarily with the headgroup and despite Mg:AOT having a larger surface population it was found that AOT alkyl chains are unresponsive to changes in surface concentration.

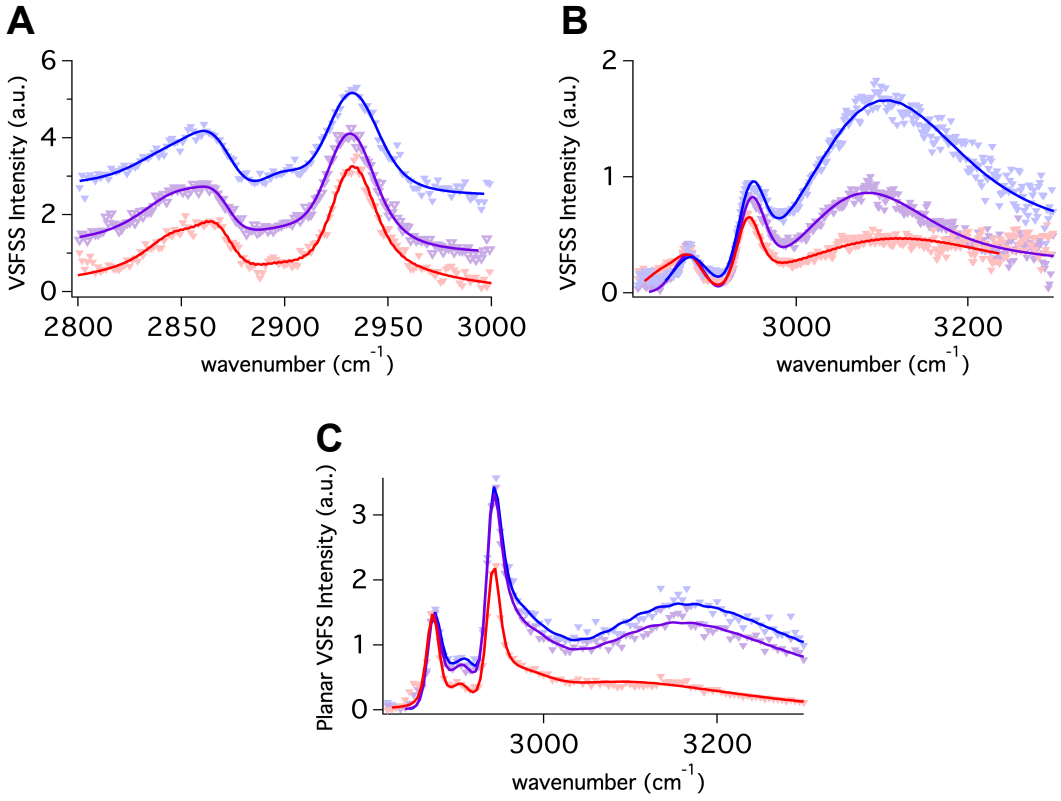

Figure 5.11. Sum-frequency spectra of Na:AOT (blue), K:AOT (purple), and Mg:AOT at the (A) CCl_4–D_2O reverse nanoemulsion interface, (B) CCl_4–H_2O reverse nanoemulsion interface, and the planar CCl_4–H_2O interface. Spectra for at the CCl_4–D_2O reverse nanoemulsion interface have been vertically shifted, but no other spectra have been shifted or scaled.

Swapping the D_2O dispersed phase for H_2O shifts the water vibrational bands back into the frequency region probed by these experiments, allowing for investigations into the affect these different counter ions have on interfacial water and the charge screening process that occurs at the droplet and planar interfaces. The results of SSP polarization VSFSS and VSFS experiments with H_2O as the aqueous phase are presented in Figure 5.11b-c. Sum-frequency intensity appearing from ~3000 to ~3400 cm^{-1} originates from highly coordinated interfacial water molecules. At both interfaces the strongest water is signal is measured for systems with Na:AOT at the oil-water interface, followed by K:AOT, and then Mg:AOT where the spectral response from water is found to be least. After fitting, the CH modes are observed to have similar intensities and frequencies, which is, again, consistent with what was observed above for reverse nanoemulsions made of D_2O and for the planar CCl_4-D_2O interface.

Interfacial water contributions result from the net orientation of water molecules solvating the AOT headgroup and counterion, as well as water molecules aligned by the electric field resulting from charge separation at the interface. Indeed, the majority of the signal observed above 3000 cm^{-1} originates from highly coordinated water that is oriented by the interfacial field created by the AOT charged headgroup as the volume of this region is significantly greater than the volume of water molecules solvating the headgroup. This extended region of ordered water, resulting from the headgroups charge, is going to be most affected by changes to the counterion. At the interface, the surface concentration for the different AOT counterions follows the trend of Mg:AOT > K:AOT ~ Na:AOT, mirroring the relative size of the solvation spheres and the counterion proximity to the surfactant headgroup.[187, 189] However, the intensity of the water

vibrational modes follows a different trend. The highest degree of water orientation is found for the Na^+ ion and is significantly reduced when the Mg^{2+} ion complexes at the surface with AOT. Previous ^1H NMR studies demonstrated the Mg^{2+} counterion is more tightly coordinated with the sulfonate headgroup, followed by K^+ and Na^+.[187] Thus the differences in water intensity at both the planar and droplet interfaces can be accounted for by higher degrees of charge screening by Mg^{2+}, followed by K^+, and then finally Na^+. However, while the extent of charge screening on the enhanced water alignment is affected by the counterion identity, the sulfonate headgroup remains fully solvated for all counterions. Furthermore, this appears to be true for both the curved and the planar interfaces.

Differences in the relative intensity between the CH stretches and coordinated water bands between the nanoemulsion and planar interfacial spectra would seem to suggest there is an additional enhancement of ordered water at the nanoemulsion interface. Similar claims, by others, of enhanced water ordering at nanoemulsion interfaces were mentioned in Chapter IV,[75] but it has been shown those enhanced water modes could be replicated by simply adding surfactant to the bare oil-water interface.[107] Past work from the Richmond lab demonstrated that the coordinated water bands are highly susceptible to slight changes in ionic surfactant concentration at the surface.[105] It is likely that the larger water intensity for the M:AOT systems is reflecting a different AOT surface concentration at the nanoemulsion surface compared to the planar interface under similar experimental conditions. However, the amount of evidence necessary to really elucidate the origins of these relative spectral intensities has yet to be collected. Thus, enhanced water ordering could still possible at the nanodroplet surface, but neither

this work nor the work of others has produced enough evidence to confirm this is the case. It is therefore left as an open question.

Conclusion and Summary

The studies presented in this chapter have provided an expansive and detailed picture of surfactant adsorption to the nanoemulsion surface. Using AOT as a model system, it was found AOT adsorbs to the nanoemulsion interface and forms a conformationally disordered monolayer. While this is consistent with previous work on regular nanoemulsions stabilized simple linear alkyl chain surfactants, this dissertation goes further and demonstrates that this disordered monolayer is similarly structured regardless of whether aqueous or hydrophobic phase is confined. Experiments of AOT adsorption to the surfaces of regular nanoemulsion formed by a branched hydrophobic phase indicate that the conformational arrangement of AOT alkyl chains is largely unaffected and orders itself similarly at nanoemulsion droplets composed of either linear or branched hydrocarbons. It was further found that surfactant molecular structure within this disordered AOT monolayer remains unchanged over droplets ranging 200 nm to 650 nm, and that the molecular structure remains unchanged over course of years.

While the conformational organization of AOT alkyl chains differs between the nanoemulsion and planar interfaces, the headgroup solvation and surfactant-counterion interactions are observed to be similar. VSFSS experiments of the AOT sulfonate headgroup indicate solvent hydration of the ionic headgroup is similar at each interface and any changes to the counterion identity do not result in any measurable changes to the headgroup solvation environment. Counterion identity does, however, play a significant

role in the charge screening of the interfacial electric field at both the curved and planar oil-water interfaces. Measurements of the coordinated water bands reveal that most of water ordering is a result of the interfacial electric field and is dependent upon the counterion-headgroup interactions. As the surfactant-counterion interactions increase and become more closely associated, the electric field is screened and the coordinated water bands shrink as a result of less water ordering. The changes to interfacial water structure induced by counterion charge screening and the invariance of the headgroups solvation are illustrated in Figure 5.12. Chapter VI will continue to explore similar charge screening phenomena, but with a focus on how it impacts surfactant adsorption.

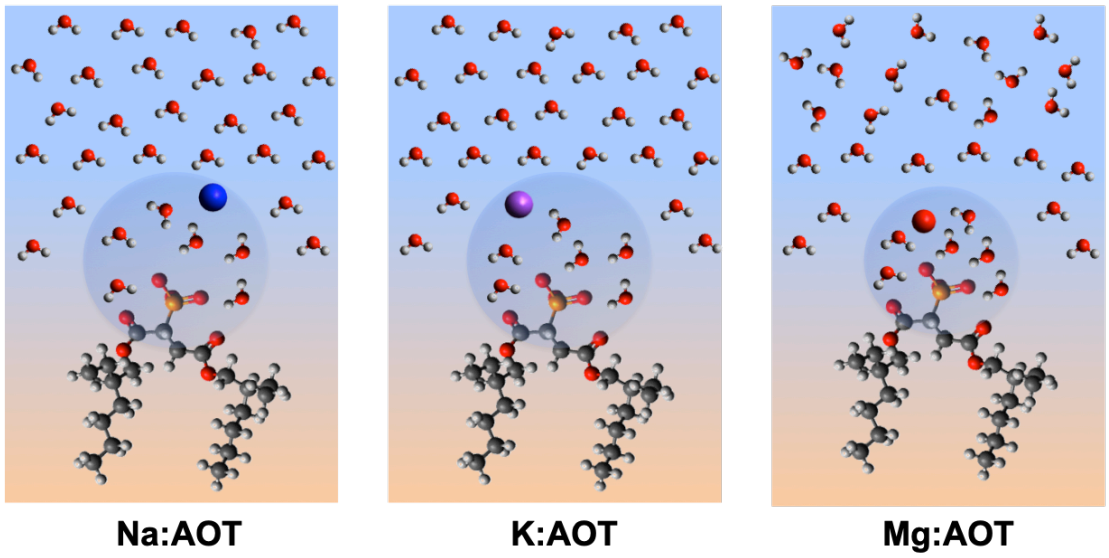

Figure 5.12. Illustration of the effects of counterion charge screening on water structure at the planar and nanoemulsion interface. Image adapted from Hensel et. al.[36]

CHAPTER VI

ELECTROSTATIC CONTRIBUTIONS TO SURFACTANT ADSORPTION AT NANOEMULSION INTERFACES

Electrostatic forces play an important role in the stabilization of nanoemulsion by providing a repulsive force to prevent droplet coagulation. On the molecular level, however, the specific effects that these electrostatic forces have the assembly on surfactant monolayers is not fully understood. This chapter investigates changes to surfactant adsorption behavior at both the planar and nanoemulsion oil-water interfaces as NaCl is used to lower the Debye screening length resulting in a charge screening of the inter-surfactant electrostatic interactions. Surface pressure and VSFSS are used to monitor the adsorption of AOT to these oil-water interfaces and a Langmuir model is applied to quantify and compare the effects of added salt on surfactant adsorption to these two interfaces. These studies observe increased AOT adsorption at both the planar and nanoemulsion oil-water interfaces with a similar dependence on salt concentration. These experiments conclude that screening the repulsive forces between surfactant headgroups induce the same changes to surfactant adsorption, despite the different thermodynamic nature of the planar and curved interfaces. Marc J. Foster contributed to the collection of surface pressure measurements presented here.

Introduction

One of the dominant molecular factors affecting the adsorption behavior of ionic surfactants is the electrostatic repulsive forces between the surfactant headgroups.[33] As ionic surfactants adsorb to the oil-water interface and interfacial potential that establishes an electric double layer in the solution extending out from the interface. The presence of this electric double layer can then influence the subsequent adsorption of other surfactants and polyelectrolytes.[33, 100, 190-191] Within the surfactant monolayer at the oil-water interface, the electrostatic interactions between ionic headgroups will affect the maximum packing density of the surfactant molecules and help dictate the concentrations at when it is thermodynamically favorable to being spontaneously creating of micelles.[33] For nanoemulsions, the development of this interfacial electrostatic potential is additionally important for their stabilization, because nanoemulsion stability requires a repulsive force that will resist droplet coagulation.[21] Derjaguin-Landau-Verwey-Overbeek (DLVO) theory describes this repulsive electrostatic force and has been rather successful at describing colloidal stability for decades.[41, 192]

While the contributions of ionic surfactants to nanoemulsion stability are generally acknowledged due to DLVO theory, the contributions of the electrostatic interactions on the structure of the surfactant monolayer at the droplet surface are not fully understood. At planar aqueous-hydrophobic interfaces, the effects of these electrostatic interactions on surfactant maximum packing density and CMC concentration have been explored by manipulating the ionic character of the solution. Experiments observing surfactant adsorption while swapping the surfactant counterion or adjusting the

ionic strength of the aqueous phase have helped researchers come to understand that shrinking the Debye length lowers the electrostatic repulsive force between surfactants molecules.[193-197] This is ultimately understood to result in a more compressed surfactant monolayer at the planar aqueous interfaces. While this may be the case at the planar interfaces, it has become well established that surfactant assembly to the nanoemulsion surface is not strictly the same as the planar oil-water interface.[35-36, 71, 76] As discussed in Chapter V, VSFSS experiments have shown that surfactant monolayers at nanoemulsion surfaces are at least an order of magnitude less dense than similarly constructed planar oil-water interfaces. It has been proposed that the difference in packing density largely emerges as a result of the increased electrostatic repulsive forces the surfactant experiences due to the electric field lines not being sufficiently screened through the dispersed phase.[76] This is thought to be the case because the Debye screening length through the dispersed phase is thought to be much larger than the droplet radius.

This chapter seeks to explore the effects of charge screening on surfactant adsorption to the nanoemulsion interface. To date some work has been done that has shown SDS nanoemulsions dispersed in 30 mM NaCl have a more densely packed monolayer compared to SDS stabilized nanoemulsions in neat water.[76] However, the emergence of charge screening effects on surfactant adsorption to the nanoemulsion interface has yet to be explored. The experiments reported in this chapter slowly adjust the ionic strength in order to gradually shrink the Debye screening length. As the ionic strength of the aqueous phase is adjusted using NaCl, pendant droplet tensiometry is used to monitor surfactant adsorption to the planar interface and VSFSS is used to monitor surfactant adsorption to the regular nanoemulsion interface. The effects are then

quantified using a simple Langmuir model in order to compare salt induced changes in adsorption behavior between the nanoemulsion and planar oil-water interfaces.

Effects of Salt on Surfactant Adsorption to the Planar Oil-Water Interface

Beginning with the planar oil-water interface, AOT is used as a model surfactant in order to study the effects that variations in bulk ionic strength exerts on surfactant adsorption. The expected effect is that changes in ionic strength will alter the Debye screening length, which will reduce the electrostatic repulsion and allow increased surfactant adsorption to the oil-water interface. Pendant droplet tensiometry (PDT) is the chosen experimental technique to monitor changes in surfactant adsorption to the planar oil-water interface. For these experiments a constant amount of AOT was dissolved in aqueous salt solutions that possessed a variable amount of NaCl, with the experiments reported here focused on lower salt concentrations (1 μM – 50 mM). These solutions were then suspended in a cuvette filled with CCl_4 and the surface tension measured as described in Chapter III.

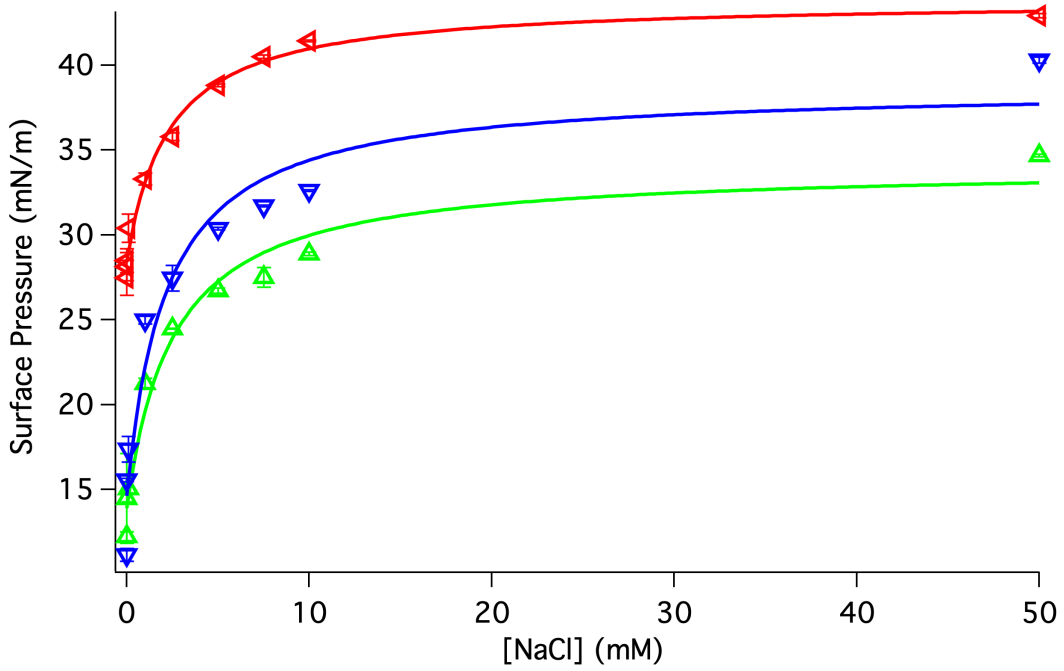

Figure 6.1. Pendant droplet surface pressure results for 0.05 mM (green), 0.1 mM (blue), and 0.5 mM (red) AOT solutions, in the presence of varied background salt concentrations, at the CCl_4–H_2O interface. Solid lines are the respective Langmuir model fits using equation 6.1.

PDT experiments were performed for three AOT concentrations; 0.05 mM, 0.1 mM, and 0.5 mM. A surfactant's CMC is known to change upon the addition salt,[33] so these concentrations were chosen to remain sufficiently far from AOT's CMC both in the absence and presence of salt (2.1 mM).[196] Figure 6.1 displays the results from PDT experiments of three different AOT concentrations in the presence of NaCl. At each AOT concentration, the surface pressure is observed to monotonically increase with increasing NaCl concentrations until it begins to plateau near 50 mM, indicating that the surface concentration of AOT is increasing. Increased surfactant adsorption is consistent with previous studies that have observed increased adsorption for both ionic and non-

ionic surfactants in the presence of salt at the air-water and oil-water interfaces.[193-195, 197-201]

The Langmuir model was chosen to quantitatively describe the change in surface pressure as a function of NaCl concentration. This was done so that additional comparisons can be made later on between the planar and nanoemulsion oil-water interfaces. The model will be briefly introduced here, but is explained in more detail in Appendix C. The Langmuir model describes the oil-water interface as a "lattice" of adsorption sites that are non-interacting and can be either occupied or empty.[202] The final rate equation governing the "reaction" of surfactant adsorption can be expressed in terms of relative surface coverage, where the number of adsorbed surfactants is expressed as a fraction a maximum value. Using surface pressure as a proxy for surfactant population at the oil-water interface and assuming that the number of surfactant molecules at the surface is small in comparison to the number of surfactants in the bulk, the Langmuir model is expressed in the following form (equation 6.1).

$$SP(C) = \frac{A}{1 + \frac{55.5}{Ce^{\frac{-\Delta G}{RT}}}} + SP_0 \tag{6.1}$$

In this form, the surface pressure of a surfactant solution containing some concentration of salt (C) is dependent upon the interfacial pressure of the no-salt surfactant solution (SP_o), an amplitude of change (A), and a change in free energy (ΔG) corresponding to changes in surfactant adsorption. Importantly, the shape of the concentration dependence is only characterized by a single parameter (ΔG) and the other two parameters just

account for the height and baseline of the data. The resulting fit parameters from fitting the various surface pressure traces in Figure 6.1 are presented in Table 6.1.

Table 6.1: Parameters from Langmuir model fits to surface pressure data and experimental SP_o. Error values for the fit parameters are the first standard deviation, while the error for the experimental SP_o is the standard deviation from multiple measurements.

[AOT] (mM)	ΔG (kJ/mol)	A (a.u.)	SP_0 (mN/m)	Exp. SP_0 (mN/m)
0.05	-24.0 ± 0.7	20.2 ± 1.6	13.9 ± 0.9	13.9 ± 0.8
0.1	-24.3 ± 1.0	24.1 ± 2.6	14.6 ± 1.5	10.6 ± 1.2
0.5	-24.2 ± 0.5	15.5 ± 0.8	28.4 ± 0.4	28.9 ± 1.0

The value of SP_o derived from the fits was verified by measuring the surface pressure of AOT at the oil-water interface in the absence of salt. Remarkable agreement is found between the model's SP_o and the experimental SP_o for the 0.05 and 0.5 mM AOT concentrations. At this time, the experimental salt free surface pressure value for 0.1 mM AOT is suspicious as it is lower than the surface pressure value for 0.05 mM. It should be somewhere between the surface pressure values for 0.05 mM and 0.5 mM AOT. As it does not agree with what is known about surfactant adsorption behavior in the absence of salt, this data point is concluded to be an outlier and will have to be retaken when the university reopens after the Covid-19 outbreak.

Use of the Langmuir model assumes a simple adsorption process and no micelle formation. Given the concentrations of NaCl used in these PDT experiments, the lowest CMC value for AOT is ~1.5.[196] Therefore, micelle formation shouldn't be an issue for application of the Langmuir model In fact, there is no evidence of micelle formation in

the surface pressure data either. A sharp break in the surface tension curve is not observed at higher salt concentrations, which one would expect upon reaching the CMC.[33, 196] Similar trends in adsorption behavior were observed in studies of SDS in the presence of a varied NaCl concentration.[193-194] When the SDS concentration was sufficiently low, the CMC was not reached at the highest salt concentrations and the effects of ionic strength on adsorption behavior were observed to be the similar across difference SDS concentrations. At higher concentrations of SDS, where the cmc was reached, the shape of the surface pressure curve distorted. Thus, the consistent ΔG between AOT concentrations is interpreted as the Langmuir model describing the effect of charge screening at the droplet interface without the interference of micelle formation. If the effects of charge screening on surfactant adsorption to the nanoemulsion interface differs from charge screening at the planar oil-water interface, than it should be observable as a variation in the value of ΔG.

Effects of Salt on Surfactant Adsorption to the Regular Nanoemulsion Surface

VSFSS was used to assess changes in surfactant adsorption to the nanoemulsion interface resulting from changes to the ionic strength of the continuous phase. Nanoemulsions were initially prepared by dispersing 2% vol./vol. deuterated hexadecane into a salt-free D_2O continuous phase with a 1 mM AOT concentration. The initial dispersion was diluted into a D_2O salt solution containing NaCl to form a final nanoemulsion sample with 1% vol./vol. dispersed phase, 0.5 mM AOT, and a final NaCl concentration. Similar to the planar PDT studies, the NaCl concentration was varied

between 1 μM to 50 mM. The AOT concentration was chosen in order to have a sufficiently high signal-to-noise ratio at salt-free/low salt concentrations while remaining far enough away from the CMC at high salt concentrations.[196]

VSFSS spectra taken in the SSP polarization combination are shown in Figure 6.2. AOT stabilized nanoemulsions dispersed salt free solutions (black trace, Figure 6.2) provide a baseline spectral response. A monotonic increase in signal intensity that could be the result of increased AOT adsorption is observed upon increasing ionic strength. The square root of the integrated sum-frequency intensity in the CH stretching region (2800 – 3000 cm^{-1}) has been plotted to illustrate the concentration dependent rise in sum-frequency electric field amplitude (inset, Figure 6.2). This also allows for a more thorough analysis of changes to AOT surface concentration, because the electric field is directly proportional to the number of oscillators at the surface.[59, 70, 203-204] The sum-frequency amplitude was normalized for each salt concentration to the amplitude of a salt free nanoemulsion sample. Since the transmission of optical beam lines will change dependent on the beam polarization, this normalization was done in order to provide a polarization combination specific reference that changes in sum-frequency amplitude can be referenced to. This will be important when comparing different polarization combinations later on.

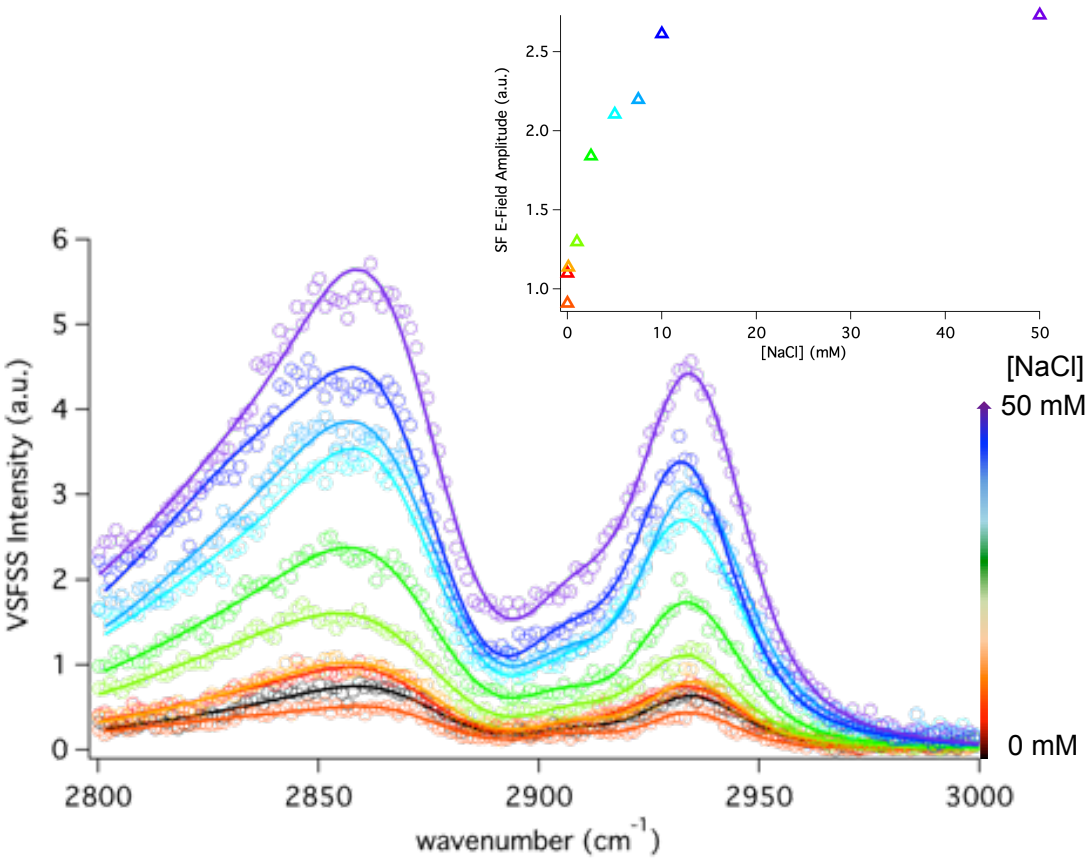

Figure 6.2. VSFSS spectra in the SSP polarization combination of 0.5 mM AOT stabilized nanoemulsions dispersed in various salt solutions. Inset provides the integrated sum-frequency electric field amplitude for each salt solution.

It is important to note that increases in sum-frequency intensity don't just originate from changes in increased AOT surface population, but could also arise from orientational or conformational shifts in the AOT monolayer.[59] Two approaches were taken to assess whether the observed rise in sum-frequency intensity was primarily the result of changes to surface concentration, or whether conformational and orientational changes to the interfacial surfactant structure could be present.

First, while the spectral shapes between spectra don't seem to vary much visually, the AOT spectra were fit to determine this in a more quantitative manner. The same series of peaks used to fit AOT spectra in Chapter V were used to fit these spectra. These

include the CH_2 symmetric stretch (2856 cm^{-1}), CH_3 symmetric stretch (2868 cm^{-1}), the CH symmetric stretch (2908 cm^{-1}), and the CH_3 fermi resonance splitting of the CH_3 symmetric stretch and bending overtone (2932 cm^{-1}). In order to investigate salt induced changes in conformational ordering compared to the salt free sample, the d/r ratio for each salt concentration referenced to the salt free d/r ratio and is plotted as the fraction of the two (salt free d/r ratio / salt d/r ratio, Figure 6.3). This method of displaying the d/r ratios was chosen to illustrate changes from the salt free sample. There is clearly a high degree of uncertainty in these ratios compared to what was observed at the planar oil-water interface when the surfactant concentration was varied (Chapter V). The larger error bars are most likely due to lower spectral resolution in the scattering experiment.[94] Despite the higher error, it is apparent that there is negligible systematic change in the average d/r ratio as the bulk NaCl concentration is varied. This invariance indicates that while the NaCl is causing changes to the AOT monolayer at the regular nanoemulsion surface, evidenced by the large intensity changes, these changes don't involve significant changes in the conformational ordering of AOT molecules. This is consistent with what is known about AOT packing at the planar oil-water interface, where increases in the interfacial concentration fail to induce shifts in the average surfactant conformation. This provides preliminary indications that the change in AOT intensity observed as the solution ionic strength increases is primarily the result of an increasing AOT surface population at the nanoemulsion surface.

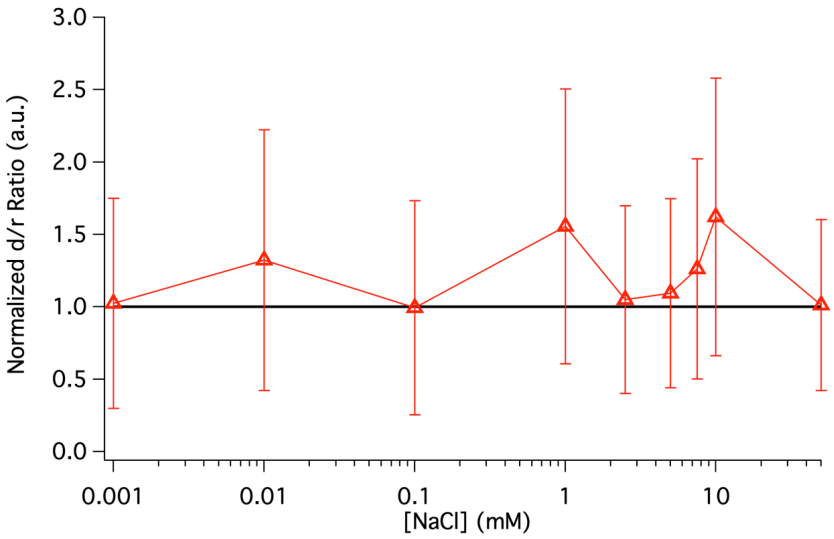

Figure 6.3. Normalized d/r ratios where each salt concentration d/r ratio has been normalized to the salt-free solution. Black line serves as a guide to the eye. Error bars are the propagated errors from the fits.

To support such a conclusion, VSFSS spectra were also taken in the PPP polarization combination (Figure 6.4.). Spectral changes observed in the PPP polarization combination will be more complicated to deconvolve, because several tensor elements contribute to the measured intensity.[84, 86] However, if changes to electric field amplitude scale in a similar manner to that of the SSP polarization combinations, which is dependent upon a single tensor element,[86] then one can reasonably assume that the changes in electric field amplitudes arise primarily from changes in surfactant interfacial concentration and not orientational changes. As with the SSP experiments, AOT stabilized nanoemulsions dispersed in a salt free solution were used to provide a baseline spectral response for the PPP experiments. The sum-frequency amplitude in the CH stretching region is plotted as a function of NaCl concentration for the PPP polarization scheme (inset, Figure 6.4). A concentration dependent rise in the electric field amplitude

is clear and, upon visual inspection, the concentration dependence seems to be similar to what was observed in SSP VSFSS experiments.

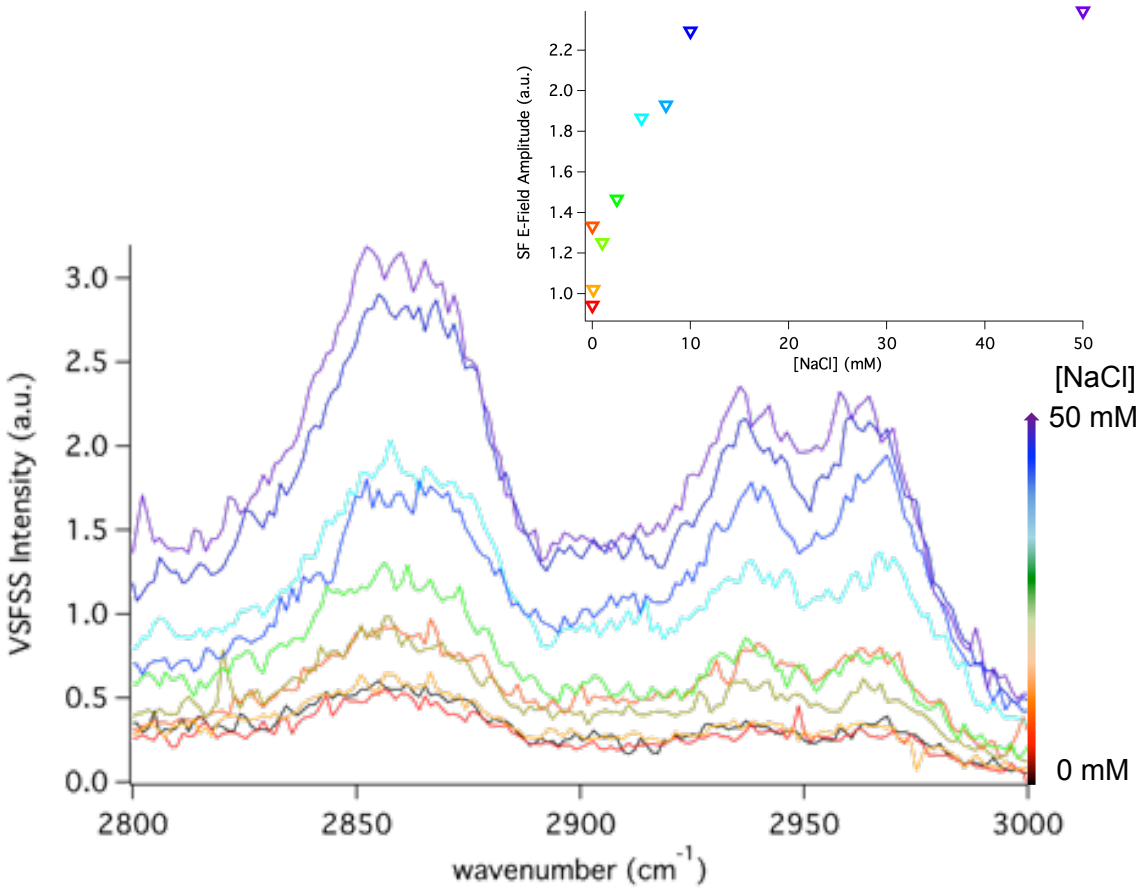

Figure 6.4. VSFSS spectra in the PPP polarization combination of 0.5 mM AOT stabilized nanoemulsions dispersed in various salt solutions. Inset provides the integrated sum-frequency electric field amplitude for each salt solution.

The Langmuir model was used to quantitatively assess similarities in the dependence of SSP and PPP sum-frequency amplitude on salt concentration. While the form expressed in equation 6.1 models changes to surface pressure, the Langmuir model is generalizable to any experiment that monitors adsorption processes that adhere to the model's assumptions.[33, 203-204] It is important, however, that the measured signal can be

reasonably assigned to solely changes in surface concentration of the absorbate and not a surface reorientation. Previous second-order nonlinear scattering experiments used a modified Langmuir model (MLM) to quantitatively describe intensity changes and determine thermodynamic quantities, such as the free energy of adsorption of molecules to the nanodroplet surfaces.[71, 205] The modified Langmuir model assumes the depletion of molecules from the bulk continuous phase to the droplet surface is significant relative to the bulk concentration.[205-206] The available interfacial area for surfactant adsorption is much greater at the droplet surface, compared to the planar, as a result of the increased surface area-to-volume ratio in nanodroplet systems. Given more interfacial area, it is believed a significant portion of the surfactants will adsorb to the surface. This is opposite of what was assumed in the discussion of the use of the Langmuir model to model the salt dependent changes to surface pressure above. However, despite the larger surface area to volume ratio of the nanoemulsion systems, the MLM is not considered appropriate for modeling the changes observed in the VSFSS experiments reported here. This conclusion is rationalized by the fact the addition of salt will not induce the same order of magnitude changes in the number of molecules at the surface versus the bulk,[33, 76, 194] which is what the MLM is primarily used to model.[71, 205-206] Therefore, a Langmuir model was used to model the changes to the sum-frequency electric field amplitude, similar to what was used to model the changes in surface pressure.

The electric field amplitudes for VSFSS experiments performed in the SSP and PPP polarization combinations are presented in Figure 6.5 with the Langmuir model fits included. The functional form of the Langmuir model used for these fits is presented in equation 6.2.

$$E_{SF}(C) = \frac{A}{1 + \frac{55.5}{Ce^{\frac{-\Delta G}{RT}}}} + E_0 \tag{6.2}$$

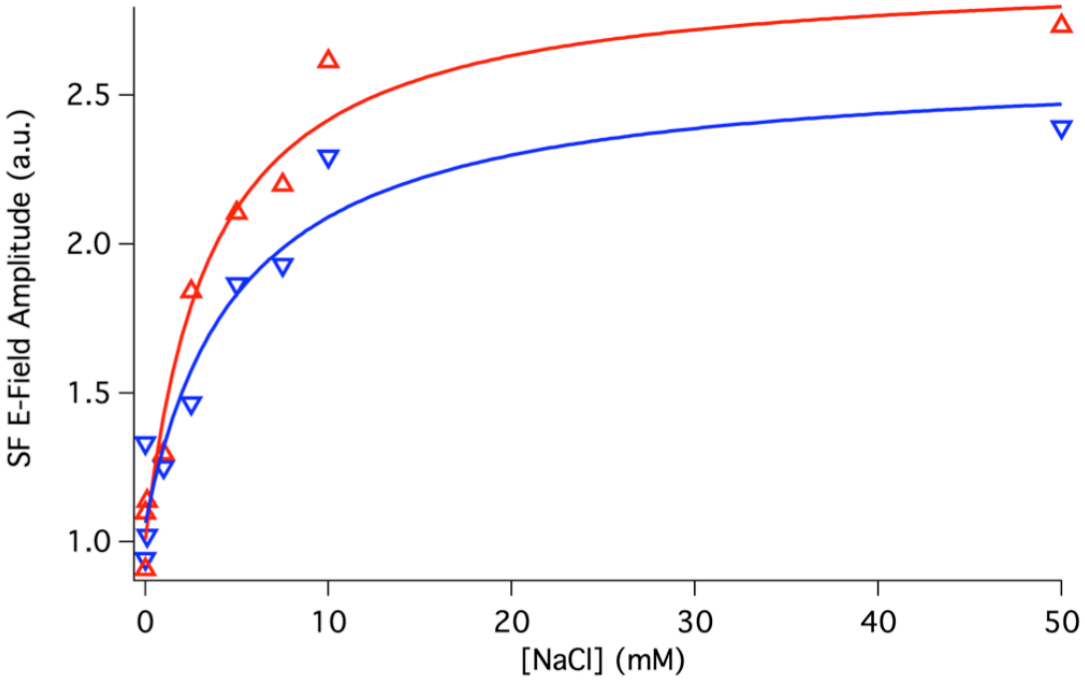

Figure 6.5. Integrated sum-frequency electric field amplitudes of 0.5 mM AOT dispersed in different salt concentrations taken in the SSP (red) and PPP (blue) polarization combinations. Solid lines are the associated Langmuir fits using equation 6.2.

In this form, the integrated sum-frequency electric field amplitude (E_{SF}) at a particular NaCl concentration (C) is a function of the amplitude of change (A), the baseline sum-frequency response (E_0) for a salt free solution, and the free energy change associated with the effects of salt on the surfactant adsorption process (ΔG). Since the electric field amplitudes at each salt concentration have been normalized to the electric field amplitude

for a sample in the absence of salt, E_0 should be 1 for both the SSP and PPP curves. The results of the Langmuir model fits are given in Table 6.2.

Table 6.2: Fit parameters from Langmuir model fits to salt dependent VSFSS experiments performed in the SSP and PPP polarization combinations.

Polarization	ΔG (kJ/mol)	A (a.u.)	E_0 (a.u.)
SSP	-23.1 ± 0.7	1.92 ± 0.15	1.00 ± 0.07
PPP	-22.3 ± 1.1	1.55 ± 0.22	1.06 ± 0.09

Assessing the use of this model, the values of E_0 are within error of 1. This is consistent with the fact that all values have been normalized by the no-salt solution, so the baseline value should be 1. The concentration dependent rise of electric field amplitude, from E_0, also appears to be well characterized, where the steepness of the curve is dependent on the value of ΔG. Similar values of -23.1 ± 0.7 kJ/mol and -22.3 ± 1.1 kJ/mol are found for the SSP and PPP polarization combinations, respectively. However, the amplitude of change from the baseline (A) does appear to be different between the two traces. The relative increase in sum-frequency electric field amplitude from the baseline response (no salt nanoemulsion spectra) is greater in the SSP experiments compared to the PPP experiments. The presence of small orientational changes occurring at the interface could explain this difference in amplitude. Additional polarization combinations, SPS and PSS, would be needed to properly determine specific changes in angular distributions of the CH stretches.[84, 86, 88] However, given the branched nature of the AOT alkyl chains and the lower spectral resolution of these VSFSS

experiments, the appropriate assignments of necessary vibrational modes for this analysis would be difficult.

Despite some of the increase in electric field amplitude likely being the result of small orientational changes, the invariance of the d/r ratio in the SSP polarization combination provides confidence that the majority of the changes in electric field amplitude are the result of increased surfactant adsorption to the regular nanoemulsion surface. As such, the ΔG values for the SSP and PPP experiments are compared to the ΔG value from the PDT experiments with 0.5 mM AOT. Recall from the PDT experiment that ΔG = -24.2 ± 0.5 kJ/mol for the 0.5 mM AOT at the planar oil-water interface. This is close to the values measured for the nanoemulsion experiments. These results would indicate that the effects of charge screening measured at the nanoemulsion droplet surface emerge in the same way as at the extended planar oil-water interface. This is consistent with what was observed in Chapter V when the counterions were changed. VSFSS spectra of the SO mode observed the same increase of Mg:AOT surfactant at the nanoemulsion surface, relative to Na:AOT and K:AOT, that was observed at the planar oil-water interface using VSFS and PDT.

Additional quantification of salt-induced changes to the AOT monolayer can be estimated. A previous VSFSS study monitoring SDS adsorption in the presence of a static salt concentration (30 mM NaCl) determined that the SDS packing density roughly doubled, due to an ~ 4x increase in sum-frequency intensity.[76] Following a similar line of logic, the near 4x increase in the sum-frequency intensity (~2x increase in amplitude) observed in these salt studies would indicate a similar doubling of AOT's surface concentration. An absolute value for AOT's packing density at the nanoemulsion

interface in the absence of salt has yet to be determined, so an absolute area/molecule value can't be given here. While VSFSS studies of linear alkyl surfactants have been able to conclude the packing density of ionic surfactants is ~10x that of the planar interfacial value,[35, 71-72, 76] similar experiments of AOT have yet to produce such a value. The concentration range between the VSFSS detection limit and the CMC for AOT is much narrower than for SDS, making it difficult to observe surfactant adsorption over a wide range of concentrations in order to determine a reliable maximum surface concentration. However, there is reason to believe the AOT monolayer is more diffuse at the nanoemulsion surface compared to the planar oil-water interface since earlier studies of AOT stabilized nanoemulsions found a conformationally disordered monolayer at the nanoemulsion agree,[36] in agreement with the SDS experiments.[35]

Conclusions and Summary

It is becoming increasingly evident that charge screening of electrostatic interactions between surfactants follows a similar trend at the nanoemulsion interface as it does the planar oil-water interface. In Chapter V this was evident in the increased adsorption of Mg:AOT and reduction of water modes upon tighter counterion binding, which were observed at both interfacial geometries. Here in Chapter VI, investigating the adsorption of AOT in the presence of added salt has expanded upon those previous investigations into charge screening at both interfaces. At the planar oil-water interface, PDT measurements were used to monitor AOT adsorption to the planar oil-water interface. These experiments found that decreases to the Debye screen length, due to

increasing ionic strength, resulted in increased AOT adsorption for all concentrations of AOT measured. The concentration dependence of the increasing surface pressure was characterized by a Langmuir model, which demonstrated the effects of added salt on surfactant adsorption had the same concentration dependence for all AOT concentrations.

At the nanoemulsion interface, VSFSS was used to monitor changes in AOT adsorption to the droplet surface. Additions of salt to nanoemulsion solutions resulted in an increase in sum-frequency intensity, indicating increasing surfactant adsorption. Increases in the electric field amplitude observed in both the SSP and PPP polarization combination were characterized by a Langmuir model, which found a similar concentration dependence for the rise in sum-frequency amplitude. This indicates the observed increase in amplitude is primarily the result of increased AOT adsorption to the nanoemulsion surface. Further comparison of the results from all Langmuir models found remarkably similar concentration dependent changes to surfactant adsorption at the planar and nanoemulsion interfaces. This is taken as evidence that reduction of the Debye screening length at the nanoemulsion surface induces the same changes to surfactant adsorption as one would observe at the planar oil-water interface.

Whereas charge-screening trends are the same between the nanoemulsion and planar oil-water interfaces, much more work needs to be done. In particular, the origins of decreased surfactant density at the nanoemulsion interface are of importance. The Roke group has concluded that surfactant-packing density is lower at the nanoemulsion surface because the electric fields that originate from ionic headgroups permeate through the dispersed oil phase.[76] While the slight difference between ΔG values measured between the planar and nanoemulsion interfaces in this dissertation is likely the result of

contributions to the sum-frequency spectra from slight orientational shifts, it is possible that the difference is hinting at additional forces not entirely screened by reducing the Debye screening length in the continuous phase. However, it would be expected that as the charge from headgroups at the regular interface are screened the strength of the electric fields passing through the oil phase should diminish as well.[33, 154] Attempts were made to test the Roke hypothesis by adjusting the ionic strength inside reverse nanoemulsion water droplets. It is not evident, however, that this approach will be successful. The formation of these reverse nanoemulsions requires surfactants are dissolved in the continuous oil phase and the salt is dissolved in the dispersed aqueous phase. Preliminary surface tension results reveal the kinetics of the surfactant adsorption and the equilibrium surface pressure values are very different when the salt and surfactant are in the same phase versus separate into the oil and water phases. Due to these differences, it is therefore unclear at this time whether the reverse nanoemulsion system can be appropriately compared to the regular nanoemulsion system.

The persistent decrease in surfactant density at the nanoemulsion surface, even when the Debye screen length is lowered to about a nanometer, remains an interesting topic for future exploration. While likely the result of the nanoemulsion interface being in a non-equilibrium state, it would be interesting to further explore whether solution conditions can be manufactured where surfactants can adopt a tight pack arrangement at a non-equilibrium surface.

CHAPTER VII

CONCLUSIONS AND FUTURE OUTLOOK

In order to stabilize nanoemulsion dispersions it has been known a reduction of surface tension and addition of electrostatic repulsive forces at the droplet surface are necessary. These stabilizing contributions have most often been provided through the use of mono- and multi-layers of surfactants and polymers that spontaneously adsorb to the droplet surface. Yet, reports about presumably "bare" nanoemulsion surfaces acquiring a significant negative charge that stabilize the droplet would seem to indicate that nano-sized droplets of oil can be effectively mixed into water without any stabilizing additives. The controversy around these bare nanoemulsions has only intensified over the last several decades due to a lack of the knowledge about the molecular structure and composition of nanoemulsion surfaces. Previous experimental approaches to studying nanoemulsion systems have lacked either the chemical or interfacial specificity to inquire about the composition and structure of nanoemulsion droplets. For example, neutron and x-ray scattering have provided structural information about the nanoemulsion interface without a chemical specificity and traditional vibrational spectroscopic techniques have provided chemically specific information without an interfacial specificity. Other methods used to study nanoemulsions can also be binned into categories defined as lacking a chemical or interfacial specificity, or both, without making significant assumptions. The development of vibrational sum-frequency scattering spectroscopy (VSFSS) by Roke and coworkers has provided the much-needed chemical and interfacial

specificity necessary to begin addressing questions on the structure and composition at nanoemulsion interfaces.

The studies reported in this dissertation have used VSFSS to directly probe the bare and surfactant stabilized nanoemulsion interfaces in order to build up a molecular level description of the bare and surfactant-stabilized nanoemulsion surface. This work began in Chapter IV by describing the preparation of bare low charge nanoemulsions (LCNE) that possessed a zeta potential significantly lower than previously reported bare nanoemulsions. VSFSS studies of the aqueous phase in contact with the LCNE surface made the first measurements of unbound water vibrations, otherwise known as the free OD, at the nanoemulsion surface. The presence of the free OD concurrent with the reduced surface charge and pH dependence of the electrophoretic mobility measurements of LCNE droplets provide evidence that the low zeta potential is the result of a minimization of impurities. This, then, would have the implication that the bare nanoemulsions measured to have high zeta potentials in previous studies likely possessed surface-active impurities. With the reduced surface impurities at the LCNE droplet surface, VSFSS measurements found the water-oil bonding interactions were stronger at the nanoemulsion surface relative to a similar planar interface. The structural origins for these stronger bonding interactions remains unknown and will require additional VSFSS experiments in addition to high quality simulations to uncover its origins. On the other side of the interface, the hydrophobic molecules at the bare LCNE surface were concluded to be primarily oriented parallel to the droplet surface. Upon adsorption of ionic and nonionic surfactants the interfacial hexadecane molecules undergo a structural transition at room temperature in response to the surfactant alkyl chains.

With the bare nanoemulsion surface characterized, Chapter V focused on surfactant-stabilized nanoemulsions. These studies made direct comparisons of surfactant structure at the regular and reverse nanoemulsion surfaces as well as the extended planar interface. The surfactant alkyl chains were observed to be adopt a conformationally disordered state, with more gauche defects, at both the nano-oil and nano-water droplet surfaces compared to the planar interface. Yet, while the surfactant alkyl chains were more disordered, surfactant headgroup solvation and charge screening trends of interfacial water molecules were similar at the nanoemulsion and planar oil-water interfaces. Remarkably, these studies suggest that while the alkyl chain conformational arrangement is sensitive to interfacial curvature, surfactant headgroups and their influence on interfacial water are not.

Charge screening of the interfacial headgroups was further explored in Chapter VI, where the Debye screening length was lowered by increasing the solution ionic strength. Pendant droplet tensiometry (PDT) and VSFSS experiments were used to monitor surfactant adsorption to the planar and nanoemulsion oil-water interfaces, respectively. Application of a Langmuir adsorption model to the PDT and VSFSS data reveals that reducing the Debye length results in similar increases of surfactant adsorption to the nanoemulsion and planar oil-water interfaces. The effects of salt on surfactant adsorption, thus, appear to be similar at both interfaces. When considered in totality with the effects of swapping the counterions from Chapter V, it would seem that there are negligible differences in the general effects of charge screening on surfactant adsorption at both nanoemulsion and planar oil-water interfaces.

This dissertation has presented results that provide a deeper understanding of the composition, molecular structure, and bonding environment of both bare and surfactant-stabilized nanoemulsions. In particular, these results have strong implications for the study of bare nanoemulsion systems and the procedures used in their preparation. This dissertation also provides more insight into the assembly of surfactant monolayers at nanoemulsion interfaces and the factors that limit their adsorption.

Future Outlook

The current use of VSFSS is still in its infancy, with the technique only to be found in a limited number of labs worldwide compared to reflection geometry sum-frequency spectroscopy. Professor Roke and coworkers have done phenomenal work in the initial creation, theoretical formulation, and development of VSFSS. At present time, VSFSS has been applied to research involving nanoemulsions, nanoparticles, liposomes, collegen fibers, and cellulose nanocrystals.[36, 70, 207-208] As the number of labs building VSFSS experimental systems grows, so will the diversity of the chemical systems it is used to study. I would like to use the end of this dissertation to briefly share my speculation and perspective on the potential future second-order nonlinear scattering spectroscopies hold. The hope in sharing these is that they will stimulate discussions on where to go next with second-order nonlinear scattering spectroscopies.

First, the use of VSFSS in the study of the air-water interface has not yet been realized; yet the demonstration of VSFSS to probe the surface of ethanol droplets formed by a microjet[209] provides hope that the nano-water droplet surface can be studied. The

most significant technical hurdle currently limiting the use of VSFSS in the study of the air-nano water droplet interface is a method of preparing samples, with droplet radii of 100's nm, which is necessary for reproducible and reliable data to be taken. Once overcome, however, the use of VSFSS would be a significant addition to the toolbox of those studying the surfaces of nano-sized aerosols.

Concurrent with the work reported in this dissertation, several "proof of principal" experiments were performed to explore and highlight the potential of VSFSS. Two of these demonstrations grew out of side projects I worked on during the summers of 2017 and 2018 in collaboration with two extremely talented undergraduate researchers (Oregon REU), Bryce Hickam and Ashley Mapile. Sum-frequency scattering spectra were acquired of nanoemulsions stabilized by surfactant-polyelectrolyte complexes and biodegradable surfactant mixtures, as well as spectra of AOT stabilized foams (Figure 7.1). These were spectra were acquired in a pursuit to explore the potential application of VSFSS to oil remediation efforts, pharmaceutical applications, and the surface structure of foam films. The spectra from those experiments are purely exploratory and several technical challenges are present before reliable VSFSS spectra can be taken. In particular, significant challenges exist with the preparation of foams stable enough for the reliable application of VSFSS. However, the spectra are shared here in the hope that they generate interest in applying VSFSS towards new applications.

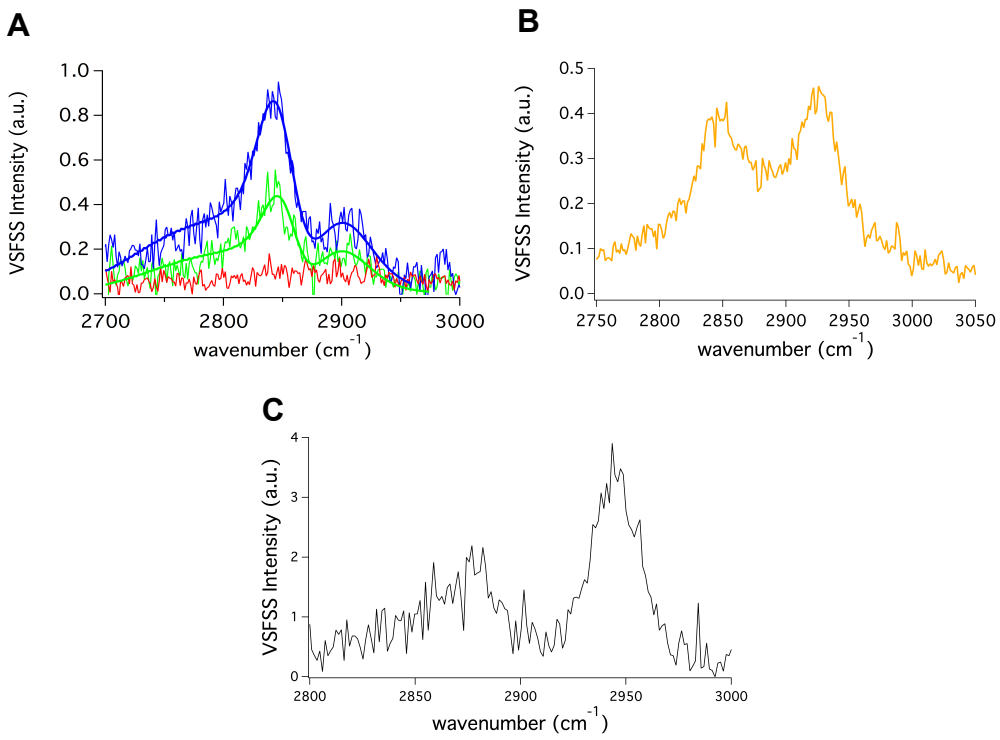

Figure 7.1. VSFSS spectra taken in the SSP polarization combination of nanoemulsions stabilized by (A) different ratios of PSS-deuterated CTAB complexes and (B) lecithin (orange). (C) VSFSS spectrum of AOT stabilized foam.

Finally, the roadmap for future technique development in the area of second-order nonlinear scattering spectroscopies has nearly been written by the history of the field. In the study of planar liquid interfaces, second harmonic generation was realized and then quickly followed by the development of sum-frequency generation. The same pattern occurred with the development of scattering geometry experiments. Second-harmonic scattering (SHS) was first realized by Wang and Eisenthal[210] and was quickly followed by the development of VSFSS.[68] Looking toward the future it is easy to see several developments waiting to be pursued. Electronic sum-frequency scattering spectroscopy (ESFSS) seems to be a logical step in technique development since it, historically, followed the development of vibrational sum-frequency spectroscopy in the study of

planar interfaces. SHS of surface adsorbed chromophores is an example already having been demonstrated where an electronic state is probed at nanoparticle surfaces. It is just that the two excitation laser beams are degenerate in frequency. The development of ESFSS could open new avenues in materials research, such as the study of the electronic transfer at particle interfaces in solution. Another avenue of technique development would include the demonstration of phase-sensitive second-order scattering spectroscopies. The traditional approach to heterodyne detection where the sum-frequency signal is interfered with a local oscillator at the detector, is not possible with scattering experiments as a result of the interference being frustrated by the lack of reproducibility of the sum-frequency path length arising from randomly distributed particles undergoing Brownian motion.[211] However, if the interference can be accomplished at the sample position and phase relationship between incoming beams manipulated appropriately,[212-213] as has been demonstrated with second harmonic generation experiments of planar materials, phase-sensitive scattering experiments may actually be possible in some form.

APPENDIX A

VSFSS AQUEOUS PHASE SPECTRA NORMALIZATION

Normalization of VSFSS spectra was typically accomplished by generating a non-resonant sum-frequency response out of a nonlinear crystal placed at the sample position, using the beams that were used for sample measurements, and the resulting non-resonant spectrum is then used for normalization. These non-resonant spectra correct for the differences in infrared excitation energy across the spectrally broad infrared pulse profile and were collected daily. This was found to be sufficient for the CH and SO stretching regions, where using isotopic dilution mitigates any absorbance by the continuous and dispersed phases. It is not sufficient, however for VSFSS experiments using HOD as the continuous phase, because the same water modes that are being measured at the droplet surface are also absorbing the infrared energy as the pulse passes through the continuous phase.

In order to correct for the frequency dependent absorbance of the infrared pulse, an infrared absorbance spectrum was measured for the 50:50 H_2O:D_2O aqueous phase. This aqueous phase was pressed between two CaF_2 window and the absorbance spectrum was acquired using an FTIR spectrometer (ThermoFisher Scientific). Figure A.1 shows both a typical non-resonant sum-frequency response and the transmission spectrum of the aqueous phase. All VSFSS spectra of the interfacial aqueous phase were normalized to both the daily non-resonant profile and infrared transmission.

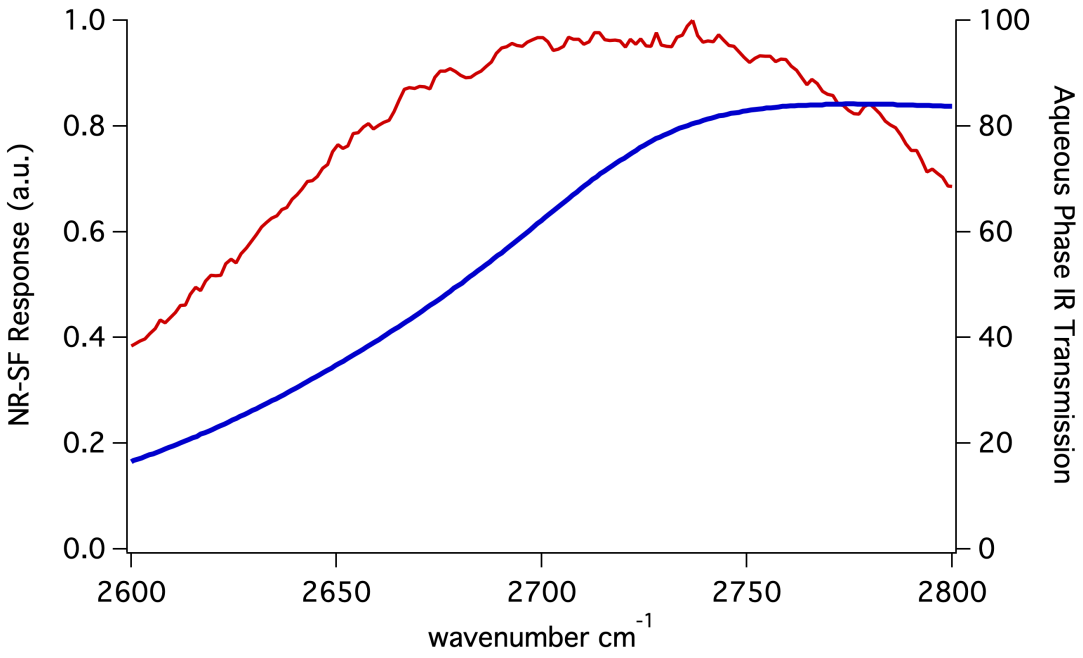

Figure A.4. A typical non-resonant sum-frequency profile (red, left axis) and the infrared transmission spectrum for the 50:50 H_2O:D_2O aqueous phase (blue, right axis).

APPENDIX B

$\chi^{(3)}$ CONTRIBUTIONS TO SUM-FREQUENCY SPECTRA

When ionic surfactants adsorb to the oil-water interface an interfacial potential will develop, with the interfacial charge density dependent on the surfactant surface density. The presence of this charge establishes a static electric field (E_{DC}) that can lead to third-order ($\chi^{(3)}$) changes from the resonant second-order sum-frequency lineshapes. This appendix is purposed towards aiding in the discussion of $\chi^{(3)}$ effects on the oil phase spectra in Chapter IV (Figure 4.7). In order to accomplish that purpose the effects of a $\chi^{(3)}$ will be briefly summarized, followed by a simple model to illustrate how sum-frequency spectra will change depending on the sign of the potential. References on $\chi^{(3)}$ interference effects within second-order spectroscopies will be provided at the end of this section for the interested reader.

Recall from Chapter II the sum-frequency electric field is dependent upon the incident electric fields, of the infrared and visible beams, as well as the second-order nonlinear susceptibility (equation B.1).

$$E_{SF}(\omega) \propto \chi^{(2)} E_{IR} E_{Vis} \tag{B.1}$$

When a static electric field is present at the interface, as a result of ionic surfactant adsorption, third-order contributions can then interfere with the second-order vibrational line shapes (equation B.2).

$$E_{SF}(\omega) \propto \chi^{(2)} E_{IR} E_{Vis} + \chi^{(3)} E_{IR} E_{Vis} E_{DC} \tag{B.2}$$

Quantifying the complete response requires integration over the depth that the static electric field penetrates into the bulk solvent.

Begin by replacing the static field with a depth (z) dependent integral.

$$E_{SF}(\omega) \propto \chi^{(2)} E_{IR} E_{Vis} + \chi^{(3)} E_{IR} E_{Vis} \int_0^\infty E_{DC}\,(z)\, dz$$

(B.3)

The depth dependent electric field can be re-expressed as the negative of the derivative of the interfacial potential with respect to the distance from the interface. Evaluating the integral in equation B.3, the sum-frequency electric field becomes,

$$E_{SF}(\omega) \propto \chi^{(2)} E_{IR} E_{Vis} - \chi^{(3)} E_{IR} E_{Vis} \big(\phi(\infty) - \phi(0)\big)$$

(B.4)

Given that at infinite distance from the interface the potential drops to zero, equation B.4 can be re-written as:

$$E_{SF}(\omega) \propto \chi^{(2)} E_{IR} E_{Vis} + \chi^{(3)} E_{IR} E_{Vis} \phi(0)$$

(B.5)

The interfacial potential, $\phi(0)$, can be modeled by several models, however the Gouy-Chapman is chosen here for illustrating $\chi^{(3)}$ interference. The interfacial potential is written in the familiar form of the Gouy-Chapman model:

$$\phi(0) = \frac{2k_B T}{e} sinh^{-1}\left(\frac{\sigma}{\sqrt{8000 k_B T N_a \varepsilon_0 \varepsilon c}}\right)$$

(B.6)

where the physical constants all have their standard definitions, c is the ionic strength, σ is the interfacial charge density, and ε is the solvent dielectric constant.

In order to model the effects of the $\chi^{(3)}$ interference on the CH stretching spectra, equation B.6 is plugged into equation B.5. For the $\chi^{(2)}$ response, four resonances are included. These correspond to the methylene (2850 cm^{-1}) and methyl (2875 cm^{-1}) symmetric stretches, an asymmetric stretch (2905 cm^{-1}) and Fermi resonance (2935 cm^{-1}). All resonances are modeled using a lorentzian lineshapes. The relative intensities and linewidths were chosen to visually resemble the shape of the oil phase spectra. Several spectra were simulated by calculating three different interfacial potentials by inserting three different surface charge densities into the Gouy-Chapman model. These included two charge densities of equal magnitude, but opposite sign, and a zero charge density input. The results of these simulated spectra are displayed in Figure B.1.

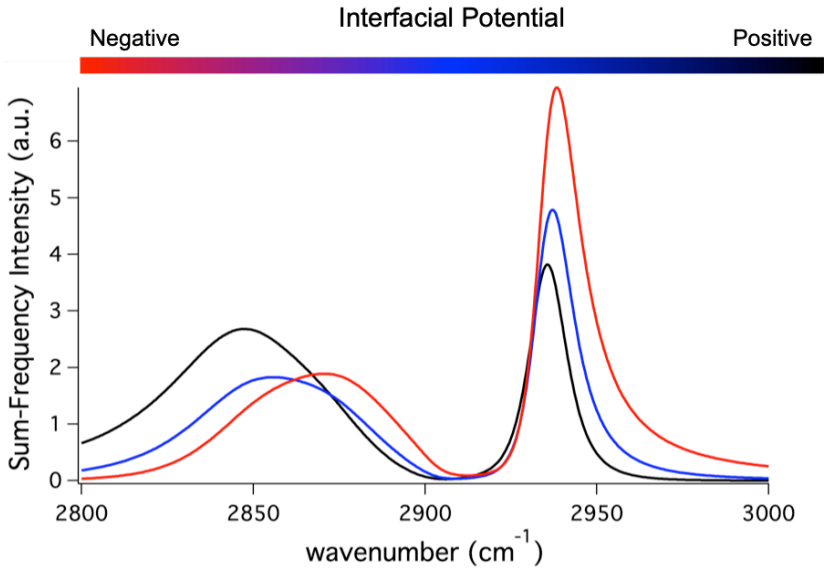

Figure B.5. Simulated spectra illustrating the effects of $\chi^{(3)}$ interferences on sum-frequency spectra. The $\chi^{(2)}$ lineshape without any higher-order interferences (blue) is compared to interferences arising from a positive (black) and negative (red) interfacial potential. Positive and negative charge densities possessed similar magnitudes.

The blue spectrum within Figure B.1 is calculated solely from model vibrational resonances and no $\chi^{(3)}$ response, as the interfacial charge density was set to zero. The black and red traces were calculated using the same vibrational resonances as the blue trace, but have the same magnitude charge density with positive and negative signs, respectively. Note that the resonant contributions were held constant for all calculated spectra. From these model spectra one can easily see how the baseline response on the low energy and high energy sides of the spectra will alternatively rise depending on the sign of the interfacial potential. Similarly, while there are absolutely frequency shifts observed in the maximum intensity, the underlying resonant frequencies have not changed and the source of the apparent frequency shifts arise from the $\chi^{(3)}$ interference.

The purpose of these model spectra was to illustrate the possible effects that higher order interferences can have on sum-frequency spectra. While the oil phase spectra were not fit due to low spectral resolution, the maximum intensity and elevated baseline spectral response on the low and high-energy sides of the spectra can be replicated using a simple $\chi^{(3)}$ model. It should be noted that the effects of $\chi^{(3)}$ interferences can me more nuanced than represented in this brief discussion. For example, the model presented here ignores any optical dispersion occurring within the diffuse layer.[70, 91, 168, 214-215] It has also been suggested that the effects of $\chi^{(3)}$ interferences will manifest differently in reflection and scattering sum-frequency spectroscopy.[70, 91] For the reader interested in learning more, they are referred to the preceding references as well as the following sources and the references within.[148, 216-218]

APPENDIX C

MODELING SURFACTANT ADSORPTION WITH THE LANGMUIR MODEL

A simple Langmuir model was chosen to describe changes in surface pressure and sum-frequency intensity induced by the addition of salt. Application of the Langmuir model assumes that the oil-water interface is a "lattice" of adsorption sites that are non-interacting and can be either filled or empty.[33, 202] Adsorption of surfactants to these sites can be considered as a reaction where a bulk surfactant (S_{AOT}) plus an empty site (ES) "react" to form a filled site (FS), or surface surfactant. The rate equation for such a reaction is expressed in equation C.1, where the forward and reverse reaction rates are given as k_1 and k_{-1}, respectively.

$$S_{AOT} + ES \underset{k_{-1}}{\overset{k_1}{\rightleftharpoons}} FS \tag{C.1}$$

The kinetic equation for such a reaction would be,

$$\frac{dN}{dt} = k_1 \frac{(C - N)(N_{max} - N)}{55.5} - k_{-1} \tag{C.2}$$

where N is the number of adsorbed molecules, N_{max} is the maximum possible number of adsorbed molecules, C is the total number of molecules in solution, and 55.5 is the molarity of water. It follows that $\frac{(C-N)}{55.5}$ is the mole fraction of molecules remaining in the

solution bulk after N have adsorbed to the surface. Typically $(C - N) \approx 0$, because the number of adsorbed molecules to the planar surface is small compared to the total number of molecule in solution.[206] Under this approximation equation B.2 is simplified and rewritten as equation B.3.

$$\frac{N}{N_{max}} = \frac{1}{1 + \frac{55.5}{KC}} \tag{C.3}$$

Equation B.3 expresses the adsorption reaction in terms of its relative surface coverage with $K = \frac{k_1}{k_{-1}}$ as the adsorption reaction equilibrium constant. It follows that as the surfactant reaches its maximum surface coverage any observable monitoring the adsorption process will also plateau.

Since surface pressure and sum-frequency measurements are different measurements, the Langmuir model is re-written in order to be generalizable to both experimental techniques, so long as any changes in signal can be directly attributable to changes in surface adsorption.

$$Obs(C) = \frac{A}{1 + \frac{55.5}{Ce^{\frac{-\Delta G}{RT}}}} + Obs_0 \tag{C.4}$$

In equation C.4 the observable (Obs) of a measurement of a chemical system with a certain salt concentration (C) is modeled as a Langmuir adsorption isotherm, but with an amplitude (A) and a baseline value (Obs_0). The amplitude is necessary to adjust the isotherm to the scale of the measurement made, while the baseline value is necessary

since the surface pressure and VSFSS intensity of AOT solutions and nanoemulsions free of salt are non-zero. The equilibrium constant has been exchanged for a change in free energy according to the equation, $K = e^{\frac{-\Delta G}{RT}}$, where R is the ideal gas constant and T is the temperature.

The free parameters in this model are A, Obs_0, and ΔG. Figure C.1 illustrates how adjusting each parameter change changes the model. Holding ΔG constant and adjusting the amplitude or baseline value (Figure C.1a-b) results in a change in magnitude or vertical shift of the trace. These parameters will adjust the fits to the order of magnitude of the surface pressure or VSFSS observable and the baseline value of salt free samples. Setting the amplitude to 1 and baseline value to 0, ΔG was varied between -20 kJ/mol and -30 kJ/mol (Figure C.1c). The concentration dependence in the observable is clearly different for each trace.

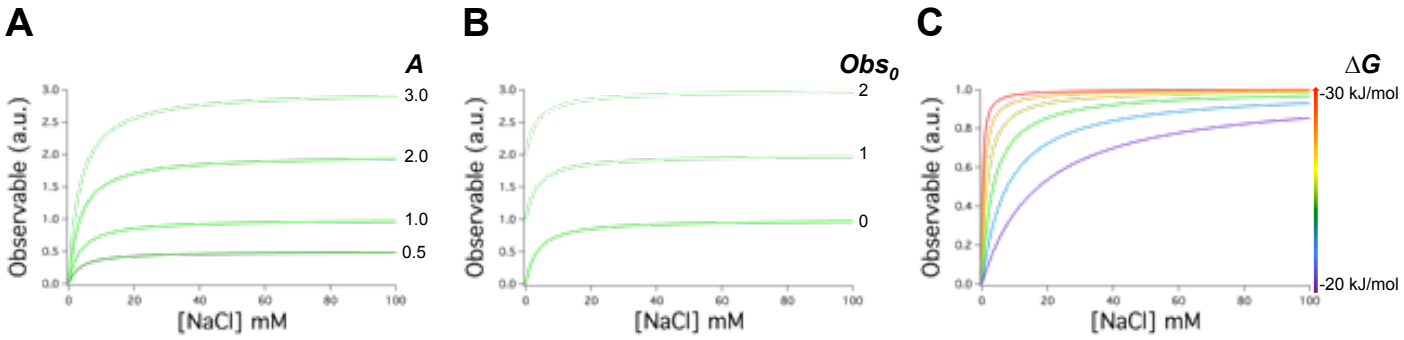

Figure C.1. Demonstration how changes to the (A) amplitude, (B) baseline value, and (C) ΔG affect the Langmuir Model.

The most desirable feature for any model used to compare adsorption at different interfaces, and observed with different techniques, is a limited number of adjustable

parameters. With the Langmuir model only one adjustable parameter (ΔG) is used to fit the concentration dependence. By comparing the ΔG value across different observables, similarities or differences in salt induced changes to surfactant adsorption are, therefore, able to be quantitatively assessed.

APPENDIX D

SUM-FREQUENCY PEAK ASSIGNMENTS

Aggregated in this appendix are the peak frequencies and assignments for sum-frequency fits discussed in this thesis.

Table D.1. Peaks used to fit the aqueous phase spectra of the bare planar oil-water and LCNE interfaces (Figures 4.4., 4.5.)

Interface	**Bound OD**	**Free OD_{HOD}**	**Free OD_{D2O}**
Planar CCl_4-D2O	2530 cm^{-1}	N/A	2715 cm^{-1}
Planar CCl_4-HOD	2530 cm^{-1}	2699 cm^{-1}	2715 cm^{-1}
LCNE Surface	2550 cm^{-1}	2690 cm^{-1}	2703 cm^{-1}

Table D.2. Peaks used to fit CTAB CH stretching spectra in Figure 5.2.

	Peak Frequency	Peak Assignment
Peak 1	2857 cm^{-1}	Methylene Symmetric Stretch
Peak 2	2876 cm^{-1}	Methyl Symmetric Stretch
Peak 3	2907 cm^{-1}	Methylene Asymmetric Stretch
Peak 4	2938 cm^{-1}	Methyl Fermi Resonance
Peak 5	2975 cm^{-1}	Headgroup Methyl Asymmetric Stretches

Table D.3. Peak frequencies and assignments used to fit AOT CH stretching spectra at nanoemulsion and planar oil-water interfaces (Figure 5.4.a-c, 5.5., 5.6., 5.7. 5.11a, 6.2)

	Regular Nanoemulsion	Reverse Nanoemulsion	Planar Oil-Water Interface	Peak Assignment
Peak 1	2856 cm^{-1}	2856 cm^{-1}	2856 cm^{-1}	Methylene Symmetric Stretch
Peak 2	2872 cm^{-1}	2872 cm^{-1}	2869 cm^{-1}	Methyl Symmetric Stretch
Peak 3	2905 cm^{-1}	2905 cm^{-1}	2908 cm^{-1}	Methyne Stretch
Peak 4	2933 cm^{-1}	2933 cm^{-1}	2932 cm^{-1}	Methyl Fermi Resonance

Table D.4. Peak frequencies and assignment used to fit AOT SO stretching spectra taken of the reverse nanoemulsion and planar oil-water interface.

	Reverse Nanoemulsion	Planar Oil-Water Interface
Na:AOT	1045 cm^{-1}	1048 cm^{-1}
K:AOT	1045 cm^{-1}	1048 cm^{-1}
Mg:AOT	1045 cm^{-1}	1048 cm^{-1}

REFERENCES CITED

1. Sonnevilleaubrun, O. Nanoemulsions: a new vehicle for skincare products. *Advances in Colloid and Interface Science* **2004,** *108-109*, 145-149.

2. Sonneville-Aubrun, O.; Yukuyama, M. N.; Pizzino, A. Chapter 14 - Application of Nanoemulsions in Cosmetics. In *Nanoemulsions*, Jafari, S. M.; McClements, D. J., Eds. Academic Press: 2018; pp 435-475.

3. Che Marzuki, N. H.; Wahab, R. A.; Abdul Hamid, M. An overview of nanoemulsion: concepts of development and cosmeceutical applications. *Biotechnology & Biotechnological Equipment* **2019,** *33* (1), 779-797.

4. Rocca, S. G.-C., M. J.; Caldero,G.; Pons, R.; Solans, C.; Stebe, M. J. Hydrophilic model drug delivery from concentrated reverse emulsions. *Langmuir* **1998,** *14* (24), 6840-6845.

5. Müller-Goymann, C. C. Physicochemical characterization of colloidal drug delivery systems such as reverse micelles, vesicles, liquid crystals and nanoparticles for topical administration. *European Journal of Pharmaceutics and Biopharmaceutics* **2004,** *58* (2), 343-356.

6. Javadi, M.; Pitt, W. G.; Belnap, D. M.; Tsosie, N. H.; Hartley, J. M. Encapsulating nanoemulsions inside eliposomes for ultrasonic drug delivery. *Langmuir* **2012,** *28* (41), 14720-14729.

7. Lu, G. W.; Gao, P. Emulsions and Microemulsions for Topical and Transdermal Drug Delivery. 2010; pp 59-94.

8. Szczepanowicz, K.; Bazylinska, U.; Pietkiewicz, J.; Szyk-Warszynska, L.; Wilk, K. A.; Warszynski, P. Biocompatible long-sustained release oil-core polyelectrolyte nanocarriers: From controlling physical state and stability to biological impact. *Advances in Colloid and Interface Science* **2015,** *222*, 678-691.

9. Rai, V. K.; Mishra, N.; Yadav, K. S.; Yadav, N. P. Nanoemulsion as pharmaceutical carrier for dermal and transdermal drug delivery: Formulation development, stability issues, basic considerations and applications. *Journal of Controlled Release* **2018,** *270*, 203-225.

10. Nakano, Y.; Tajima, M.; Sugiyama, E.; Sato, V. H.; Sato, H. Development of a Novel Nano-emulsion Formulation to Improve Intestinal Absorption of Cannabidiol. *Medical Cannabis and Cannabinoids* **2019,** *2* (1), 35-42.

11. Czarnecki, J. Stabilization of water in crude oil emulsions. Part 2. *Energy & Fuels* **2009,** *23* (3), 1253-1257.

12. Alvarez, G.; Jestin, J.; Argillier, J. F.; Langevin, D. Small-angle neutron scattering study of crude oil emulsions: Structure of the oil-water interfaces. *Langmuir* **2009,** *25* (7), 3985-3990.

13. Athas, J. C.; Jun, K.; McCafferty, C.; Owoseni, O.; John, V. T.; Raghavan, S. R. An Effective Dispersant for Oil Spills Based on Food-Grade Amphiphiles. *Langmuir* **2014,** *30* (31), 9285-9294.

14. Riehm, D. A.; Rokke, D. J.; Paul, P. G.; Lee, H. S.; Vizanko, B. S.; McCormick, A. V. Dispersion of oil into water using lecithin-Tween 80 blends:The role of spontaneous emulsification. *Journal of Colloid and Interface Science* **2017,** *487*, 52-59.

15. Julian McClements, D. Edible nanoemulsions: fabrication, properties, and functional performance. *Soft Matter* **2011,** *7* (6), 2297-2316.

16. McClements, D. J.; Rao, J. Food-Grade Nanoemulsions: Formulation, Fabrication, Properties, Performance, Biological Fate, and Potential Toxicity. *Critical Reviews in Food Science and Nutrition* **2011,** *51* (4), 285-330.

17. McClements, D. J. Nanoemulsions versus microemulsions: Terminology, differences and similarities. *Soft Matter* **2012,** *8*, 1719-1730.

18. Komaiko, J. S.; McClements, D. J. Formation of Food-Grade Nanoemulsions Using Low-Energy Preparation Methods: A Review of Available Methods. *Comprehensive Reviews in Food Science and Food Safety* **2016,** *15* (2), 331-352.

19. Eastoe, J.; Hollamby, M. J.; Hudson, L. Recent advances in nanoparticle synthesis with reversed micelles. *Advances in Colloid and Interface Science* **2006,** *128-130*, 5-15.

20. Muñoz-Espí, R.; Álvarez-Bermúdez, O. Chapter 15 - Application of Nanoemulsions in the Synthesis of Nanoparticles. In *Nanoemulsions*, Jafari, S. M.; McClements, D. J., Eds. Academic Press: 2018; pp 477-515.

21. Gupta, A.; Eral, H. B.; Hatton, T. A.; Doyle, P. S. Nanoemulsions: formation, properties and applications. *Soft Matter* **2016,** *12* (11), 2826-2841.

22. Kini, G. C.; Biswal, S. L.; Wong, M. S.; Miller, C. A. Characteristics of spontaneously formed nanoemulsions in octane/AOT/brine systems. *Journal of Colloid and Interface Science* **2012,** *385* (1), 111-121.

23. Izquierdo, P.; Esquena, J.; Tadros, T. F.; Dederen, C.; Garcia, M. J.; Azemar, N.; Solans, C. Formation and Stability of Nano-Emulsions Prepared Using the Phase Inversion Temperature Method. *Langmuir* **2002,** *18* (1), 26-30.

24. Izquierdo, P.; Esquena, J.; Tadros, T. F.; Dederen, J. C.; Feng, J.; Garcia-Celma, M. J.; Azemar, N.; Solans, C. Phase Behavior and Nano-emulsion Formation by the Phase Inversion Temperature Method. *Langmuir* **2004,** *20* (16), 6594-6598.

25. Tadros, T.; Izquierdo, P.; Esquena, J.; Solans, C. Formation and stability of nano-emulsions. *Advances in Colloid and Interface Science* **2004,** *108-109*, 303-318.

26. Yuan, Y.; Gao, Y.; Mao, L.; Zhao, J. Optimisation of conditions for the preparation of β-carotene nanoemulsions using response surface methodology. *Food Chemistry* **2008,** *107* (3), 1300-1306.

27. Yuan, Y.; Gao, Y.; Zhao, J.; Mao, L. Characterization and stability evaluation of β-carotene nanoemulsions prepared by high pressure homogenization under various emulsifying conditions. *Food Research International* **2008,** *41* (1), 61-68.

28. Mewis, J.; Wagner, N. J. *Colloidal Suspension Rheology*. Cambridge University Press: Cambridge, 2011.

29. Fryd, M. M.; Mason, T. G. Advanced Nanoemulsions. *Annual Review of Physical Chemistry* **2012,** *63* (1), 493-518.

30. Helgeson, M. E.; Moran, S. E.; An, H. Z.; Doyle, P. S. Mesoporous organohydrogels from thermogelling photocrosslinkable nanoemulsions. *Nature Materials* **2012,** *11* (4), 344-352.

31. Wilking, J.; Mason, T. Irreversible shear-induced vitrification of droplets into elastic nanoemulsions by extreme rupturing. *Physical Review E* **2007,** *75* (4).

32. Delmas, T.; Piraux, H.; Couffin, A.-C.; Texier, I.; Vinet, F.; Poulin, P.; Cates, M. E.; Bibette, J. How To Prepare and Stabilize Very Small Nanoemulsions. *Langmuir* **2011,** *27* (5), 1683-1692.

33. Rosen, M. J. *Surfactants and Interfacial Phenomena*. 3 ed.; Wiley-Interscience: Hoboken, New Jersey, 2004; p 444.

34. Djerdjev, A. M.; Beattie, J. K.; Hunter, R. J. Stagnant Layer Conduction in Surfactant-Stabilized Hexadecane Emulsion Systems Measured by Electroacoustics. *Australian Journal of Chemistry* **2003,** *56*, 1081-1089.

35. de Aguiar, H. B.; Strader, M. L.; de Beer, A. G. F.; Roke, S. Surface Structure of Sodium Dodecyl Sulfate Surfactant and Oil at the Oil-in-Water Droplet Liquid/Liquid Interface: A Manifestation of a Nonequilibrium Surface State. *The Journal of Physical Chemistry B* **2011,** *115* (12), 2970-2978.

36. Hensel, J. K.; Carpenter, A. P.; Ciszewski, R. K.; Schabes, B. K.; Kittredge, C. T.; Moore, F. G.; Richmond, G. L. Molecular characterization of water and surfactant AOT at nanoemulsion surfaces. *Proceedings of the National Academy of Sciences* **2017,** *114* (51), 13351.

37. El-Sharaky, E. A.; El-Tabey, A. E.; Noor El-Din, M. R.; Al-Sabagh, A. M.; Mishrif, M. R. Polyoxyethylene Alkenyl Succinate Gemini Emulsifier for Diesel Fuel Nanoemulsions. *Energy & Fuels* **2019,** *33* (6), 5476-5487.

38. Kumar, N.; Mandal, A. Oil-in-water nanoemulsion stabilized by polymeric surfactant: Characterization and properties evaluation for enhanced oil recovery. *European Polymer Journal* **2018,** *109*, 265-276.

39. Peng, L.-C.; Liu, C.-H.; Kwan, C.-C.; Huang, K.-F. Optimization of water-in-oil nanoemulsions by mixed surfactants. *Colloids and Surfaces A: Physicochemical and Engineering Aspects* **2010,** *370* (1-3), 136-142.

40. Galindo-Alvarez, J.; Le, K.-A.; Sadtler, V.; Marchal, P.; Perrin, P.; Tribet, C.; Marie, E.; Durand, A. Enhanced stability of nanoemulsions using mixtures of non-ionic surfactant and amphiphilic polyelectrolyte. *Colloids and Surfaces A: Physicochemical and Engineering Aspects* **2011,** *389* (1-3), 237-245.

41. Hunter, R. J. *Foundations of Colloid Science*. 2nd ed.; Oxford University Press: Oxford, 2001; p 806.

42. Marinova, K. G.; Alargova, R. G.; Denkov, N. D.; Velev, O. D.; Petsev, D. N.; Ivanov, I. B.; Borwankar, R. P. Charging of Oil-Water Interfaces Due to Spontaneous Adsorption of Hydroxyl Ions. *Langmuir* **1996,** *12*, 2045-2051.

43. Beattie, J. K. The Intrinsic Charge at the Hydrophobe/Water Interface. In *Colloid Stability: The Role of Surface Forces – Part II*, Tadros, P. D. T. F., Ed. Wiley-VCH: Weinheim, Germany, 2007; Vol. 2, pp 153-164.

44. Rehfeld, S. J. Adsorption of sodium dodecyl sulfate at various hydrocarbon-water interfaces. *The Journal of Physical Chemistry* **1967,** *71* (3), 738-745.

45. Li, Z. X.; Lu, J. R.; Thomas, R. K. Neutron reflectivity studies of the adsorption of aerosol-OT at the air/water interface: the surface excess. *Langmuir* **1997,** *13* (14), 3681-3685.

46. Scoppola, E.; Micciulla, S.; Kuhrts, L.; Maestro, A.; Campbell, A. R.; Konovalov, V. O.; Fragneto, G.; Schneck, E. Reflectometry Reveals Accumulation of Surfactant Impurities at Bare Oil/Water Interfaces. *Molecules* **2019,** *24* (22).

47. Beattie, J. K.; Djerdjev, A. M. The Pristine Oil/Water Interface: Surfactant-Free Hydroxide-Charged Emulsions**. *Angewandte Chemie International Edition* **2004,** (43), 3568-3571.

48. Creux, P.; Lachaise, J.; Graciaa, A.; Beattie, J. K.; Djerdjev, A. M. Strong Specific Hydroxide Ion Binding at the Pristine Oil/Water and Air/Water Interfaces. *Journal of Physical Chemistry B* **2009,** (113), 14146-14150.

49. de Oca-Ávalos, J. M. M.; Candal, R. J.; Herrera, M. L. Nanoemulsions: stability and physical properties. *Current Opinion in Food Science* **2017,** *16*, 1-6.

50. Moran, P. D.; Bowmaker, G. A.; Cooney, R. P.; Bartlett, J. R.; Woolfrey, J. L. Vibrational Spectroscopic Study of the Structure of Sodium Bis(2-ethylhexyl)sulfosuccinate Reverse Micelles and Water-in-Oil Microemulsions. *Langmuir* **1995,** *11* (3), 738-743.

51. Moilanen, D. E.; Fenn, E. E.; Wong, D.; Fayer, M. D. Water Dynamics in Large and Small Reverse Micelles: From Two Ensembles to Collective Behavior. *The Journal of Chemical Physics* **2009,** *131*, 014704 – 014709.

52. Fenn, E. E.; Wong, W.; Fayer, M. D. Water Dynamics at Neutral and Ionic Interfaces in Reverse Micelles. *Proceedings of the National Academy of Sciences* **2009,** *106*, 15243 – 15248.

53. Levinger, N. E.; Swafford, L. A. Ultrafast Dynamics in Reverse Micelles. *Annu. Rev. Phys. Chem.* **2009**, 385-406.

54. Fayer, M. D.; Levinger, N. E. Analysis of Water in Confined Geometries and at Interfaces. *Annual Review of Analytical Chemistry* **2010,** *3* (1), 89-107.

55. Kumar, S. K. K.; Tamimi, A.; Fayer, M. D. Dynamics in the interior of AOT lamellae investigated with two-dimensional infrared spectroscopy. *Journal of the American Chemical Society* **2013,** *135* (13), 5118-5126.

56. Shen, Y. R. Surface-Properties Probed By 2nd- Harmonic and Sum-Frequency Generation. *Nature* **1989,** *337* (6207), 519-525.

57. Shen, Y. R. Surfaces probed by nonlinear optics. *Surface science* **1994,** *299-300*, 551-562.

58. Richmond, G. L. Molecular Bonding and Interactions at Aqueous Surfaces as Probed by Vibrational Sum Frequency Spectroscopy. *Chemical Reviews* **2002,** *102* (8), 2693-2724.

59. Lambert, A. G.; Davies, P. B.; Neivandt, D. J. Implementing the Theory of Sum Frequency Generation Vibrational Spectroscopy: A Tutorial Review. *Applied Spectroscopy Reviews* **2005,** *40* (2), 103-145.

60. Jubb, A. M.; Hua, W.; Allen, H. C. Environmental Chemistry at Vapor/Water Interfaces: Insights from Vibrational Sum Frequency Generation Spectroscopy. *Annual Review of Physical Chemistry* **2012,** *63* (1), 107-130.

61. Guyot-Sionnest, P.; Hunt, J. H.; Shen, Y. R. Sum-Frequency Vibrational Spectroscopy of a Langmuir Film - Study of Molecular-Orientation of a Two-Dimensional System. *Phys. Rev. Lett.* **1987,** *59* (14), 1597-1600.

62. Auer, B. M.; Skinner, J. L. Vibrational sum-frequency spectroscopy of the liquid/vapor interface for dilute HOD in D2O. *The Journal of Chemical Physics* **2008,** *129* (21), 214705.

63. Cyran, J. D.; Backus, E. H. G.; Nagata, Y.; Bonn, M. Structure from Dynamics: Vibrational Dynamics of Interfacial Water as a Probe of Aqueous Heterogeneity. *The Journal of Physical Chemistry B* **2018,** *122* (14), 3667-3679.

64. Bain, C. D. Sum-frequency vibrational spectroscopy of the solid/liquid interface. *Journal of the Chemical Society, Faraday Transactions* **1995,** *91* (9), 1281-1296.

65. Messmer, M. C.; Conboy, J. C.; Richmond, G. L. Observation of Molecular Ordering at the Liquid-Liquid Interface by Resonant Sum Frequency Generation. *Journal of the American Chemical Society* **1995,** *117* (30), 8039-8040.

66. Scatena, L. F.; Brown, M. G.; Richmond, G. L. Water at Hydrophobic Surfaces: Weak Hydrogen Bonding and Strong Orientational Effects. *Science* **2001,** *292*, 908-912.

67. Moore, F. G.; Richmond, G. L. Integration or Segregation: How Do Molecules Behave at Oil/Water Interfaces? *Accounts of Chemical Research* **2008,** *41* (6), 739-748.

68. Roke, S.; Roeterdink, W. G.; Wijnhoven, J. E. G. J.; Petukhov, A. V.; Kleyn, A. W.; Bonn, M. Vibrational Sum Frequency Scattering from a Submicron Suspension. *Physical Review Letters* **2003,** *91* (25), 258302.

69. Roke, S.; Bonn, M.; Petukhov, A. V. Nonlinear optical scattering: The concept of effective susceptibility. *Physical Review B* **2004,** *70* (11), 115106.

70. Roke, S.; Gonella, G. Nonlinear Light Scattering and Spectroscopy of Particles and Droplets in Liquids. *Annual Review of Physical Chemistry* **2012,** *63* (1), 353-378.

71. de Aguiar, H. B.; de Beer, A. G. F.; Strader, M. L.; Roke, S. The Interfacial Tension of Nanoscopic Oil Droplets in Water Is Hardly Affected by SDS Surfactant. *Journal of the American Chemical Society* **2010,** *132* (7), 2122-2123.

72. Scheu, R.; Chen, Y.; de Aguiar, H. B.; Rankin, B. M.; Ben-Amotz, D.; Roke, S. Specific Ion Effects in Amphiphile Hydration and Interface Stabilization. *Journal of the American Chemical Society* **2014,** *136* (5), 2040-2047.

73. Vácha, R.; Rick, S. W.; Jungwirth, P.; de Beer, A. G. F.; de Aguiar, H. B.; Samson, J.-S.; Roke, S. The Orientation and Charge of Water at the Hydrophobic Oil Droplet–Water Interface. *Journal of the American Chemical Society* **2011,** *133* (26), 10204-10210.

74. Samson, J.-S.; Scheu, R.; Smolentsev, N.; Rick, S. W.; Roke, S. Sum frequency spectroscopy of the hydrophobic nanodroplet/water interface: Absence of hydroxyl ion and dangling OH bond signatures. *Chemical Physics Letters* **2014,** *615*, 124-131.

75. Smolentsev, N.; Smit, W. J.; Bakker, H. J.; Roke, S. The interfacial structure of water droplets in a hydrophobic liquid. *Nature Communications* **2017,** *8*, 15548.

76. Zdrali, E.; Chen, Y.; Okur, H. I.; Wilkins, D. M.; Roke, S. The Molecular Mechanism of Nanodroplet Stability. *ACS Nano* **2017,** *11* (12), 12111-12120.

77. Zdrali, E.; Baer, M. D.; Okur, H. I.; Mundy, C.; Roke, S. The Diverse Nature of Ion Speciation at the Nanoscale Hydrophobic/Water Interface. *The Journal of Physical Chemistry B* **2019**.

78. Mukamel, S. *Principles of Nonlinear Optical Spectroscopy*. Oxford University Press: New York, 1995; p 543.

79. Sutherland, R. L. *Handbook of Nonlinear Optics*. 2nd ed.; Marcel Dekker, Inc.: New York, 2003; p 971.

80. Hamm, P.; Zanni, M. *Concepts and Methods of 2D Infrared Spectroscopy*. Cambridge University Press: New York, 2011; p 286.

81. Shen, Y.-R. *Fundamentals of Sum-Frequency Spectroscopy*. Cambridge University PRess: United Kingdom, 2016.

82. Raymond, E. A.; Richmond, G. L. Probing the Molecular Structure and Bonding of the Surface of Aqueous Salt Solutions. *The Journal of Physical Chemistry B* **2004,** *108* (16), 5051-5059.

83. Yamaguchi, S.; Shiratori, K.; Morita, A.; Tahara, T. Electric quadrupole contribution to the nonresonant background of sum frequency generation at air/liquid interfaces. *The Journal of Chemical Physics* **2011,** *134* (18), 184705.

84. de Beer, A. G. F.; Roke, S. Sum frequency generation scattering from the interface of an isotropic particle: Geometrical and chiral effects. *Physical Review B* **2007,** *75* (24), 245438.

85. de Beer, A. G. F.; Roke, S. Nonlinear Mie theory for second-harmonic and sum-frequency scattering. *Physical Review B* **2009,** *79* (15), 155420.

86. Beer, A. G. F. d.; Roke, S. Obtaining molecular orientation from second harmonic and sum frequency scattering experiments in water: Angular distribution and polarization dependence. *The Journal of Chemical Physics* **2010,** *132* (23), 234702.

87. de Beer, A. G. F.; Campen, R. K.; Roke, S. Separating surface structure and surface charge with second-harmonic and sum-frequency scattering. *Physical Review B* **2010,** *82* (23), 235431.

88. de Beer, A. G. F.; Roke, S.; Dadap, J. *Theory of optical second-harmonic and sum-frequency scattering from arbitrarily shaped particles*. 2011; Vol. 58256420, p 180-4315.

89. Bohren, C. F.; Huffman, D. R. *Absorption and Scattering of Light by Small Particles*. Wiley-Interscience: New York, 2010.

90. Dadap, J. I.; Shan, J.; Heinz, T. F. Theory of optical second-harmonic generation from a sphere of centrosymmetric material: small-particle limit. *JOSA B* **2004,** *21* (7), 1328-1347.

91. Gonella, G.; Lütgebaucks, C.; de Beer, A. G. F.; Roke, S. Second Harmonic and Sum-Frequency Generation from Aqueous Interfaces Is Modulated by Interference. *The Journal of Physical Chemistry C* **2016,** *120* (17), 9165-9173.

92. Moore, F. G.; Becraft, K. A.; Richmond, G. L. Challenges in Interpreting Vibrational Sum Frequency Spectra: Deconvoluting Spectral Features as Demonstrated in the CaF2/H2O/SDS System. *Applied Spectrscopy* **2002,** *56*, 1600-1610.

93. Bain, C. D.; Davies, P. B.; Ong, T. H.; Ward, R. N.; Brown, M. A. Quantitative analysis of monolayer composition by sum-frequency vibrational spectroscopy. *Langmuir* **1991,** *7* (8), 1563-1566.

94. Busson, B.; Tadjeddine, A. Non-Uniqueness of Parameters Extracted from Resonant Second-Order Nonlinear Optical Spectroscopies. *The Journal of Physical Chemistry C* **2009,** *113* (52), 21895-21902.

95. Goates, S. R.; Schofield, D. A.; Bain, C. D. A Study of Nonionic Surfactants at the Air−Water Interface by Sum-Frequency Spectroscopy and Ellipsometry. *Langmuir* **1999,** *15* (4), 1400-1409.

96. Brown, M. G.; Raymond, E. A.; Allen, H. C.; Scatena, L. F.; Richmond, G. L. The Analysis of Interference Effects in the Sum Frequency Spectra of Water Interfaces†. *The Journal of Physical Chemistry A* **2000,** *104* (45), 10220-10226.

97. Ota, S. T.; Richmond, G. L. Uptake of SO2 to Aqueous Formaldehyde Surfaces. *Journal of the American Chemical Society* **2012,** *134* (24), 9967-9977.

98. Beaman, D. K.; Robertson, E. J.; Richmond, G. L. From Head to Tail: Structure, Solvation, and Hydrogen Bonding of Carboxylate Surfactants at the Organic–Water Interface. *The Journal of Physical Chemistry C* **2011,** *115* (25), 12508-12516.

99. Robertson, E. J.; Carpenter, A. P.; Olson, C. M.; Ciszewski, R. K.; Richmond, G. L. Metal Ion Induced Adsorption and Ordering of Charged Macromolecules at the Aqueous/Hydrophobic Liquid Interface. *The Journal of Physical Chemistry C* **2014,** *118* (28), 15260-15273.

100. Schabes, B. K.; Altman, R. M.; Richmond, G. L. Come Together: Molecular Details into the Synergistic Effects of Polymer–Surfactant Adsorption at the Oil/Water Interface. *The Journal of Physical Chemistry B* **2018,** *122* (36), 8582-8590.

101. Altman, R. M.; Richmond, G. L. Coming to Order: Adsorption and Structure of Nonionic Polymer at the Oil/Water Interface as Influenced by Cationic and Anionic Surfactants. *Langmuir* **2020,** *36* (8), 1975-1984.

102. Robertson, E. J. Vibrational Sum Frequency Spectroscopic Investigations of Carboxylic Acid-Containing Polyelectrolytes at the Oil-Water Interface. University of Oregon, Eugene, OR, 2014.

103. Schabes, B. K. Mixtures of Polyelectrolytes and Surfactants at the Oil/Water Interface. University of Oregon, Eugene, OR, 2019.

104. Schabes, B. K.; Hopkins, E. J.; Richmond, G. L. Molecular Interactions Leading to the Coadsorption of Surfactant Dodecyltrimethylammonium Bromide and Poly(styrenesulfonate) at the Oil/Water Interface. *Langmuir* **2019,** *35* (22), 7268-7276.

105. Scatena, L. F.; Richmond, G. L. Isolated Molecular Ion Solvation at an Oil/Water Interface Investigated by Vibrational Sum-Frequency Spectroscopy. *The Journal of Physical Chemistry B* **2004,** *108* (33), 12518-12528.

106. Ohshima, H. Electrophoretic Mobility of Soft Particles. *Journal of Colloid and Interface Science* **1994,** *163* (2), 474-483.

107. Carpenter, A. P.; Tran, E.; Altman, R. M.; Richmond, G. L. Formation and surface-stabilizing contributions to bare nanoemulsions created with negligible surface charge. *Proceedings of the National Academy of Sciences* **2019,** *116* (19), 9214.

108. Carpenter, A. P.; Altman, R. M.; Tran, E.; Richmond, G. L. How Low Can You Go? Molecular Details of Low Charge Nanoemulsion Surfaces. *The Journal of Physical Chemistry B* **2020***,* 124, 20, 4234-4245.

109. Quincke, G. Ueber die Fortführung materieller Theilchen durch strömende Elektricität. *Ann. Phys. Chem.* **1861,** *113*, 513.

110. Takahashi, M. ζ Potential of Microbubbles in Aqueous Solutions: Electrical Properties of the Gas−Water Interface. *The Journal of Physical Chemistry B* **2005,** *109* (46), 21858-21864.

111. Creux, P.; Lachaise, J.; Graciaa, A.; Beattie, J. K. Specific Cation Effects at the Hydroxide-Charged Air/Water Interface. *Journal of Physical Chemistry C* **2007,** (111), 3753-3755.

112. Zimmermann, R.; Dukhin, S.; Werner, C. Electrokinetic Measurements Reveal Interfacial Charge at Polymer Films Caused by Simple Electrolyte Ions. *The Journal of Physical Chemistry B* **2001,** *105* (36), 8544-8549.

113. Hozumi, A.; Sugimura, H.; Yokogawa, Y.; Kameyama, T.; Takai, O. ζ-Potentials of planar silicon plates covered with alkyl- and fluoroalkylsilane self-assembled monolayers. *Colloids and Surfaces A: Physicochemical and Engineering Aspects* **2001,** *182* (1), 257-261.

114. Schweiss, R.; Werner, C.; Knoll, W. Impedance spectroscopy studies of interfacial acid–base reactions of self-assembled monolayers. *Journal of Electroanalytical Chemistry* **2003,** *540*, 145-151.

115. Beattie, J. K.; Djerdjev, A. M.; Warren, G. G. The surface of neat water is basic. *Faraday Discussions* **2008,** *141*, 31-39.

116. Yan, X.; Delgado, M.; Aubry, J.; Gribelin, O.; Stocco, A.; Boisson-Da Cruz, F.; Bernard, J.; Ganachaud, F. Central Role of Bicarbonate Anions in Charging Water/Hydrophobic Interfaces. *The Journal of Physical Chemistry Letters* **2018,** *9* (1), 96-103.

117. Yan, X.; Stocco, A.; Bernard, J.; Ganachaud, F. Freeze/Thaw-Induced Carbon Dioxide Trapping Promotes Emulsification of Oil in Water. *The Journal of Physical Chemistry Letters* **2018,** *9* (20), 5998-6002.

118. Vácha, R.; Marsalek, O.; Willard, A. P.; Bonthuis, D. J.; Netz, R. R.; Jungwirth, P. Charge Transfer between Water Molecules As the Possible Origin of the Observed Charging at the Surface of Pure Water. *The Journal of Physical Chemistry Letters* **2012,** *3* (1), 107-111.

119. Wick, C. D.; Lee, A. J.; Rick, S. W. How intermolecular charge transfer influences the air-water interface. *The Journal of Chemical Physics* **2012,** *137* (15), 154701.

120. Poli, E.; Jong, K. H.; Hassanali, A. Charge transfer as a ubiquitous mechanism in determining the negative charge at hydrophobic interfaces. *Nature Communications* **2020,** *11* (1), 901.

121. Roger, K.; Cabane, B. Why Are Hydrophobic/Water Interfaces Negatively Charged? *Angewandte Chemie International Edition* **2012,** (51), 5625-5628.

122. Uematsu, Y.; Bonthuis, D. J.; Netz, R. R. Charged Surface-Active Impurities at Nanomolar Concentration Induce Jones–Ray Effect. *The Journal of Physical Chemistry Letters* **2018,** *9* (1), 189-193.

123. Duignan, T. T.; Peng, M.; Nguyen, A. V.; Zhao, X. S.; Baer, M. D.; Mundy, C. J. Detecting the undetectable: The role of trace surfactant in the Jones-Ray effect. *Journal of Chemical Physics* **2018,** *149*, 194702.

124. Uematsu, Y.; Bonthuis, D. J.; Netz, R. R. Impurity effects at hydrophobic surfaces. *Current Opinion in Electrochemistry* **2019,** *13*, 166-173.

125. Uematsu, Y.; Bonthuis, D. J.; Netz, R. R. Nanomolar Surface-Active Charged Impurities Account for the Zeta Potential of Hydrophobic Surfaces. *Langmuir* **2020,** *36* (13), 3645-3658.

126. Gan, W.; Wu, W.; Yang, F.; Hu, D.; Fang, H.; Lan, Z.; Yuan, Q. The behavior of hydroxide and hydronium ions at the hexadecane–water interface studied with second harmonic generation and zeta potential measurements. *Soft Matter* **2017,** *13* (43), 7962-7968.

127. Winter, B.; Faubel, M.; Vácha, R.; Jungwirth, P. Behavior of hydroxide at the water/vapor interface. *Chemical Physics Letters* **2009,** *474*, 241-247.

128. Tarbuck, T. L.; Ota, S. T.; Richmond, G. L. Spectroscopic Studies of Solvated Hydrogen and Hydroxide Ions at Aqueous Surfaces. *Journal of the American Chemical Society* **2006,** *128*, 14519-14527.

129. McFearin, C. L. Investigations of the Molecular Structure and Bonding of Water at the Liquid-Liquid Interface Utilizing Vibrational Sum-Frequency Spectroscopy. University of Oregon, Eugene, OR, 2009.

130. Imamura, T.; Ishiyama, T.; Morita, A. Molecular Dynamics Analysis of NaOH Aqueous Solution Surface and the Sum Frequency Generation Spectra: Is Surface OH– Detected by SFG Spectroscopy? *The Journal of Physical Chemistry C* **2014,** *118* (50), 29017-29027.

131. Wick, C. D.; Dang, L. X. The behavior of NaOH at the air-water interface: A computational study. *The Journal of Chemical Physics* **2010,** *133*, 024705.

132. Tse, Y.-L. S.; Chen, C.; Lindberg, G. E.; Kumar, R.; Voth, G. A. Propensity of Hydrated Excess Protons and Hydroxide Anions for the Air–Water Interface. *Journal of the American Chemical Society* **2015,** *137* (39), 12610-12616.

133. Washburn, E. W.; West, C. J. *International critical tables of numerical data, physics, chemistry and technology*. 1st ed. ed.; New York Pub. for the National research council by the McGraw-Hill Book Company, Inc.: New York, 1926.

134. Richmond, G. L. Structure and bonding of molecules at aqueous surfaces. *Annual Review of Physical Chemistry* **2001,** *52* (1), 357-389.

135. Nihonyanagi, S.; Mondal, J. A.; Yamaguchi, S.; Tahara, T. Structure and Dynamics of Interfacial Water Studied by Heterodyne-Detected Vibrational Sum-Frequency Generation. *Annual Review of Physical Chemistry* **2013,** *64* (1), 579-603.

136. Agmon, N.; Bakker, H. J.; Campen, R. K.; Henchman, R. H.; Pohl, P.; Roke, S.; Thämer, M.; Hassanali, A. Protons and Hydroxide Ions in Aqueous Systems. *Chemical Reviews* **2016,** *116* (13), 7642-7672.

137. Bonthuis, D. J.; Horinek, D.; Bocquet, L.; Netz, R. R. Electrokinetics at Aqueous Interfaces without Mobile Charges. *Langmuir* **2010,** *26* (15), 12614-12625.

138. Beattie, J. K.; Gray-Weale, A. Oil/Water Interface Charged by Hydroxide Ions and Deprotonated Fatty Acids: A Comment. *Angewandte Chemie International Edition* **2012,** (51), 12941-12942.

139. Li, Z.; Wang, Y.; Kozbial, A.; Shenoy, G.; Zhou, F.; McGinley, R.; Ireland, P.; Morganstein, B.; Kunkel, A.; Surwade, S. P.; Li, L.; Liu, H. Effect of airborne contaminants on the wettability of supported graphene and graphite. *Nature Materials* **2013,** *12* (10), 925-931.

140. Mücksch, C.; Rösch, C.; Müller−Renno, C.; Ziegler, C.; Urbassek, H. M. Consequences of Hydrocarbon Contamination for Wettability and Protein Adsorption on Graphite Surfaces. *The Journal of Physical Chemistry C* **2015,** *119* (22), 12496-12501.

141. Li, Z.; Kozbial, A.; Nioradze, N.; Parobek, D.; Shenoy, G. J.; Salim, M.; Amemiya, S.; Li, L.; Liu, H. Water Protects Graphitic Surface from Airborne Hydrocarbon Contamination. *ACS Nano* **2016,** *10* (1), 349-359.

142. Duignan, T. T.; Zhao, X. S. Impurities Limit the Capacitance of Carbon-Based Supercapacitors. *The Journal of Physical Chemistry C* **2019,** *123* (7), 4085-4093.

143. Goebel, A.; Lunkenheimer, K. Interfacial Tension of the Water/n-Alkane Interface. *Langmuir* **1997,** *13* (2), 369-372.

144. Morigaki, K.; Walde, P. Fatty acid vesicles. *Current Opinion in Colloid & Interface Science* **2007,** *12* (2), 75-80.

145. Holte, L. K.; Kuran, B. A.; Richmond, G. L.; Johnson, K. E. Computational Modeling of Lauric Acid at the Organic–Water Interface. *The Journal of Physical Chemistry C* **2014,** *118* (19), 10024-10032.

146. Jena, K. C.; Scheu, R.; Roke, S. Surface Impurities Are Not Responsible For the Charge on the Oil/Water Interface: A Comment. *Angewandte Chemie International Edition* **2012,** (51), 12938-12940.

147. Gragson, D. E.; Richmond, G. L. Probing the Structure of Water Molecules at an Oil/Water Interface in the Presence of a Charged Soluble Surfactant through Isotopic Dilution Studies. *The Journal of Physical Chemistry B* **1998,** *102* (3), 569-576.

148. Gragson, D. E.; Richmond, G. L. Potential Dependent Alignment and Hydrogen Bonding of Water Molecules at Charged Air/Water and CCl4/Water Interfaces. *Journal of the American Chemical Society* **1998,** *120*, 366-375.

149. Tyrode, E.; Johnson, C. M.; Rutland, M. W.; Claesson, P. M. Structure and Hydration of Poly(ethylene oxide) Surfactants at the Air/Liquid Interface. A Vibrational Sum Frequency Spectroscopy Study. *The Journal of Physical Chemistry C* **2007,** *111* (31), 11642-11652.

150. McFearin, C. L.; Beaman, D. K.; Moore, F. G.; Richmond, G. L. From Franklin to Today: Toward a Molecular Level Understanding of Bonding and Adsorption at the Oil−Water Interface. *The Journal of Physical Chemistry C* **2009,** *113* (4), 1171-1188.

151. Holmes, J. R.; Kivelson, D.; Drinkard, W. C. Proton Magnetic Resonance Spectrum of HDO. *The Journal of Chemical Physics* **1962,** *37* (1), 150-152.

152. Brown, M. G.; Walker, D. S.; Raymond, E. A.; Richmond, G. L. Vibrational Sum-Frequency Spectroscopy of Alkane/Water Interfaces: Experiment and Theoretical Simulation. *Journal of Physical Chemistry B* **2003,** *107*, 237-244.

153. Chang, T.-M.; Dang, L. X. Molecular dynamics simulations of CCl4-H2O liquid-liquid interface with polarizable potential models. *The Journal of Chemical Physics* **1996,** *104*, 6772-6783.

154. Hore, D. K.; Walker, D. S.; Richmond, G. L. Layered Organic Structure at the Carbon Tetrachloride−Water Interface. *Journal of the American Chemical Society* **2007,** *129* (4), 752-753.

155. Hopkins, A. J.; Richmond, G. L. The Water–Hydrophobic Interface: Neutral and Charged Solute Adsorption at Fluorocarbon and Hydrocarbon Self-Assembled Monolayers (SAMs). *Applied Spectrscopy* **2013,** *67*, 261-273.

156. Stiopkin, I. V.; Weeraman, C.; Pieniazek, P. A.; Shalhout, F. Y.; Skinner, J. L.; Benderskii, A. V. Hydrogen bonding at the water surface revealed by isotopic dilution spectroscopy. *Nature* **2011,** *474*, 192-195.

157. Sun, S.; Tang, F.; Imoto, S.; Moberg, D. R.; Ohto, T.; Paesani, F.; Bonn, M.; Backus, E. H. G.; Nagata, Y. Orientational Distribution of Free O-H Groups of Interfacial Water is Exponential. *Physical Review Letters* **2018,** *121* (24), 246101.

158. Gan, W.; Feng, R.-R.; Wang, H.-F. Comment on ``Orientational Distribution of Free OH Groups of Interfacial Water is Exponential". *Physical Review Letters* **2019,** *123* (9), 099601.

159. Sun, S.; Tang, F.; Imoto, S.; Moberg, D. R.; Ohto, T.; Paesani, F.; Bonn, M.; Backus, E. H. G.; Nagata, Y. Sun et al. Reply. *Physical Review Letters* **2019,** *123* (9), 099602.

160. Knecht, V.; Risselada, H. J.; Mark, A. E.; Marrink, S. J. Electrophoretic mobility does not always reflect the charge on an oil droplet. *Journal of Colloid and Interface Science* **2008,** *318*, 477-486.

161. Hore, D. K.; Tyrode, E. Probing Charged Aqueous Interfaces Near Critical Angles: Effect of Varying Coherence Length. *The Journal of Physical Chemistry C* **2019,** *123* (27), 16911-16920.

162. Fukuto, M.; Ocko, B. M.; Bonthuis, G. J.; Netz, R. R.; Steinrück, H.-G.; Pontoni, D.; Kuzmenko, I.; Haddad, J.; Deutsch, M. Nanoscale structure of the oil-water interface. *Physical Review Letters* **2016,** *117*, 256102.

163. Rivera, J.; McCabe, C.; Cummings, P. Molecular Simulations of Liquid-Liquid Interfacial Properties: Water-n-Alkane and Water-Methanol-n-Alkane Systems. *Physical review. E, Statistical, nonlinear, and soft matter physics* **2003,** *67*, 011603.

164. Chowdhary, J.; Ladanyi, B. M. Water−Hydrocarbon Interfaces: Effect of Hydrocarbon Branching on Interfacial Structure. *The Journal of Physical Chemistry B* **2006,** *110* (31), 15442-15453.

165. Esenturk, O.; Walker, R. A. Surface Structure at Hexadecane and Halo-hexadecane Liquid/Vapor Interfaces. *The Journal of Physical Chemistry B* **2004,** *108* (30), 10631-10635.

166. Esenturk, O.; Walker, R. A. Surface vibrational structure at alkane liquid/vapor interfaces. *The Journal of Chemical Physics* **2006,** *125* (17), 174701.

167. Kovacik, F.; Okur, H. I.; Smolentsev, N.; Scheu, R.; Roke, S. Hydration mediated interfacial transitions on mixed hydrophobic/hydrophilic nanodroplet interfaces. *The Journal of Chemical Physics* **2018,** *149* (23), 234704.

168. Ohno, P. E.; Wang, H.-F.; Geiger, F. M. Second-order spectral lineshapes from charged interfaces. *Nature Communications* **2017,** *8* (1), 1032.

169. Onori, G.; Santucci, A. IR investigations of water structure in Aerosol OT reverse micellar aggregates. **1993,** *97* (20), 5430-5434.

170. Moran, P. D.; Bowmaker, G. A.; Cooney, R. P.; Bartlett, J. R.; Woolfrey, J. L. Vibrational spectra of metal salts of bis(2-ethylhexyl)sulfosuccinate (AOT). *Journal of Materials Chemistry* **1995,** *5*, 295-302.

171. Conboy, J. C.; Messmer, M. C.; Richmond, G. L. Investigation of surfactant conformation and order at the liquid-liquid interface by total internal reflection sum-frequency vibrational spectroscopy. *The Journal of Physical Chemistry* **1996,** *100*, 7617-7622.

172. Conboy, J. C.; Messmer, M. C.; Richmond, G. L. Dependence of alkyl chain conformation of simple ionic surfactants on head group functionality as studied by vibrational sum-frequency spectroscopy. *The Journal of Physical Chemistry B* **1997,** *101* (34), 6724-6733.

173. Knock, M. M.; Bell, G. R.; Hill, E. K.; Turner, H. J.; Bain, C. D. Sum-Frequency Spectroscopy of Surfactant Monolayers at the Oil−Water Interface. *The Journal of Physical Chemistry B* **2003,** *107* (39), 10801-10814.

174. de Aguiar, H. B.; Samson, J.-S.; Roke, S. Probing nanoscopic droplet interfaces in aqueous solution with vibrational sum-frequency scattering: A study of the effects of path length, droplet density and pulse energy. *Chemical Physics Letters* **2011,** *512* (1-3), 76-80.

175. Fainerman, V. B. Adsorption kinetics from concentrated micellar solutions of ionic surfactants at the water—air interface. *Colloids and Surfaces* **1992,** *62* (4), 333-347.

176. Eastoe, J.; Rankin, A.; Wat, R.; Bain, C. D. Surfactant adsorption dynamics. *International Reviews in Physical Chemistry* **2001,** *20* (3), 357-386.

177. Javadi, A.; Mucic, N.; Vollhardt, D.; Fainerman, V. B.; Miller, R. Effects of dodecanol on the adsorption kinetics of SDS at the water–hexane interface. *Journal of Colloid and Interface Science* **2010,** *351* (2), 537-541.

178. Hirose, C.; Akamatsu, N.; Domen, K. Formulas for the Analysis of the Surface SFG Spectrum and Transformation Coefficients of Cartesian SFG Tensor Components. *Appl. Spectrosc.* **1992,** *46* (6), 1051-1072.

179. Ciszewski, R. K.; Gordon, B. P.; Muller, B. N.; Richmond, G. L. Takes Two to Tango: Choreography of the Coadsorption of CTAB and Hexanol at the Oil–Water Interface. *The Journal of Physical Chemistry B* **2019,** *123* (40), 8519-8531.

180. Ruckenstein, E. Microemulsions, macroemulsions, and the Bancroft rul. *Langmuir* **1996,** *12* (26), 6351-6353.

181. Chevalier, Y.; Zemb, T. The structure of micelles and microemulsion. *Reports of Progress in Physics* **1990,** *53* (3), 279-371.

182. Li, Z. X.; Weller, A.; Thomas, R. K.; Rennie, A. R.; Webster, J. R. P.; Penfold, J.; Heenan, R. K.; Cubitt, R. Adsorption of the Lamellar Phase of Aerosol-OT at the Solid/Liquid and Air/Liquid Interfaces. *The Journal of Physical Chemistry B* **1999,** *103* (49), 10800-10806.

183. Li, Z. X.; Lu, J. R.; Thomas, R. K.; Penfold, J. Neutron reflectivity studies of the adsorption of aerosol-OT at the air-water interface: the structure of the sodium salt. *The Journal of Physical Chemistry* **1997,** *101* (9), 1615-1620.

184. Bell, G. R.; Bain, C. D.; Ward, R. N. Sum-frequency vibrational spectroscopy of soluble surfactants at the air/water interface. *J. Chem. Soc., Faraday Trans.* **1996,** *92*, 515-523.

185. Zdrali, E.; Etienne, G.; Smolentsev, N.; Amstad, E.; Roke, S. The interfacial structure of nano- and micron-sized oil and water droplets stabilized with SDS and Span80. *The Journal of Chemical Physics* **2019,** *150* (20), 204704.

186. Smit, W. J.; Smolentsev, N.; Versluis, J.; Roke, S.; Bakker, H. J. Freezing effects of oil-in-water emulsions studied by sum-frequency scattering spectroscopy. *The Journal of Chemical Physics* **2016,** *145*, 044706.

187. Stahla, M. L.; Baruah, B.; James D. M.; Johnson, M. D.; Levinger, N. E.; Crans, D. C. 1H NMR Studies of Aerosol-OT Reverse Micelles with Alkali and Magnesium Counterions: Preparation and Analysis of MAOTs. *Langmuir* **2008,** *24*, 6027-6035.

188. Eastoe, J.; Towey, T. F.; Robinson, B. H.; Williams, J.; Heenan, R. K. Structures of metal bis(2-ethylhexylsulfosuccinate) aggregates in cyclohexane. *The Journal of Physical Chemistry* **1993,** *97* (7), 1459-1463.

189. Eastoe, J. R., B. H.; Fragneto, G.; Towey, T. F.; Heenan, R. K.; Leng, F. J. Variation of Surfactant Counterion and Effect on the Structure and Properties of Aerosol-OT Based Water-in-Oil Microemulsions. *J. Chem. Soc. Faraday Trans.* **1992,** *3*, 461-473.

190. Aidarova, S.; Sharipova, A.; Krägel, J.; Miller, R. Polyelectrolyte/surfactant mixtures in the bulk and at water/oil interfaces. *Advances in Colloid and Interface Science* **2014,** *205*, 87-93.

191. Wang, C.; Cao, X.-L.; Guo, L.-L.; Xu, Z.-C.; Zhang, L.; Gong, Q.-T.; Zhang, L.; Zhao, S. Effect of molecular structure of catanionic surfactant mixtures on their interfacial properties. *Colloids and Surfaces A: Physicochemical and Engineering Aspects* **2016,** *509*, 601-612.

192. Morrison, I. D.; Ross, S. *Colloidal Dispersions: Suspensions, Emulsions, and Foams*. John Wiley and Sons, Inc.: New York, 2002; p 616.

193. Tajima, K. Radiotracer Studies on Adsorption of Surface Active Substance at Aqueous Surface. II. The effect of Excess Salt on the Adsorption of Sodium Dodecylsulfate. *Bull. Chem. Soc. Jpn.* **1970,** *43*, 3063-3066.

194. Tajima, K. Radiotracer Studies on Adsorption of Surface Active Substance at Aqueous Surface. III. The effects of Salt on the Adsorption of Sodium Dodecylsulfate. *Bull. Chem. Soc. Jpn.* **1971,** *44*, 1767-1771.

195. Datwani, S. S.; Stebe, K. J. Surface Tension of an Anionic Surfactant: Equilibrium, Dynamics, and Analysis for Aerosol-OT. *Langmuir* **2001,** *17* (14), 4287-4296.

196. Umlong, I. M.; Ismail, K. Micellization of AOT in aqueous sodium chloride, sodium acetate, sodium propionate, and sodium butyrate media: A case of two different concentration regions of counterion binding. *Journal of Colloid and Interface Science* **2005,** *291* (2), 529-536.

197. Ghosh, P.; Banik, M. Effects of Salts Containing Mono-, Di-, and Trivalent Ions on Electrical and Rheological Properties of Oil-Water Interface in Presence of Cationic Surfactant: Importance in the Stability of Oil-in-Water Emulsions. *Journal of Dispersion Science and Technology* **2014,** *35* (4), 471-481.

198. Aveyard, R.; Binks, B. P.; Lawless, T. A.; Mead, J. Interfacial tension minima in oil + water + surfactant systems. Effects of salt and temperature in systems containing non-ionic surfactants. *Journal of the Chemical Society, Faraday Transactions 1: Physical Chemistry in Condensed Phases* **1985,** *81* (9), 2155-2168.

199. Penfold, J.; Staples, E.; Tucker, I.; Thompson, L.; Thomas, R. K. Adsorption of Nonionic Mixtures at the Air–Water Interface: Effects of Temperature and Electrolyte. *Journal of Colloid and Interface Science* **2002,** *247* (2), 404-411.

200. Gurkov, T. D.; Dimitrova, D. T.; Marinova, K. G.; Bilke-Crause, C.; Gerber, C.; Ivanov, I. B. Ionic surfactants on fluid interfaces: determination of the adsorption; role of the salt and the type of the hydrophobic phase. *Colloids and Surfaces A: Physicochemical and Engineering Aspects* **2005,** *261* (1), 29-38.

201. Kumar, M. K.; Mitra, T.; Ghosh, P. Adsorption of Ionic Surfactants at Liquid−Liquid Interfaces in the Presence of Salt: Application in Binary Coalescence of Drops. *Industrial & Engineering Chemistry Research* **2006,** *45* (21), 7135-7143.

202. Langmuir, I. The Adsorption of Gases on Plane Surfaces of Glass, Mica, and Platinum. *Journal of the American Chemical Society* **1918,** *40* (9), 1361-1403.

203. Wu, W.; Fang, H.; Yang, F.; Chen, S.; Zhu, X.; Yuan, Q.; Gan, W. Understanding the Different Steps of Surfactant Adsorption at the Oil–Water Interface with Second Harmonic Generation. *Journal of Physical Chemistry C* **2016,** *120* (12), 6515-6523.

204. Weißenborn, E.; Braunschweig, B. Specific Ion Effects of Dodecyl Sulfate Surfactants with Alkali Ions at the Air-Water Interface. *Molecules* **2019,** *24*.

205. Eisenthal, K. B. Second Harmonic Spectroscopy of Aqueous Nano- and Microparticle Interfaces. *Chemical reviews* **2006,** *106* (4), 1462-1477.

206. Wang, H.; Yan, E. C. Y.; Liu, Y.; Eisenthal, K. B. Energetics and Population of Molecules at Microscopic Liquid and Solid Surfaces. *The Journal of Physical Chemistry B* **1998,** *102* (23), 4446-4450.

207. Johansson, P. K.; Koelsch, P. Vibrational Sum-Frequency Scattering for Detailed Studies of Collagen Fibers in Aqueous Environments. *Journal of the American Chemical Society* **2014,** *136* (39), 13598-13601.

208. Makarem, M.; Lee, C. M.; Sawada, D.; O'Neill, H. M.; Kim, S. H. Distinguishing Surface versus Bulk Hydroxyl Groups of Cellulose Nanocrystals Using Vibrational Sum Frequency Generation Spectroscopy. *The Journal of Physical Chemistry Letters* **2018,** *9* (1), 70-75.

209. Smolentsev, N.; Chen, Y.; Jena, K. C.; Brown, M. A.; Roke, S. Sum frequency and second harmonic generation from the surface of a liquid microjet. *The Journal of Chemical Physics* **2014,** *141* (18), 18C524.

210. Wang, H.-F.; Yan, E. C. Y.; Borguet, E.; Eisenthal, K. B. Second harmonic generation from the surface of centrosymmetric particles in bulk solution. *Chemical Physics Letters* **1996,** *259* (1), 15-20.

211. de Beer, A. G. F.; Samson, J.-S.; Hua, W.; Huang, Z.; Chen, X.; Allen, H. C.; Roke, S. Direct comparison of phase-sensitive vibrational sum frequency generation with maximum entropy method: Case study of water. *The Journal of Chemical Physics* **2011,** *135* (22), 224701.

212. Marx, C. A.; Harbola, U.; Mukamel, S. Nonlinear optical spectroscopy of single, few, and many molecules: Nonequilibrium Green's function QED approach. *Physical Review A* **2008,** *77* (2), 022110.

213. Goodman, A. J.; Tisdale, W. A. Enhancement of Second-Order Nonlinear-Optical Signals by Optical Stimulation. *Physical Review Letters* **2015,** *114* (18), 183902.

214. Wen, Y.-C.; Zha, S.; Liu, X.; Yang, S.; Guo, P.; Shi, G.; Fang, H.; Shen, Y. R.; Tian, C. Unveiling Microscopic Structures of Charged Water Interfaces by Surface-Specific Vibrational Spectroscopy. *Physical Review Letters* **2016,** *116* (1), 016101.

215. Ohno, P. E.; Saslow, S. A.; Wang, H.F.; Geiger, F. M.; Eisenthal, K. B. Phase-referenced nonlinear spectroscopy of the α-quartz/water interface. *Nature Communications* **2016,** *7* (1), 13587.

216. Ong, S.; Zhao, X.; Eisenthal, K. B. Polarization of water molecules at a charged interface: second harmonic studies of the silica/water interface. *Chemical Physics Letters* **1992,** *191* (3), 327-335.

217. Geiger, F. M. Second Harmonic Generation, Sum Frequency Generation, and χ(3): Dissecting Environmental Interfaces with a Nonlinear Optical Swiss Army Knife. *Annual Review of Physical Chemistry* **2009,** *60* (1), 61-83.

218. Ohno, P. E. On Phase and the $\chi^{(3)}$ Effect in Second-Order Nonlinear Spectroscopy. Northwestern University, Evanston, Illinois, 2019.